A Multiscale *In Silico* Investigation of the Mechanics and Dynamics of *Ex Vivo* Coagulation

by

Megan Patricia Cala

Bachelor of Science in Biology, Seton Hill University, 2014

Submitted to the Graduate Faculty of

the Swanson School of Engineering in partial fulfillment

of the requirements for the degree of

Doctor of Philosophy

University of Pittsburgh

2020

UNIVERSITY OF PITTSBURGH

SWANSON SCHOOL OF ENGINEERING

This dissertation was presented

by

Megan Patricia Cala

It was defended on

July 14, 2020

and approved by

Robert S. Parker, Ph.D., Professor, Department of Chemical and Petroleum Engineering,

Department of Bioengineering

Joseph J. McCarthy, Ph.D., Professor, Department of Chemical and Petroleum Engineering

Ipsita Banerjee, Ph.D., Associate Professor, Department of Chemical and Petroleum

Engineering, Department of Bioengineering

Jeffrey Vipperman, Ph.D., Professor, Department of Mechanical Engineering and Materials

Science, Department of Bioengineering

Dissertation Advisors: Robert S. Parker, Ph.D., Professor, Department of Chemical and

Petroleum Engineering, Department of Bioengineering,

Joseph J. McCarthy, Ph.D., Professor, Department of Chemical and Petroleum Engineering

A Multiscale *In Silico* Investigation of the Mechanics and Dynamics of *Ex Vivo* Coagulation

Megan Patricia Cala, PhD

University of Pittsburgh, 2020

Theories describing the coagulation cascade have been around for decades and have greatly expanded in functional detail over the past several years. However, there still exists a void in the literature on the quantification of the microscale contribution of individual blood cell mechanics on the macroscale behavior of blood clots. This is due, in part, to the fact that the trans-scale relationships between blood components are not fully understood. In this work, we aim to bridge the gap between the known cell-scale phenomena of coagulation, specifically platelet and fibrin interactions, and the measurable mechanics and dynamics of whole blood clots.

The developed multiscale model consists of two main components: (1) a phenomenological model of activated platelet adhesion and contraction and (2) a mechanistic model of fibrin viscoelasticity and strain-hardening extensibility. The components of the multiscale model include stand-alone discrete element method (DEM)-based cell-scale models for the primary components of blood. The unique mechanical and dynamical behaviors observed experimentally in single-platelet and single-fiber studies can be captured by this technique due to the inclusion of phenomenological force models, namely piecewise linear functions for the adhesion exhibited by activated platelets and Hill functions for the nonlinear elastic modulus of fibrin.

The isolated platelet adhesion and fibrin extension models were developed and calibrated separately before they were combined to study the emergent behavior of platelet and fibrin assemblies. The platelet and fibrin compositions were varied between simulations to assess the morphological and mechanistic differences of *in silico*-formed aggregates. Applying the model within a dynamic framework was also used to obtain a macroscale metric of *in silico* aggregate behavior that is comparable to one from existing clinical whole-blood diagnostic devices like the thromboelastogram, or TEG. Specifically, we can quantify the platelet con-

tribution to the strength of platelet and fibrin *in silico* aggregates. We observed a nonlinear relationship between platelet concentration and platelet contribution that corroborates experimental studies. The culmination of the modeling efforts from this dissertation is a tool that can be used and expanded to better understand the mechanistic detail of platelet and fibrin contributions during coagulation.

Table of Contents

List of Tables

List of Figures

Preface

This dissertation is dedicated to the village that has supported me throughout my doctoral journey. In addition to those mentioned in this preface, I am also grateful for the passionate teachers that have inspired me throughout my education and whose active guidance started me on this track many years ago. Two that cannot go unnamed are Mrs. Carolyn Stewart, my high school computer science and mathematics teacher who was a real pioneer in the field and is a radiant role model for women in STEM, and Dr. Jamie Fornsaglio, my enthusiastic undergraduate advisor who was instrumental in my successful pivot to engineering and research.

I am very grateful to my co-advisors, Drs. Robert Parker and Joseph McCarthy, for their invaluable mentorship over the past five and a half years. They helped me to develop my critical thinking research lens and quantitative mindset as I transitioned into and made the field of chemical engineering my home. Most of all, I am thankful for their intellectual creativity in fostering this project that has emerged at the interface of their seemingly dissimilar areas of expertise. I am also grateful to have learned a thing or two about home-brewing from them when the topic meandered into our weekly meeting agendas.

Thank you to my other two committee members, Drs. Ipsita Banerjee and Jeffrey Vipperman, for the diverse perspectives that they brought to my dissertation and for their patience in scheduling my thesis defense during a pandemic.

I am forever indebted to my wonderful family who I would like to thank for their unwavering support and constant encouragement during my graduate school years and in life. To my late grandparents, Baba & Nonno and Nana & Pap, for teaching me the value of education, showing me how to live life to the fullest, and building a family, deeply rooted in faith. To my parents, Kate and Greg Cala, for their unconditional love and instilling in me their shared passion for life-long learning and humor. Their many selfless sacrifices created opportunities for me that I recognize have shaped me into the person I am today. To my late Uncle Mike for paving the way by earning his PhD in chemical engineering from Purdue University in 1984 and planting the chemical engineering seed in my mind many years ago.

To my brother, Andrew, and his wife, Katie, for helping me to maintain a positive outlook on life and to their adorable children that fill my heart (and my laptop backgrounds). To my brother, Kevin, and his fiancé, Lauren, for always having great advice and helping me to keep the ebbs and flows of life in perspective. And to Joe Pane for inspiring me to be the best person I can be and for being an incredible teammate as we navigate the perfect balance between running and ice cream, I mean work and life.

Last, but not least, I would like to acknowledge my former and current colleagues for their contributions to the welcoming culture of our department that has made all of the difference during my time at the University of Pittsburgh. To the Parker (Ari, Matt, Tim, Christy, Li Ang, Flo, Michelle, Monica, Brian, and Stefanos) and McCarthy (Chris, Melissa, Diana, Sue, Siying, Ramon, and Shichao) Lab folks, Jenna Gustafson, Gianfranco and Fabiana Rodriguez, Michael Taylor, Ashlee Greene, Emily Ackerman, and Andrea Schilling - I have been lucky to call you not only my colleagues, but my genuine friends.

1.0 Introduction

Blood clotting, or coagulation, is an essential physiological mechanism that contributes to homeostasis by stemming blood loss after vascular injury [1]. The complex, multi-step mechanism of coagulation has been classically termed the "coagulation cascade," and is comprised of a sequence of several reactions involving blood cells, blood-cell fragments, proteins, and other biological factors [41, 83]. Blood is comprised of red blood cells, white blood cells, and platelets suspended in a protein-rich fluid called plasma [30]. Red blood cells, present in the highest solids volume fraction, dominate blood rheology, but the concentrations and interplay of other primary constituents, namely white blood cell fragments (platelets) and proteinaceous meshes (fibrin), dictate the mechanics and dynamics of coagulation [78, 114]. At the onset of coagulation, platelets spontaneously activate and acquire adhesive properties that facilitate platelet aggregation and the formation of a plug. The platelet plug becomes the center of the clot, which is also stabilized by a fibrin mesh that polymerizes throughout the clot.

The regulation of the coagulation cascade requires the harmonious interplay of several key players and processes, including blood cell aggregation and adhesion, and the flow and transport of important cells and clotting factors. It relies on the successful biochemical communication of the entire network to maintain the spatiotemporal organization necessary to resolve any imbalances within the system. Any minor disruption to any of these processes or players can amplify to serious pathologies like hemorrhage or excess clotting.

Within the last century, remarkable progress has been made toward improving our understanding of coagulation and resolving the mechanical properties of blood clots [80, 33, 123]. The extent of hemostasis, the process by which bleeding is stopped, falls on a spectrum with pathologies manifesting at both ends. Normal hemostasis consists of both the formation of a clot and its subsequent breakdown after healing [107]. A perturbation to hemostasis can lead to bleeding (hemorrhage) or to obstructive clotting (thrombosis). Hemorrhage results from the delayed onset or altogether absence of clotting and/or the rapid occurrence of clot lysis, whereas thrombosis results from excess blood clotting and/or the failure of clot lysis

[94]. The mechanical properties of blood can be related to hemostatic disorders and are therefore commonly used in hematological disease diagnosis [95].

1.1   Mechanics and Dynamics of Hemostasis

Under physiological flow conditions, red blood cells have the most significant effect on the mechanical properties of blood [108]. Round, biconcave, and extremely deformable, red blood cells are able to squeeze through openings smaller than their 6-8 μm diameter. The ability of the red blood cells to orient with the flow of blood leads to the non-Newtonian, shear thinning nature of blood [54]. Specifically, under low shear conditions, blood is highly viscous, and with increased shear, the viscosity of blood decreases nonlinearly as the red blood cells deform and orient with the flow [93]. Platelets have a discoid shape that measures 2-3 μm in diameter and 0.5 μm in height when circulating in their quiescent state [76]. They are produced from fragmented bone marrow megakaryocytes and have important roles in immune defense, cancer metastasis, and most relevantly, wound healing [113]. Due to their smaller size and lower concentration than red blood cells, the effect of platelets on the mechanical properties of blood under physiological flow conditions is negligible [30]. However, this reality reverses nearly spontaneously at the onset of hemostasis.

The coagulation cascade begins when platelets are exposed to sub-endothelial collagen or to high shear forces in the presence of clotting factors, which induces platelet activation. Activated platelets secrete granules that modify their membrane surface characteristics, inducing particularly adhesive properties and a more spherical structure [91]. Following platelet activation, a platelet aggregate forms and becomes the center of the clot [24, 42, 43]. Upon activation, platelet integrins, such as $\alpha_{IIb}\beta_3$, switch from low to high affinity states to facilitate platelet-fibrinogen interactions [27]. Fibrinogen is a fibrous macromolecule that bridges platelets via $\alpha_{IIb}\beta_3$, allowing the formation of platelet aggregates [49].

At the same time, the activated platelets allow the conversion of endogenous prothrombin into active thrombin, the enzyme necessary to induce the polymerization of fibrinogen into fibrin bundles [106]. Thrombin also activates other nearby platelets. Fibrin monomers link

together to form fibrin sub-units called protofibrils [32]. Protofibrils aggregate laterally and wrap into fibrin fibers, which branch to make a three dimensional network [123]. Fibrin serves to strengthen the clot by forming an extensible meshwork that is held together by the adhesive platelets, where the degree of platelet activation dictates the strength of adhesion and therefore ultimately the strength of the clot [98].

During clot formation, a process known as clot contraction occurs, in which the viscous fluid plasma is displaced and much is expelled from the clot [81]. The volume of fluid plasma expelled from a clot can be collected and measured as a surrogate for the extent of clot contraction [109]. Although the function of red blood cells in clot contraction is not well understood, their deformability is particularly noted because as clots contract, red blood cells can deform through vessel structures smaller than their diameter [51, 60, 75]. Contracting clots can also undergo subtle platelet and fibrin rearrangements. A shift in platelets and fibrin to the exterior of the clot reduces the clot permeability and enhances would healing [16].

The myriad of other cells and tissue components in the blood are capable of interacting with a growing clot or thrombus and can contribute to its formation, but pale in comparison to the role of platelets and fibrin [124]. Though the key coagulation contributors are known, their particular mechanical influence is still only vaguely understood. The mechanical properties of clots and thrombi are critical to their physiological function and a determinant of the response to treatment of both hemorrhagic and thrombotic conditions [123].

1.2   Measurements of Blood Mechanical Properties

1.2.1   Isolated cell-scale assessments

From a sample of whole blood, individual cell counts can be measured, such as platelet count, red blood cell concentration (hematocrit), fibrinogen level, clotting times, and various clotting factor levels, though these mere quantities do not reveal any insight into their contribution to the mechanical properties of blood [37].

With the invention of the atomic force microscope (AFM) in 1986, the study of how underlying molecular mechanisms connect with macroscopic mechanical behaviors within biological systems has gained momentum [123, 89]. Quantitative experimental measurements of the physical properties of particles on the cell-scale can be performed with high resolution. This technique has been applied to both platelets and fibrin, leading to greater insight into their unique adhesive and extensible properties, respectively [25, 86].

By measuring the force required to rupture the bond between a platelet-platelet and platelet-fibrin bond at varying degrees of platelet activation, the dynamics of platelets throughout the stages of the coagulation cascade are better understood. Through two seminal studies by Nguyen et al. and Lam et al., it was discovered that the adhesive power of platelets increases with an increase in the degree of platelet activation [77, 56]. AFM has been coupled with force spectroscopy to measure the extensibility of a single fibrin bundle. Through a recent experimental study, it was reported that fibrin exhibits viscoelastic and strain hardening properties, exhibited by nonlinear force versus strain profiles [63]. A single strand of fibrin can be stretched up to 3.3 times its original length before rupturing.

1.2.2 *Ex vivo* whole-blood assays

In the clinic, the coagulation status of patients can be assessed using devices such as the TEG, ROTEM, and hemodyne [78, 123]. These point-of-care devices have subtle differences, but all evaluate the whole blood clotting process from platelet aggregation to fibrinolysis.

A TEG is the readout of a point-of-care device used in the clinic to obtain functional coagulation state assessments with the simple addition of a sample of whole blood [96]. As shown in Figure 1A, the device contains an initially stationary pin that is suspended in an oscillating cup containing the blood sample. Changes in torque between the pin and the cup resulting from clot formation are traced through a computer-processed signal of the pin rotations. Parameter values from the TEG tracings are compared to reference ranges to guide the treatment of potential coagulopathies [82]. A schematic of a sample TEG with the labeled parameter values is shown in Figure 1B.
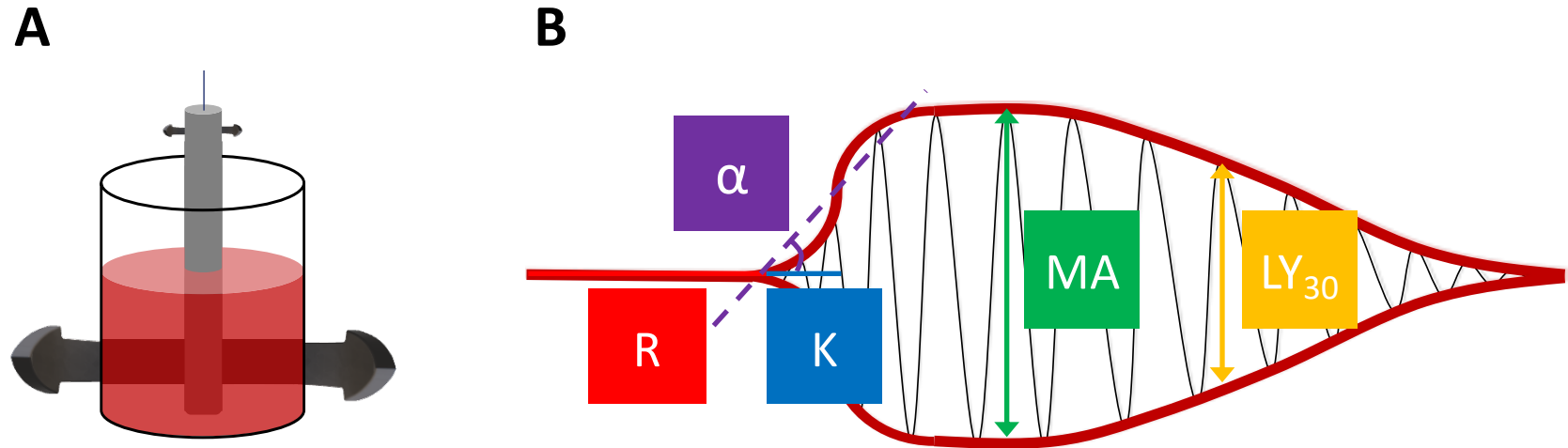
Figure 1: Schematic of (A) a TEG cup containing a whole-blood sample and suspended pin hanging from a torsion wire and (B) a normal TEG tracing (not to scale) resulting from an outline of the pin oscillations during coagulation with the five labeled key parameters used to assess the coagulation state of its subject.

The five key parameters characterizing a TEG tracing are the time to initiation of coagulation (R), the rate of formation of the clot (α-angle), the maximal amplitude (MA) of the oscillation, the time required for the oscillation to reach the maximal amplitude from the start of clot formation (K), and percentage decrease in amplitude at thirty minutes post-MA (*LY30*). Traditionally, R depends on soluble clotting factors, K on surface active factors, α on fibrinogen and platelets, MA on platelet count and functional clot strength, and *LY30* on the degree of fibrinolysis [78, 9].

The dynamic parameters obtained from these tests are compared to standard ranges obtained from a healthy control reference so that appropriate treatments or treatment corrections can be designed and administered. Because MA represents contributions of various blood components to the clot, including platelets and fibrin/fibrinogen, it is not the most sensitive indicator of a platelet deficiency. Alternatively, the platelet component of clot strength can be derived from the comparison of TEG tests performed with and without platelet inhibition [98]. While the simple and straight-forward nature of the TEG is appealing to clinicians, the suggested treatments for coagulopathies are rarely precise, which often leads to patients receiving a transfusional cocktail of blood-product therapies [9].

The dynamic capacity of the measurements made by these devices provides a distinct advantage over static quantitative clinical tests [96, 82]. However, the meaningfulness of the parameters measured by these devices is limited to the realm of the respective device because the exact connection between the microscale *in vivo* mechanistic contributions of whole blood constituents to the macro-observable parameters from these devices is not fully understood.

1.3   Existing *In Silico* Models of Coagulation

Despite the vast advancements surrounding hemostasis and thrombosis over the past three decades, bleeding complications are still the major immediate cause of morbidity and mortality in the world [6]. To enhance the study of the complexities surrounding coagulation, mathematical and computational modeling has been increasingly used in parallel with

experimental studies [97]. Though simplifying assumptions and approximations are part of every model, an improved understanding of coagulation physiology and more powerful computing have led to the development of more accurate models in recent years.

Within the computational biomechanical framework, simulation objectives for hematological models typically guide the selection from continuum- and/or discrete-based methods [115, 33, 2]. Continuum methods usually involve systems of coupled differential equations whose solutions and applicability may be limited to a narrow scope of simulation conditions and often represent oversimplified systems [30]. Alternatively, to bypass some of the limitations and abstractions of continuum methods, more intuitive discrete methods can be employed at the cost of increasing computational complexity [23, 117]. These methods explicitly define each particle as a specific type with distinct properties and laws that govern the possible constituent interactions, enabling the fine control of heterogeneous systems. The mechanical forces acting upon each particle are remembered and particle positions are reassigned at each time step [34]. Until the verge of instability is reached, decreasing the time step of discrete models increases the model accuracy, but further increases the computational cost.

There are several variations of discrete approaches, including adhesive dynamics (AD), discrete element method (DEM), molecular dynamics (MD), smoothed particle hydrodynamics (SPH), and dissipative particle dynamics (DPD) [122, 67, 38, 50, 26]. All of these methods are grounded in the solution to Newtonian physics across a collection of particles.

Further coarse graining discretized systems can increase the utility in capturing emergent behavior of complex collections of a large number of cells [33, 23, 117]. Several existing hematological models have successfully captured the *in vivo* dual behavior of platelet margination combined with the deformation of red blood cells in high shear scenarios [4, 85, 84]. The work of Wang et al. has shown promise for capturing the interplay between a small number of cells within a network or matrix, while accurately capturing the impact of fluid mechanical forces from surrounding blood plasma [122]. The correlation between the dynamics of adhesion and bond characteristics, such as association and elasticity, was an insightful advancement made by Chang et al. in their model of platelets and white blood cells [12].

A fluid dynamics technique known as Lattice Boltzmann Method (LBM) has been com-
bined with discrete particle-based methods to increase the accuracy of the solid-fluid inter-
action beyond that possible of continuum methods or discrete particle-based methods alone
[19, 64]. The fluid in a LBM framework is described with a distribution function defined as
the probability density of locating a given number of molecules with a certain velocity at
a certain place and time in the three-dimensional simulation frame [14]. The distribution
functions can propagate along neighboring nodes of the discretized simulation in a collision
and streaming fashion [11, 35].

Several groups have applied LBM to model the response of the vascular occlusion in
intracranial aneurysms to changes under various flow conditions [36, 40, 79, 132]. *In sil-
ico* models of *ex vivo* coagulation in three-dimensional space is an under-developed area of
computational hematological research, therefore motivating the work herein [8]. The multi-
scale and multiphase nature of blood motivates the use of a combinational model of a fluid
dynamics technique along with a discretized particle-based method [128, 129].

1.4   Relevant Computational Methods

A combinational method can capture the two-way phenomena of how the fluid dynamics
are influenced by the presence of particles, and how the displacement of the particles is
driven by the fluid-induced forces [28]. In our framework, solid-fluid coupling is computed
at each time step by first obtaining the fluid solution with LBM, and then updating the
particle positions using DEM. From the resulting increase in resolution of the fluid flow and
increase in accuracy of the force calculations at the solid-fluid boundary, a unique insight
into the interplay between biophysics and the details of blood is expected [22, 59].

1.4.1   Discrete Element Method (DEM)

In DEM, the bulk evolution of particle assemblies is calculated through the integration
of the forces of interacting particle pairs [21, 130]. The solution to Newton's equations of

motion are used to calculate the particle trajectories. Equations 1.1 and 1.2 describe the linear and angular particle motion, respectively,

$$m_p \frac{d\vec{v}_p}{dt} = -m_p \vec{g} + \vec{F}_n + \vec{F}_t \tag{1.1}$$

$$I_p \frac{d\vec{\omega}_p}{dt} = \vec{R} \times \vec{F}_t \tag{1.2}$$

where m_p, $\vec{v}_p$, $\vec{g}$, I_p, and $\vec{\omega}_p$ are the mass, translational velocity, gravity vector, moment of inertia, and rotational velocity of particle p. $\vec{F}_n$ and $\vec{F}_t$ are the normal and the tangential forces, respectively, and $\vec{R}$ is the vector between the center of particle p and the contact point where $\vec{F}_t$ is applied.

Several force-displacement models have been developed based on theoretical contact mechanics [20]. The accuracy of calculations depends on the contact models selected. The work herein follows the theory developed by Hertz [47]. The normal component of a collision between two particles is chosen according to the elastic properties of the solids. Considering pairwise interactions among particles, the normal force, assumed to be elastic during the initial stages of loading, is described by Equation 1.3,

$$F_n^e = k_n^e \alpha^{3/2} \tag{1.3}$$

where α is the amount of particle-particle overlap or particle deformation and can be calculated from Equation 1.4,

$$\alpha_i = (R_i + R_j) - \delta_{ij} \tag{1.4}$$

where R_i and R_j are the undeformed radii of particles i and j, respectively, and δ_{ij} is the distance between the two geometric centers of each particle. The elastic normal contact stiffness, k_n^e, can be related to the particles' mechanical properties, including their Young's moduli (E) and Poisson's ratios (v), according to Equation 1.5,

$$k_n^e = \frac{4}{3} E^* \sqrt{R^*} \tag{1.5}$$

where E^* and R^* are

$$\frac{1}{E^*} = \frac{1 - v_i^2}{E_i} + \frac{1 - v_j^2}{E_j} \tag{1.6}$$

$$\frac{1}{R^*} = \frac{1}{R_i} + \frac{1}{R_j} \tag{1.7}$$

respectively [47].

The tangential force model used for the work herein was derived by Walton and Braun [119]. For each time-step, the new tangential force, F_t, acting at the interparticle contact point is defined as Equation 1.8

$$F_t = F_{t,old} - k_t \Delta s \tag{1.8}$$

where $F_{t,old}$ is the tangential force from the previous time-step and $k_t \Delta s$ is the incremental change in the tangential force during the present time-step due to relative particle motion [118]. In other words, Δs is the relative surface displacement between the contacting particles during the current time-step and can be calculated from the component of the velocity that is tangent to the contact surface, v_t (i.e. $\Delta s = v_t dt$, where dt is the time-step). The frictional stiffness, k_t, is defined as Equation 1.9

$$k_t = 8G^* a \tag{1.9}$$

where G^* is the effective shear modulus defined as Equation 1.10 and a is the contact radius.

$$\frac{1}{G^*} = \frac{2 - v_i}{G_i} + \frac{2 - v_j}{G_j} \tag{1.10}$$

1.4.2   Lattice Boltzmann Method (LBM)

LBM is a class of computational fluid dynamics methods used to simulate fluid flows without directly solving the equations of continuum fluid mechanics [3, 65, 101]. It is based on the microscopic particle models and mesoscopic kinetic equations and assumes that macroscopic behavior of a fluid system is not very sensitive to the underlying microscopic particle behavior if only collective macroscopic flow behavior is of interest [99]. The fundamental idea of LBM is to incorporate the essential physics of the micrscopic process in a mescopic

kinetic model so that the relationship among average properties at the macroscale conforms to the Navier-Stokes equations. In the theoretical studies and simulations of LBM, various lattice discretization schemes have been proposed in one, two, and three dimensions. The standard nomenclature used to classify the different schemes is $DiQj$, where i represents the number of dimensions (1D, 2D, or 3D) and j represents the number of discrete directions (3 for 1D, 6 or 9 for 2D, and 15, 19, or 27 for 3D) [3]. D3Q19, 3D with 19 discrete velocities, has been shown to provide a suitable combination of computational stability and accuracy, thus the chosen scheme for this work. A schematic of the D3Q19 lattice velocities is shown in Figure 2.

The governing equation for the evolution of the LBM fluid distribution functions is defined as Equation 1.11

$$f_i(x + e_i\delta t, t + \delta t) - f_i(x,t) = f_i(x,t) + \Omega_i(x,t) \tag{1.11}$$

where $\Omega_i(x,t)$ is the collision operator. The most widely implemented LBM model, which utilizes the Bhatnagar-Gross-Krook (BGK) approximation for the collision operator, was chosen for the work herein [5, 87]. The evolution of the fluid can be calculated from a modified Equation 1.11, included as Equation 1.12, which contains two sub-steps that are executed during each computational iteration: streaming and collision.

$$f_i(x + e_i\delta t, t + \delta t) - f_i(x,t) = -\frac{1}{\tau}[f_i(x,t) - f_i^{eq}(x,t)] \tag{1.12}$$

In the governing equation, f_i, x, t, e_i, and δt are the probability distribution function (PDF) of a node in direction i, position, time, microscopic velocity, and time step, respectively [7]. The left-hand-side of Equation 1.12 represents the streaming step, in which fluid particles are propagated across the lattice. The right-hand-side of Equation 1.12 is the collision operator, where τ is the dimensionless relaxation time that controls the rate that f_i approaches f_i^{eq}, the equilibrium probability distribution function (EDF). The EDF can be related to the fluid density (ρ), the fluid velocity vector ($\vec{u}$), a weighting factor (w_i), and the lattice speed (c) according to Equation 1.13.

$$f_i^{eq}(x,t) = w_i\rho \left[1 + 3\frac{\vec{e}\cdot\vec{u}}{c^2} + \frac{9}{2}\frac{(\vec{e}\cdot\vec{u})^2}{c^4} - \frac{3}{2}\frac{\vec{u}\cdot\vec{u}}{c^2}\right] \tag{1.13}$$

11
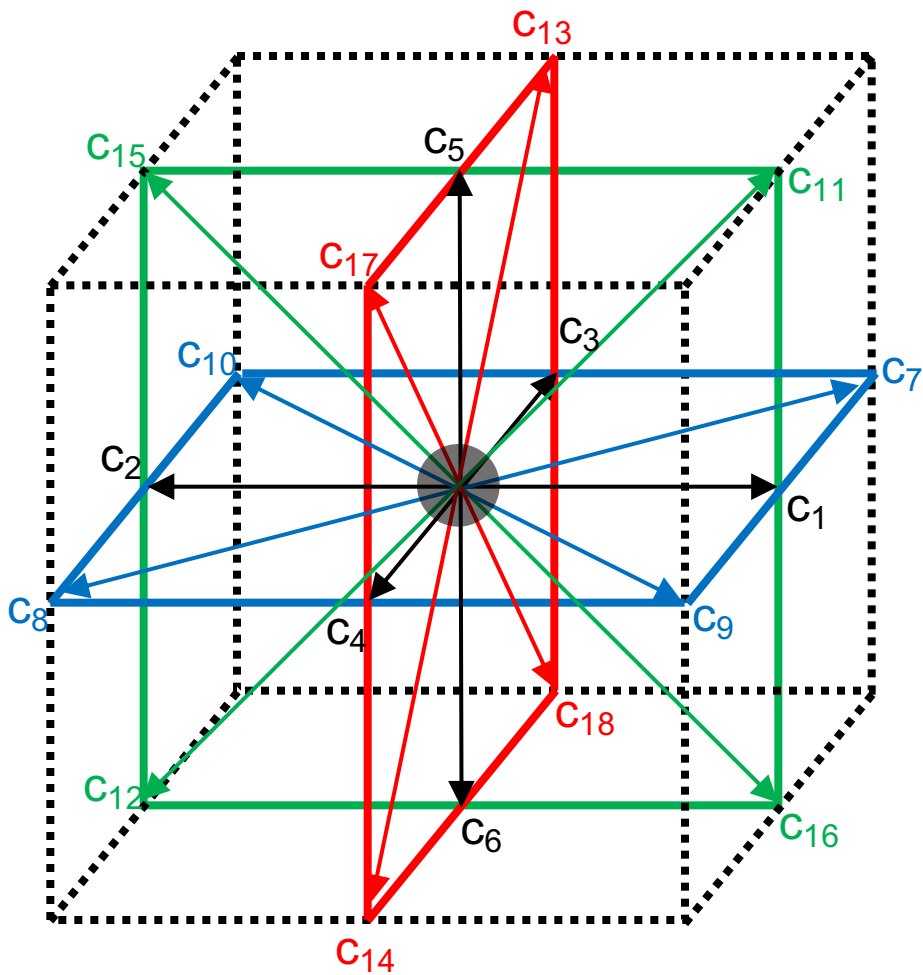
Figure 2: The 19 lattice velocities ($\vec{c}_i$) used in the D3Q19 discretization scheme of LBM.

When the D3Q19 lattice discretization scheme is used, 19 discrete particle velocities in directions $\vec{e}_i$ are introduced and defined according to Equation 1.14.

$$
\vec{e}_i = \begin{cases}
e_0 = c(0,0,0) \\
e_1 = c(0,1,0) \\
e_2 = c(0,-1,0) \\
e_3 = c(0,0,1) \\
e_4 = c(0,0,-1) \\
e_5 = c(1,0,0) \\
e_6 = c(-1,0,0) \\
e_7 = c(0,1,1) \\
e_8 = c(0,-1,-1) \\
e_9 = c(0,1,-1) \\
e_{10} = c(0,-1,1) \\
e_{11} = c(1,0,1) \\
e_{12} = c(-1,0,-1) \\
e_{13} = c(-1,0,1) \\
e_{14} = c(1,0,-1) \\
e_{15} = c(1,1,0) \\
e_{16} = c(-1,-1,0) \\
e_{17} = c(-1,1,0) \\
e_{18} = c(1,-1,0)
\end{cases} \tag{1.14}
$$

The density (ρ) and velocity vector ($\vec{u}$) are related to the PDF and EDF according to Equations 1.15 and 1.16.

$$
\rho = \sum_i f_i = \sum_i f_i^{eq} \tag{1.15}
$$

$$
\rho \vec{u} = \sum_i \vec{e}_i f_i = \sum_i \vec{e}_i f_i^{eq} \tag{1.16}
$$

13

The pressure (p) is calculated directly from the equation of state of an ideal gas according to Equation 1.17,

$$p = c_s^2 \rho \tag{1.17}$$

where c_s is the speed of sound, related to the lattice speed (c), given by $c_s = c/\sqrt{3}$.

In the GBK model, viscosity (ν) is defined as Equation 1.18.

$$\nu = c_s^2 (\tau - \frac{1}{2})\delta t \tag{1.18}$$

The bounce-back rule applies for nodes designated as solid to reflect the fluid in the opposite direction at the collision stage. If boundaries are set to be periodic in a particular direction, the last face of nodes is contiguous with the opposing face to ensure the lattice is closed in the periodic direction [3].

1.5 Dissertation Overview

This dissertation outlines the development, validation, and application of a multiscale discrete element method (DEM)-based *in silico* model of platelet and fibrin interactions during *ex vivo* blood coagulation. Chapter 2 focuses on the development of a model that captures the mechanics and dynamics of activated platelets, namely platelet-platelet, and platelet-fibrin interactions. Parallel to Chapter 2, the focus of Chapter 3 is the development of a mechanistic model that captures the viscoelastic and strain-hardening behavior of fibrin, the polymer that forms an integrated meshwork throughout a growing clot. Chapter 4 combines the platelet model from Chapter 2 and the fibrin model from Chapter 3 with a fluid dynamics technique called the Lattice Boltzmann Method (LBM) to evaluate the emergent behavior of pre-assembled clots with varied concentrations of activated platelets in the presence of both implicitly and explicity modeled fibrin bundles. Chapter 5 applies the multiscale model from Chapter 4 to a dynamic framework to measure the physical strength of the platelet-fibrin networks upon exposure to a linear stretching force. The resulting dynamic

multiscale model provides the underlying framework for a tool that can be used to understand the *in vitro* microscale contribution of fibrin and platelets on the macro-observables of whole blood point-of-care devices.

The focus of Chapter 2 is the development of a phenomenological model of activated platelet adhesion. Though far less numerous than red blood cells in the circulatory system, platelets play a critical role in coagulation [73, 92]. As the first responders to a bleeding or thrombotic event, platelets form small aggregate plugs that become the center of the clot [55]. Platelets are also active recruiters of downstream procoagulant activity, including the activation of nearby platelets and clotting factors [4]. We seek to capture the adhesive characteristics of platelets *in silico* by including two distinguishable forces that act between a platelet and its adherent substrate. The adhesive force resists platelet separation and the contractive force induces particle-particle overlap at the equilibrium position of a platelet and its neighbor. Three levels of platelet activation can be modeled, whereby the adhesive capacity increases with each level of activation. Chapter 2 functions as a cell-scale building block of the multiscale model established in Chapters 4 and 5. Model validation is performed with the availability of rupture force-strain information obtained from *in vitro* isolated platelet-platelet and platelet-fibrin interaction studies.

Chapter 3 covers the development of a mechanistic model of fibrin viscoelasticity and strain-hardening extensibility. Fibrin strands assemble during the early stages of the coagulation cascade to form the fibrinous networks that extend throughout clots and maintain clot integrity *in vivo* under high arterial pressure [10, 111, 112]. Several distinct mechanical properties of individual fibrin strands, including viscoelasticity and strain-hardening extensibility, facilitate the physiological functionality of these polymers [17, 100]. From *in vitro* extension-retraction studies of single fibrin bundles, the distinct mechanical properties can be quantified and used to validate our model. Specifically, the degree of strain-hardening is observed by a comparison of the increased slope at increased strain to the initial slope on the stress-strain curves [63]. The viscoelastic behavior is evident by the hysteresis, or the departure between the extension and retraction curves, where the area between the curves is proportional to the energy dissipated [57, 95]. *In silico*, we can model both of these mechanical properties of fibrin by mathematically defining the elastic modulus as a Hill function.

Since fibrin becomes more viscous with increased strain, the parameters of the Hill function that correspond to the retraction portion of the stress-strain curves are modified as the strain increases [68]. The Hill function parameters for the extension and retraction curves are all fit to experimental data. Similar to Chapter 2, Chapter 3 also functions as a cell-scale building block of the multiscale model proposed in Chapters 4 and 5.

In Chapter 4, a platelet and fibrin combination model is developed and validated with *in vitro* clot properties. By combining the two cell-scale models of platelets and fibrin, described in Chapters 2 and 3, respectively, with a fluid dynamics technique called Lattice Boltzmann Method (LBM), we take the first steps toward a multiscale model of coagulation. From simulations of the combined model, we demonstrate that variations in blood composition of key blood components leads to different qualitative and quantitative descriptors, similar to the observables in permeability and contractility *in vitro* experiments [126, 108]. A pathological fibrin scenario is simulated by incorporating fibrin as implicit entities to investigate the effect of compromised fibrin on aggregation. With our validated model, we define relationships between the concentrations of blood coagulation contributors and corresponding clot permeabilities and pore size distributions.

Chapter 5 extends the static model of *ex vivo* platelet and fibrin assemblies from Chapter 4 to a dynamic framework by applying a uni-axial stretch to the aggregates. By simulating *ex vivo* clot dynamics, we avoid multiple degrees of complexity associated with coagulation *in vivo* revolving around the modular flow conditions during bleeding and thrombotic events as well as the myriad of biophysical and biochemical signals and cues that stem from the exposure of the damaged sub-endothelial matrix [41, 24]. From the simulations of stretching aggregates, we generate an *in silico* aggregate metric, specifically the platelet contribution, that is comparable to one from existing clinical whole-blood diagnostic devices like the TEG. The culmination of the modeling efforts within this chapter is a tool that can be used and expanded to better understand the mechanistic detail of platelet and fibrin contributions during coagulation.

The key contributions of this dissertation include the following:

- a calibrated DEM-based model of platelet adhesion with the capacity to vary platelet activation

- progress toward traversing the gap to the macroscale with a platelet aggregate formation model

- development of methods to quantify the emergent aggregate morphologies, i.e. pore size distribution

- two approaches of fibrin inclusion, i.e. immobile lines and flexible strands of tethered particles

- application of LBM to quantify the platelet and fibrin aggregate permeabilities

- application of the platelet and fibrin aggregates to a dynamic framework to quantify their strength

- development of a method to quantify the platelet contribution to the aggregate strength

2.0 Phenomenological Model of Activated Platelet Adhesion

2.1 Background

The focus of Chapter 2 is the development of a stand-alone, DEM-based model of activated platelets that accurately captures the mechanics of platelet-platelet and platelet-fibrin interactions. Platelets are the first responders to an induction of hemostasis, such as vascular injury. In the bloodstream, platelets interact with hundreds of biochemical and biophysical signals, including fibrin networks [31]. Platelets can sense certain aspects of their mechanical microenvironments, such as substrate stiffness, and respond by releasing dense granules and undergoing membrane surface conformational changes [88]. The dense granules can activate nearby platelets and the membrane surface conformational changes can expose the GPI-IbIIIa integrin complex, the platelet-fibrin mediator [77]. The exposure to stiff substrates increases platelet activation, and therefore platelet adhesion and contraction [61]. The ability of platelets to sense microenvironments in the bloodstream and decipher the biochemical and biophysical signals into stages of platelet activation provides a possible physiological explanation of the heterogeneity of clots and thrombi during the coagulation cascade [88].

Since platelets are the building blocks of clots and thrombi, accurately capturing platelet interaction mechanics and dynamics is critical to building a meaningful multiscale model of coagulation. A computational model developed by Mori et al. combined a Stokesian fluid dynamics technique with a viscoelastic model to capture the role that implicitly-modeled fibrin plays in explicitly-modeled platelet-platelet aggregation within in a simple shear scenario [74]. Again in simple shear-flow, Mody et al. performed a series of studies using Platelet Adhesive Dynamics (PAD) to model the traction forces associated with platelet adhesion to an exposed injured vessel wall [69, 71, 70, 72].

We develop a model to capture the primary adhesive role that platelets have in hemostasis. We simulate platelet mechanics in an *ex vivo* environment, i.e. in the absence of flow and surrounding vasculature, with the explicit inclusion of both platelets and fibrin as a means to capture the interplay of platelet-platelet and platelet-fibrin interactions at a higher resolution than existing models.

2.2 Model Development

The DEM-based model of activated platelets captures the mechanics of platelet-platelet and platelet-fibrin adhesion by accounting for the forces from biochemical bonds associated with coagulation, in addition to the frictional and normal forces that are classically considered in execution of this method. Platelets are treated as the explicit discrete elements. The forces acting on a given platelet, i, are calculated according to Equation 2.1, which is modified from Equation 2.1 to include $\vec{F}_s$, a calibrated adhesive spring force that is unique to this implementation of DEM.

$$m_i\frac{d\vec{v}_i}{dt} = \sum (\vec{F}_n + \vec{F}_t + \vec{F}_s) \tag{2.1}$$

Similar to Equation 2.1, m is the particle mass, $\vec{v}$ is the particle velocity, and $\vec{F}_n$ and $\vec{F}_t$ are the normal and tangential body forces, respectively. In this work, the non-adhesive interparticle contacts are modeled using the dampened JKR model for Hertzian contact mechanics [103]. The radius of the contact spot, a, can be expressed as

$$a = \sqrt[3]{\frac{3R^*F_n}{4E^*}} \tag{2.2}$$

where R^* is the effective particle radius and E^* is the effective Young's modulus. The decrease in the normal contact force due to damping is proportional to the product of the normal velocity and the overlap distance of particles in contact. Rotational phenomena is assumed to be small in the presence of adhesion and although the precise modeling of platelet deformation is not considered, a good approximation of the mechanical behavior is still possible.

Platelet membrane surface receptors give rise to the strong adhesive properties of activated platelets that enable the platelet-substrate connections [13]. To capture this adhesive property of platelets *in silico*, we simulate platelets as single particles with implicit springs that represent mediators and membrane receptors. The variable lengths of the mediators are modeled by defining concentric spheres about the *in silico* platelets, whereby the mediator lengths are equal to the radial difference between an outer sphere and the surface of the platelet. Figure 3 shows a schematic of the various mediator lengths defined by the concentric spheres surrounding a platelet.

2.2.1 Rupture Forces

We used the force-distance curves obtained from an AFM experimental investigation of platelet-platelet bond rupture as the basis for the mediator lengths and adhesive contributions [77]. We used a similar experimental study to obtain the platelet-fibrin rupture information to calibrate our model [56]. A schematic of the experimental study used to calibrate the platelet-fibrin interactions within our model is included as Figure 4. To calibrate the platelet-platelet interactions, the fibrin-coated surfaces seen in Figure 4 were replaced with platelet-activating materials and two platelets were positioned within the plates, allowing the platelet-platelet rupture force to be measured. Upon initialization of the experiment, the platelet attached to the top plate was placed in contact with either the fibrin-coated surface or another platelet before the bottom plate was lowered at a constant velocity until the top platelet became detached. The point of detachment was determined by a clear separation between either the top platelet and the fibrin-coated surface or the two platelets.
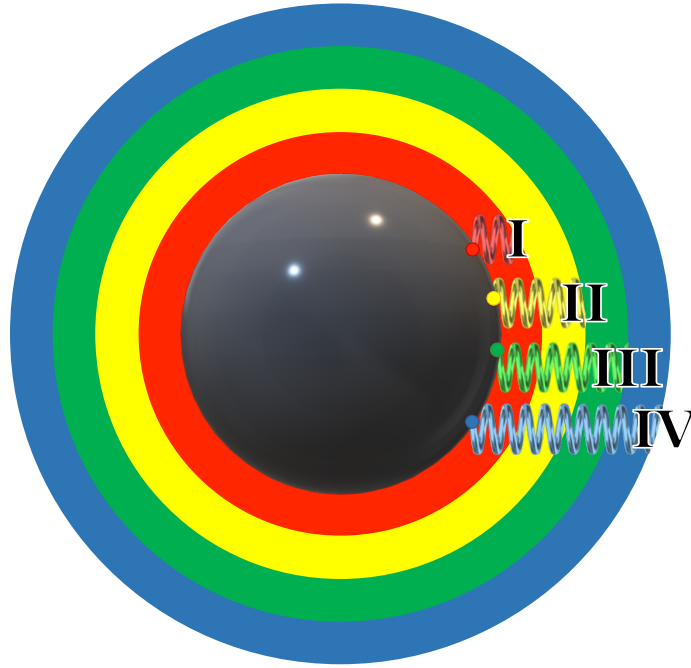
Figure 3: Schematic of a simulated platelet with the four mediator lengths defined by concentric spheres of increasing diameter with Roman numeral labels at the edges of the mediator lengths that correspond to the endpoints of Equation 2.3. The mediator lengths are defined by the distance between the platelet surface and the outer edge of the concentric spheres. Note that the depicted mediator lengths represent a general case and are therefore not to scale.
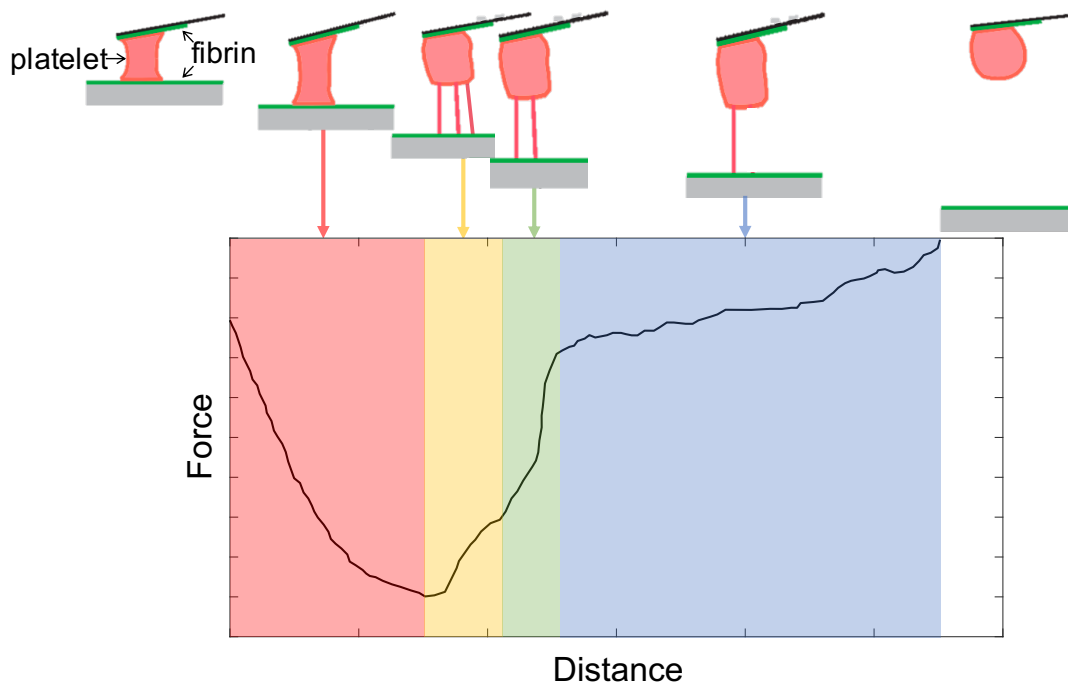
Figure 4: Schematic of the AFM experiment used to measure the resistance force of platelet-platelet and platelet-fibrin adhesive interactions. An activated platelet is placed in contact with either a fibrin-coated surface or another activated platelet and the force required to separate the plates is tracked as the upper plate remains stationary and the lower plate moves in the vertical direction away from the upper plate at a constant velocity. The curve represents the measured force as a function of the separation distance. The colored phases of the force-distance diagram correspond to the ruptured platelet mediators aligned with Figure 3. This figure was adapted from [56].

To implement the different adhesive behaviors, i.e. platelet-platelet and platelet-fibrin, we introduce an implicit spring between a platelet and an adherent substrate, such as fibrin or another platelet. Prior to initializing a simulation, the particle types are designated as either platelet particles or fibrin particles so that the pairwise adhesive interaction is classified correctly as either platelet-platelet or platelet-fibrin. Fibrin-fibrin interactions are handled as described in Chapter 3. The spring forces for each type of adhesive interaction are mathematically defined by continuous piecewise linear functions, where the interval endpoints correspond to the lengths of the mediators. The piecewise linear function for activated platelet interactions is defined as

$$\vec{F}_s(x) = \begin{cases} m_{\text{I}}x + b_{\text{I}}, & 0 \leq x \leq \text{I} \\ m_{\text{II}}x + b_{\text{II}}, & \text{I} < x \leq \text{II} \\ m_{\text{III}}x + b_{\text{III}}, & \text{II} < x \leq \text{III} \\ m_{\text{IV}}x + b_{\text{IV}}, & \text{III} < x \leq \text{IV} \end{cases} \tag{2.3}$$

where $m_{\text{I-IV}}$ and $b_{\text{I-IV}}$ are the slopes and intercepts, respectively, of the corresponding mediator lengths, x is the distance between a platelet particle surface and another adherent surface, and I-IV are the endpoints of the concentric adhesive annuli and/or the platelet mediator lengths. In practice, $\vec{F}_s$ functions to resist the separation between two particles, either two platelets or a platelet and fibrin particle, only after their surfaces have overlapped or the distance between their centers meets a defined adhesive criteria as discussed in Chapter 2.2.2.

2.2.2 Adhesive Loading

Platelet surfaces are coated with filopodial extensions that function to grab nearby platelets or other adhesive surfaces in order to facilitate platelet aggregation [52]. The actomyosin-based contraction mechanics and dynamics of platelets are known to influence the mechanical properties of clots and thrombi by shrinking, stiffening, and rearranging [56]. To gain insight into the mechanism of platelet contraction, single-platelet measurements taken at the point of platelet activation, when the first platelet contractions are possible, are particularly useful [48]. In order to simulate the effects of the platelet filopodial extensions

in silico, we incorporated a capture radius about the platelets. The capture radius is defined as the length of the first mediator, which ranges from 1.9 to 3.1 μm. The adhesive loading force is assumed to be elastic and follows Equation 2.3.

We extended our model to perform platelet contraction, which was observed in an experimental study performed by Lam et al. The study reported the spontaneous platelet activation and contraction of unactivated platelets in the presence of fibrin [56]. In order to capture a desired rate of platelet contraction, we tuned the viscous contribution of the repulsive normal force, Fn, to balance the constant attractive spring force, Fs, which are related by Equation 2.1. Increasing the viscous contribution of Fn, dampens the oscillations that arise from the strong contraction force and the opposing normal force. After validating the platelet-contraction portion, our platelet model captures the mechanics and dynamics of platelet-platelet and platelet-fibrin interactions resulting from the adhesive and contractive power of platelets as shown in Figure 5A. In Figure 5A, a positive force corresponds to an attractive force between interacting particles and a negative force corresponds to a repulsive force. We adjusted the equilibrium position of an adhesive particle pair to account for their soft and flexible nature that results in a small platelet-platelet or platelet-fibrin overlap at equilibrium. The equilibrium spring length or distance between adherent particle centers is less than the diameter of a particle, resulting in particle-particle overlap at equilibrium shown schematically in Figure 5B. Additionally, the spring force governing contraction is zero until a platelet or fibrin particle enters another platelet's contact radius.

2.3 Simulation Results of Rupture Force Studies

2.3.1 Platelet-Fibrin and Platelet-Platelet Adhesion

To capture platelet-fibrin and platelet-platelet adhesion *in silico*, the parameters corresponding to the slopes, intercepts, and endpoints included in Equation 2.3 are fit to the corresponding curves in Figure 6. The fitted parameter values are listed in Table 1. The resulting piecewise linear curves of platelet-fibrin and platelet-platelet adhesive rupture me-

A

Platelet-Fibrinogen Contraction Force

B
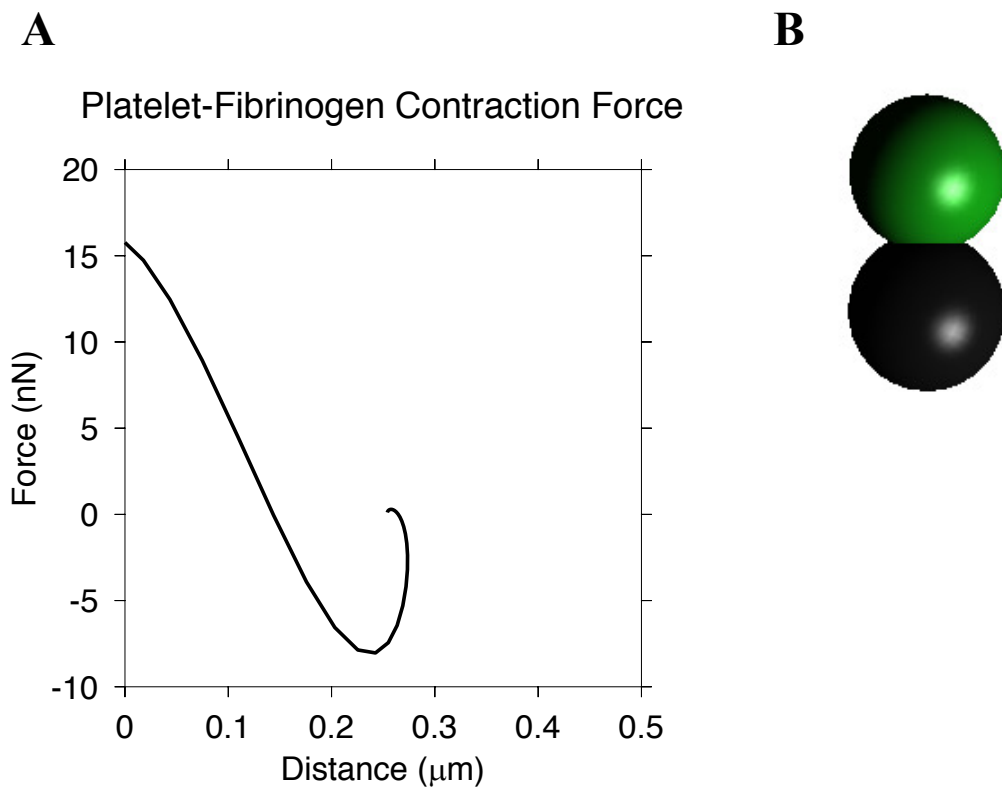
Figure 5: (A) Simulated contact force calculated by the difference between the normal repulsive force and the contraction force between a simulated platelet and a non-platelet particle plotted against the distance between the 2 μm particle centers and (B) the simulation visualization of the equilibrium position between a contracted platelet (black) and a non-platelet particle (green), demonstrating the particle overlap at equilibrium.

Parameters (Units)	I	II	III	IV	m_I	m_{II}	m_{III}	m_{IV}	b_I	b_{II}	b_{III}	b_{IV}
	(μm)				(nN/μm)				(nN)			
Platelet-fibrin	3.1	4.5	5.0	11.0	-22.2	24.6	38.1	0.01	-20.0	-167.5	-227.0	-64.5
Platelet-platelet	1.9	2.2	5.8	6.1	-1.5	2.6	-0.1	1.5	0.0	-9.0	-1.2	-18.0

chanics are included as the colored dashed lines in Figure 6a and 6b, respectively. The colors of the dashed lines correspond to the colored platelet mediators that are depicted in Figure 3.

An observation of the digitized data included in Figure 6a of the platelet-fibrin rupture forces and Figure 6 of the platelet-platelet rupture forces, from Lam et al. and Nguyen et al. respectively, reveals that platelet-fibrin bonds are nearly thirty times stronger than the strongest platelet-platelet bonds [56, 77]. A platelet's maximum rupture force is governed by the shortest (red) mediator and the rupture force measured at the greatest distance is the spring force associated with the longest (blue) mediator before complete separation or rupture. The *in silico* reproduction of the rupture force-distance curves of platelet-fibrin and platelet-platelet adhesion demonstrates that our model is able to phenomenologically capture the mechanics of platelet adhesive interactions as shown in Figure 6.

2.3.2 Platelet-Platelet Subject to Varied Activation

To capture varied platelet activation *in silico*, we implement the same implicit spring between platelet-platelet interactions, but fit the parameters corresponding to Equation 2.3 using experimental force-distance curves obtained by Nguyen et al. in a study of platelet-platelet bond rupture at various degrees of platelet activation. To induce different degrees of activation experimentally, platelets were exposed to glass surfaces passivated with collagen, fibronectin, and poly-L-lysine. The same AFM technique depicted in Figure 4 was performed
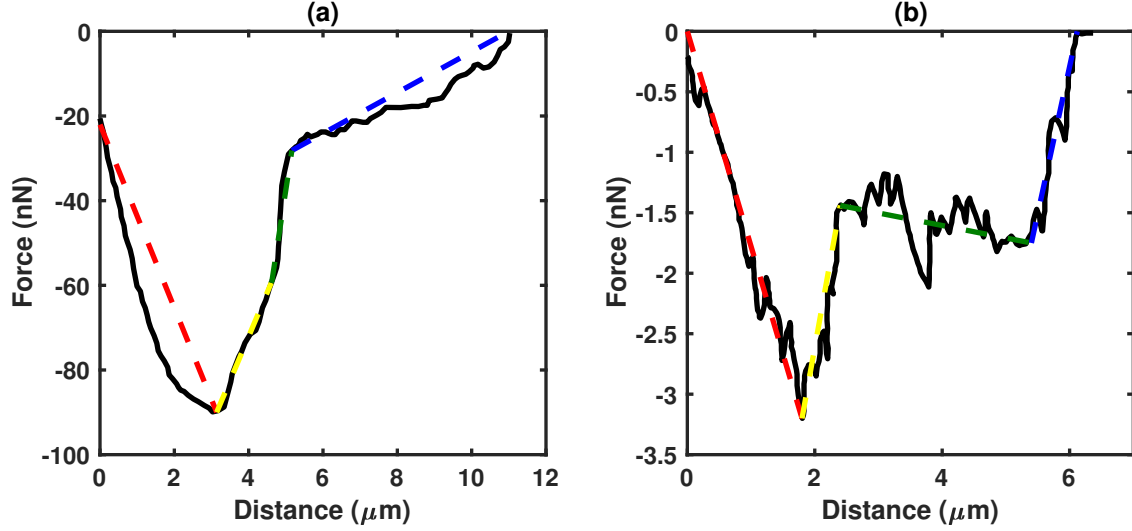
Figure 6: Simulated (– –) and experimental [56, 77] (—) rupture force of platelet-fibrin (a) and platelet-platelet (b) adhesion versus separation distance. The colors of the dashed lines correspond to the colored platelet mediators depicted in Figure 3.

Table 2: Parameter values from Equation 2.3 used to fit curves in Figure 7.

Parameters	I	II	III	IV	m_I	m_II	m_III	m_IV	b_I	b_II	b_III	b_IV
(Units)		(μm)				(nN/μm)				(nN)		
Non-/weakly-activated	1.3	1.6	2.3	4.2	-1.3	0.0	2.3	-4.4	-0.7	0.3	0.7	-2.9
Partially-activated	1.8	2.4	5.0	5.4	-1.2	0.0	2.6	-6.5	-0.3	0.2	3.1	16.9
Activated	1.9	2.2	5.8	6.1	-1.5	2.6	-0.1	1.5	0.0	-9.0	-1.2	-18.0

using the aforementioned passivated glass surfaces in place of fibrin-coated surfaces. We used the experimental force-distance curves obtained in that study to define three distinct degrees of activation, namely non-/weakly-activated, partially-activated, and activated, which correspond to the respective passivated glass surfaces.

The fitted parameter values from Equation 2.3 that correspond to the different degrees of activation are listed in Table 2. The simulation results of the rupture force between two activated platelets at the three degrees of activation are included as the dashed curves in Figure 7. The degree of activation increases in the subplots from left to right. From both experimental and simulation results in Figure 7, it is clear that the strongest platelet adhesive bonds are governed by the platelets activated to the highest degree signified by the curve with the greatest force magnitude on the y axis. Additionally, the initial capture radius and the maximum range of the adhesive interactions increases with each degree of activation. The initial capture radius corresponds with the length of the shortest mediator, as explained in Chapter 2.2.2, is located at the global minimuma of the curves in each subplot of Figure 7. The maximum range of the adhesive interactions, which occurs just before the platelet-platelet bonds completely rupture, corresponds to the point with the greatest distance on the curves in Figure 7. The rupture force curve that corresponds to the activated platelet scenario in Figure 7 is initial platelet-platelet interaction presented in Figure 6. The *in silico* reproduction of the rupture force-distance curves of platelet-platelet adhesion demonstrates that our model is able to phenomenologically capture the mechanics of varied platelet activation.
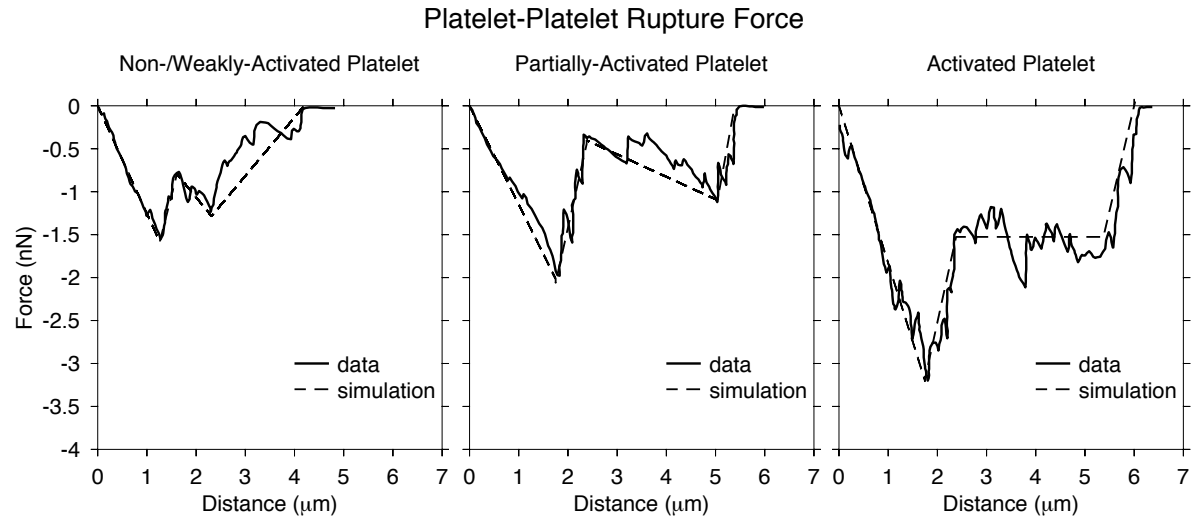
Figure 7: Simulated and experimental rupture forces of platelet-platelet interactions between a non-/weakly activated platelet and (A) a non-weakly activated platelet, (B) a partially-activated platelet, and (C) an activated platelet, plotted against the distance between the two adhering platelet surfaces. Experimental data was digitized from [77].

2.4 Summary

In total, we can implement four levels of platelet activation ranging from inactive (no adhesion) to fully-active (strongest adhesion) that governs platelet-platelet interactions. To do so *in silico*, we introduce a spring force between interacting active platelets. The spring forces for each activation level are mathematically defined by piecewise linear functions, where the Roman numerals or piecewise linear endpoints correspond to the lengths of the mediators. If platelets with dissimilar activation degrees are interacting, the spring force resulting from their interaction corresponds to the piecewise function of the platelet activated at the highest level. Platelet and fibrin interactions can also be modeled in the same manner as platelet-platelet interactions by incorporating a unique piecewise linear description that is calibrated to experimental data from the literature. The spring force that describes the aforementioned platelet adhesive interactions follows Equation 2.3, where x is the distance between a platelet particle surface and either another platelet particle or fibrin. The fitted parameter values that correspond to Equation 2.3 can be found in Table 2 for platelet-platelet interactions of the various activation levels and Table 1 for platelet-fibrin interactions.

A platelet's maximum possible rupture force, which is governed by the shortest mediators, increases with the level of activation [77]. The rupture force measured at the largest distance is the spring force associated with the longest mediator between a platelet and its adherent substrate before complete separation. An observation of the digitized data included in Figure 7 of the platelet-platelet rupture forces and Figure 6 of the platelet-fibrin rupture forces, from [77] and [56] respectively, reveals that platelet-fibrin bonds are nearly thirty times stronger than the maximum platelet-platelet bonds. The level of platelet activation, dictated by its mechanical microenvironment, is the likely determinant of the quantity of granules released and the extent of membrane-surface change, which in turn, could manifest in the variations observed in the rupture force dynamics [77]. The *in silico* reproduction of the rupture force-distance curves corresponding to various levels of platelet activation demonstrates that our model is able to broadly capture the mechanics and dynamics of platelet-platelet and platelet-fibrin interactions.

Our model assumes that all mediators within a given concentric circle shown in Figure 3 rupture and reform simultaneously, thus resulting in the reduced noise compared to the experimental counterpart. A consequence of the simplifying assumption is the absence of the mechanistic detail of platelet-platelet and platelet fibrin interactions. In order to expand the mechanistic accuracy and therefore the goodness of fit of our model to the experimental data, the structure of the single mediator per concentric circle would need to include multiple mediators whose lengths and connectivity vary with a certain degree of stochasticity for each colored concentric circle. With the aim of utilizing the developed cell-scale model as the foundation of a larger, multiscale model, the taken phenomenological approach satisfies the computational feasibility concerns that arise during scale-up of highly mechanistic cell-scale counterparts. The phenomenological cell-scale model of platelet-platelet and platelet-fibrin adhesion presented herein is essential to capturing the micro-mechanical contributions in a multiscale model of coagulation. This model serves as the foundation to examine the collective behavior of platelet and fibrin aggregates that is discussed in subsequent chapters of this dissertation.

3.0 Mechanistic Model of Fibrin Viscoelasticity and Strain-Hardening Extensibility

3.1 Background

Fibrin is a polymer that forms when activated thrombin exceeds a threshold concentration in the presence of endogenous fibrinogen [45]. Fibrin strands assemble during the early stages of the coagulation cascade to form the fibrinous network that spreads throughout a clot and helps to maintain clot integrity *in vivo* under high arterial pressure [112]. Further stabilization can occur through the addition of covalently bonded crosslinks between adjacent fibrin monomers [63]. The formation of fibrin networks contributes to the cessation of bleeding by coupling and contracting nearby platelets to generate a gel-like assembly. The unique mechanical properties of individual fibrin strands, including viscoelasticity and strain-hardening extensibility, facilitate the physiological functionality of these polymers [18, 100]. At the microscale, changes in protein folding and cross-linking can alter downstream fibrin formation and function. At the macroscale or whole-blood level, fibrin stretching and alignment are responsible for changes in blood clot mechanical properties and can be related to disorders and disease [95]. An understanding of the contribution of single fibrin fibers on the whole-blood mechanics is critical for an accurate multiscale model of clot behavior.

Unlike fully elastic solids that deform proportionally under stress and independently of the rate of strain, the deformation of viscous materials, like fibrin, behaves in a way that stress is proportional to the rate of strain but not necessarily proportional to the strain itself [46]. The fractional elastic and viscous components of fibrin will determine the response of a clot or thrombus to an applied external force [53]. Stiff clots and thrombi are able to resist deformation and those with a greater viscous component will return to their original shape more slowly, if at all, once the external force is released [123]. The most widely accepted theory to describe the physiological source of the viscoelastic behavior is the presence of distinct domains within the bundle that expand and contract with dissimilar dynamics [63].

The objective of Chapter 3 is to develop an *in silico* model using Discrete Element Method (DEM) that captures the extensible, strain-hardening, and viscoelastic behavior of individual fibrin bundles. Similar to 2, this chapter also functions as a cell-scale building block of the multiscale model elaborated upon in subsequent chapters.

3.2   Model Development

3.2.1   Fibrin as Springs in Series

Fibrin bundles can exceed a 330% strain before rupturing, though the fibrin integrity is threatened when the elastic limit of the bundle is exceeded, which occurs prior to the point of rupture [63]. *In silico*, we can capture the highly extensible nature of fibrin by modeling fibrin as a chain of adjacent solid spheres or particles connected in series via implicit mechanical springs. The equilibrium spring length (distance between particle centers) is less than the diameter of a particle, resulting in substantial particle overlap at equilibrium. The purpose of the overlapping particles at equilibrium or prior to an extension event is to mitigates physical gaps between adjacent particles at full extension. Aside from the implicit spring interaction between adjacent fibrin particles within a given strand, fibrin particles do not physically interact. Avoiding or ignoring intra-strand fibrin interactions is particularly important because the substantial overlap forced upon adjacent fibrin particles violates the laws of physics and therefore could not be carried out with DEM.

An atomic force microscopy (AFM) experimental investigation was performed by Liu et al. and used to guide the calibration of the *in silico* fibrin particles and strand length [63]. Fibrin particles were assigned a diameter of 0.2 μm, or ten times smaller than the *in silico* platelet particles. The AFM stage from extension study had a width of 12 μm, which corresponds to 59 *in silico* particles when the particles have an initial overlap of two thirds with respect to their diameter. A schematic of a single fibrin bundle at equilibrium is included as Figure 8A.

We can execute an extension-retraction case study on a single *in silico* fibrin strand by freezing the end-point fibrin particles and forcing the center particle to have a specific positive velocity in the vertical direction, followed by the same velocity in the negative vertical direction until the strain of the entire strand returns to zero. Five snapshots of a visualization of the extension portion of this *in silico* case study are compiled as Figure 8, showing the progression from 0-225% strain.
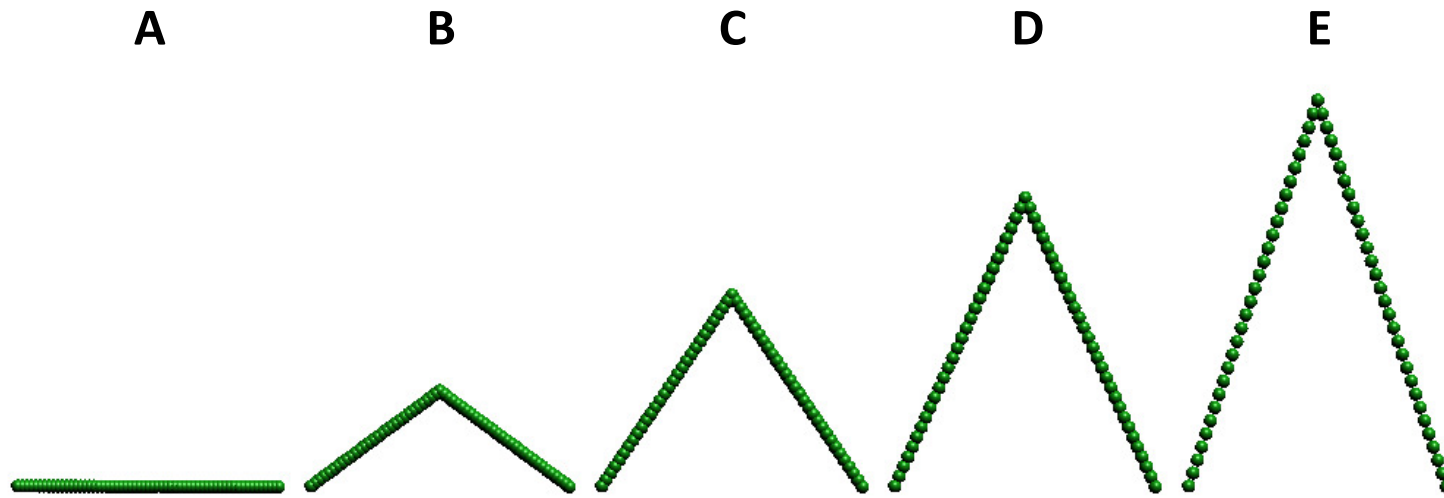
Figure 8: Simulation visualization of (A) the unstretched equilibrium stage of a fibrin strand composed of overlapping particles tethered together by an attractive force between adjacent particles and three intermediate snapshots (B-D) of the progression to 225% strain (E).

3.2.2 Hooke's Law and Hill functions

To capture the strain-hardening and viscoelasticity of the *in silico* fibrin strand, we can mathematically describe the implicit spring that tethers adjacent fibrin particles as a Hookean spring with an elastic modulus of Hill functional form. Since fibrin becomes more viscous with increased strain, the parameters of the Hill function that correspond to the retraction portion of the stress-strain curves are modified as the strain increases [68]. The Hill function parameters for the extension and retraction curves are mapped to experimentally generated data.

We used the force-strain curves obtained from an AFM experimental investigation performed by Liu et al. as the basis for the structure and calibration of our model [63]. Because the experimental data was formatted as *force* versus *strain* (ε), the modular spring coefficient is also a function of strain, where strain is defined as Equation 3.1,

$$\varepsilon = \frac{\Delta L}{L_0} \tag{3.1}$$

where ΔL is the total elongation of the intra-fibrin spring length and L_0 is the equilibrium intra-fibrin spring length. To capture the strain-hardening phenomena in our model, we have incorporated a modular spring coefficient, of Hill-type functional form, into the calculation for the force resulting from the spring between two adjacent particles within a single fibrin strand.

$$F(t) = F(t-1) + k(\varepsilon)\Delta x + \zeta c_c v \tag{3.2}$$

$$k(\varepsilon) = k_0 + \frac{k_{max} \times (\varepsilon)^n}{\varepsilon_M{}^n + (\varepsilon)^n} \tag{3.3}$$

36

The modular spring coefficient, k as defined in Equation 3.3, is a sigmoidal function of the strain of the spring. The k_0 term is the minimum spring coefficient measured at zero strain. k_{max} defines the maximum spring coefficient measured at large strains. ε_M corresponds to the strain at which half maximal force is achieved, and n, the Hill coefficient, determines the rate by which the spring coefficient changes. Equation 3.2 describes the incremental force resulting from the spring that is resolved at each time step by adding the product of the spring coefficient and the displacement $(k(\varepsilon)\Delta x)$ to the force at the previous time-step $(F(t-1))$.

Simple harmonic motion results when there is a restoring force proportional to the displacement, so the third term on the right hand side of Equation 3.2, $\zeta c_c v$, incorporates the dashpot that accounts for the dampened oscillations that are observed *in vitro*. In the third term, v is the velocity of the spring elongation and ζ is the damping ratio defined as Equation 3.4,

$$\zeta = \frac{c}{c_c} \tag{3.4}$$

where c is the actual damping coefficient and c_c is the critical damping coefficient. The critical damping coefficent, derived from Newton's second law, is equal to $2\sqrt{m \times k(\varepsilon)}$, where m is the intra-fibrin particle mass. The damping ratio can vary from undamped ($\zeta = 0$), underdamped ($\zeta < 1$), critically damped ($\zeta = 1$), and overdamped ($\zeta > 1$). Assuming a critically damped system, the magnitude of the actual damping coefficient was equal to that of the critical damping coefficient, or $2\sqrt{m \times k(\varepsilon)}$.

3.3 Results of Fibrin Simulations

3.3.1 Single Extension-Retraction Cycle

We used the extension portion of the force-strain data collected by Liu et al., digitized and included in Figure 9, to heuristically fit the parameters of 3.3. The corresponding modular spring coefficient is plotted versus strain in Figure 10.
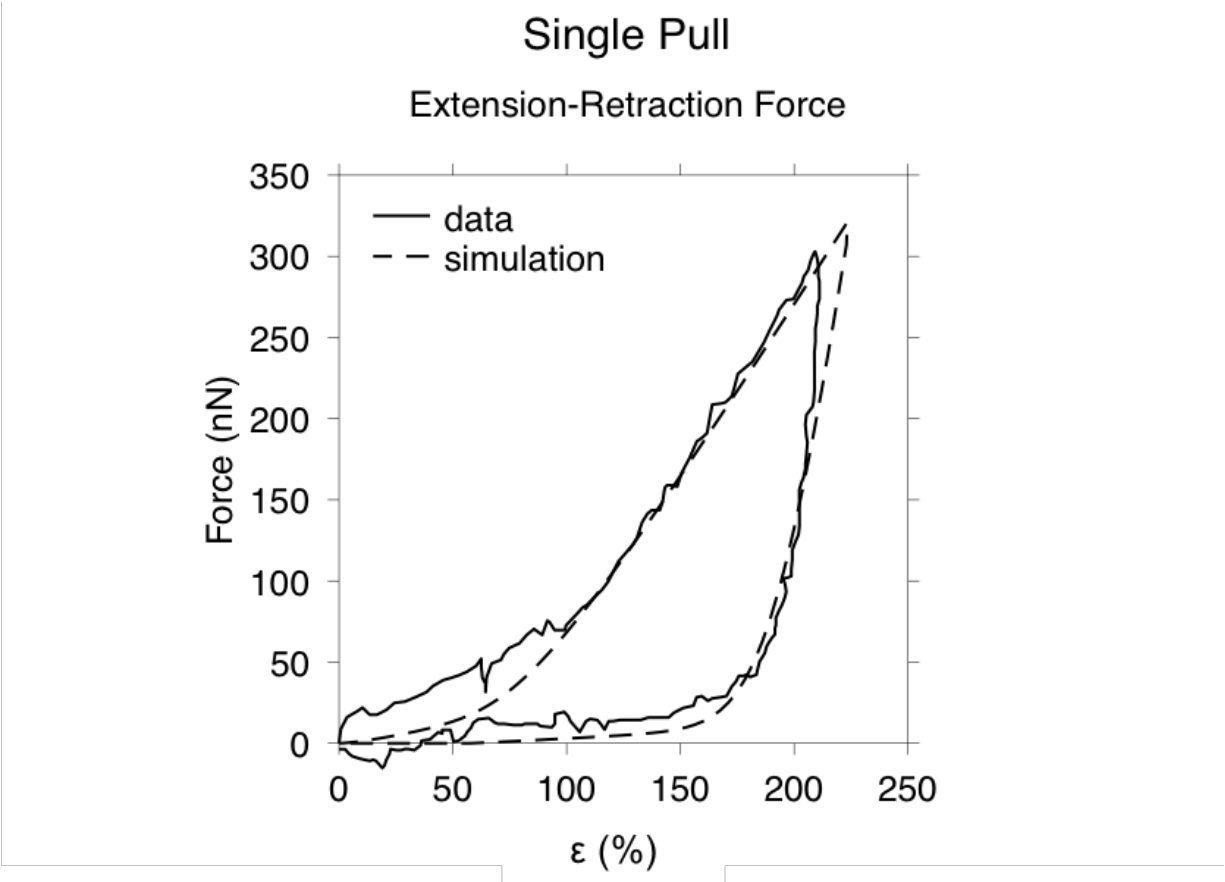
Figure 9: The experimental and simulated force required for a single fibrin strand to extend approximately 225% strain before retracted to complete a single pull for the modular spring coefficients corresponding to Figure 10. Experimental data was digitized from [63].
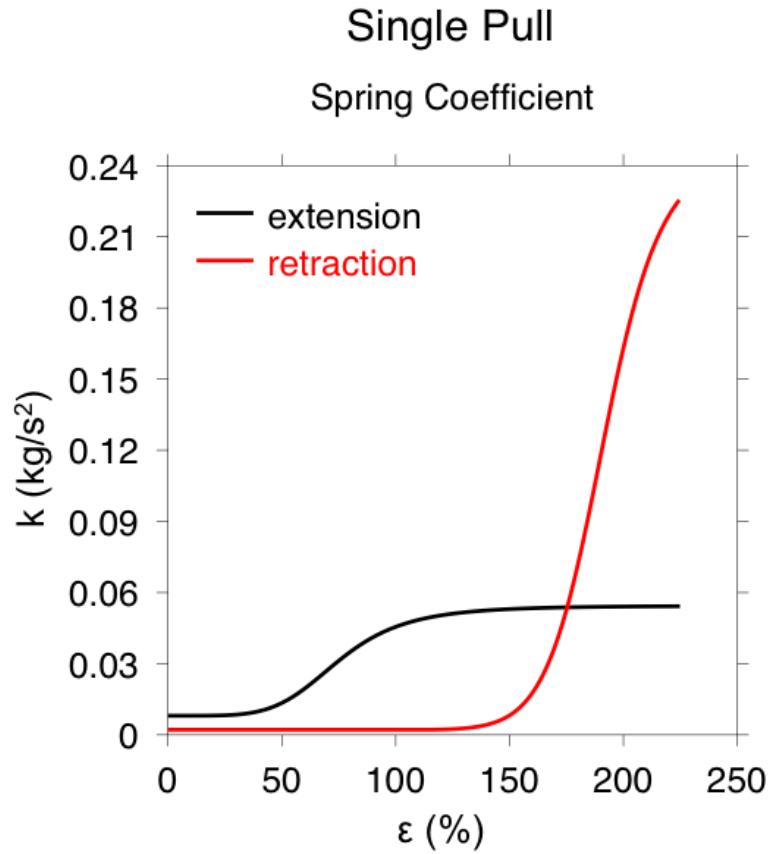
Figure 10: Spring coefficient trajectories used in the attractive force calculation between neighboring particles in a simulated fibrin bundle of three particles extended (red) to approximately 225% strain, prior to retracting (black) to complete a single pull.

Table 3: Spring coefficient Hill function parameters corresponding to Figure 10 for the single extension-retraction scenario of a fibrin strand.

Parameters (Units)	k_0 (kg/s^2)	k_{max} (kg/s^2)	ε_M (% strain)	n (unitless)
Extension	0.01	0.24	75	5
Retraction	0.0025	1.12	190	15

To capture the viscoelastic behavior of fibrin, observed on force-strain curves by the presence of an area between the extension and retraction curves, the Hill function parameters are modified upon retraction when the previous extension exceeds the elastic limit of fibrin (50% strain). From the retraction portion of the curve collected by Liu et al., digitized and included in Figure 9, we know that fibrin has a much higher elastic modulus immediately upon retraction, justifying the increase in k_{max} upon retraction. The slope of the retraction curve changes much faster upon retraction compared to extension, justifying an increase in ε_M and n. Finally, the terminal slope of the retraction curve is less steep than the initial slope of the extension portion, justifying a decrease in k_0 upon retraction. The retraction portion of the force-strain curve in Figure 9 was used to fit the parameters of 3.3 when the spring is retracting. The *in silico* reproduction of the force-strain curve generated in [63] for the constant velocity single extension-retraction case, shown in Figure 9, demonstrates that our model is able to capture the mechanics of fibrin extensibility and strain-hardening viscoelasticity when we simulate a fibrin bundle composed of 59 particles. We first calibrated the system with a strand of three particles before lengthening the *in silico* fibrin strands to contain anywhere from 20-200 particles per strand. Independent of the strand length, *in silico* fibrin strands exhibit the same dynamics upon stretching that are observed with the system used to generate Figures 9-12.

3.3.2   Consecutive Extension-Retraction Cycles

Liu et al. also observed interesting single fibrin strand dynamics during an experiment by extending and retracting the same strand consecutively, increasing the maximum strain with each cycle from 45% to 85% to 125% [63]. With the same Hill-type functional form of the spring coefficient between adjacent fibrin particles within a bundle, we aim to simulate consecutive extension-retraction cycles and observe similar dynamics. Using the same parameter fits for the extension portion of each cycle obtained in Chapter 3.3.1, and fitting the parameters of Equation 3.3 for the retraction portion of the individual cycles in the consecutive extension-retraction case, we can capture the increased energy dissipation that is observed upon consecutive extension-retraction cycles with increasing maximum strain. Following the same justification described in Chapter 3.3.1, the retraction portions of the experimental force-strain curves in Figure 11 were used to heuristically fit the parameters of Equation 3.3 when the spring is retracting in the simulation. The spring coefficient versus strain curves for the three consecutive extension-retraction constant-velocity case are included as Figure 12.

As in Chapter 3.3.1, we first calibrated the system using a strand composed of three particles before extending the *in silico* fibrin strand to contain 59 particles. Noting the departure of our simulation from the experimental data for each cycle of the consecutive extension-retraction case, observed in Figure 11, we can both increase k_0 and simultaneously decrease $k_{m}ax$ for the extension case. Increasing K_0 alone would improve the model fit in the low-strain elastic regime, but worsen the fit at larger strains. The steps in the Hill function parameters of the retraction spring coefficient (k_{max}, ε_M , and k_0), which result from fitting the individual cycles independently, create inherent discontinuities that would be observed if a simulated fibrin bundle were to be retracted between the strain ranges simulated in Figure 11. To eliminate the steps between the model parameters, general functional forms of k_{max}, ε_M, and k_0 with respect to the maximum strain of the bundle as means to create continuity and promote model stability. In doing so, predictions of the behavior of fibrin strands that are extended and retracted between and beyond the strain ranges reported experimentally by [63] would be possible. Following the justification described in Chapter 3.3.1 and from an

41
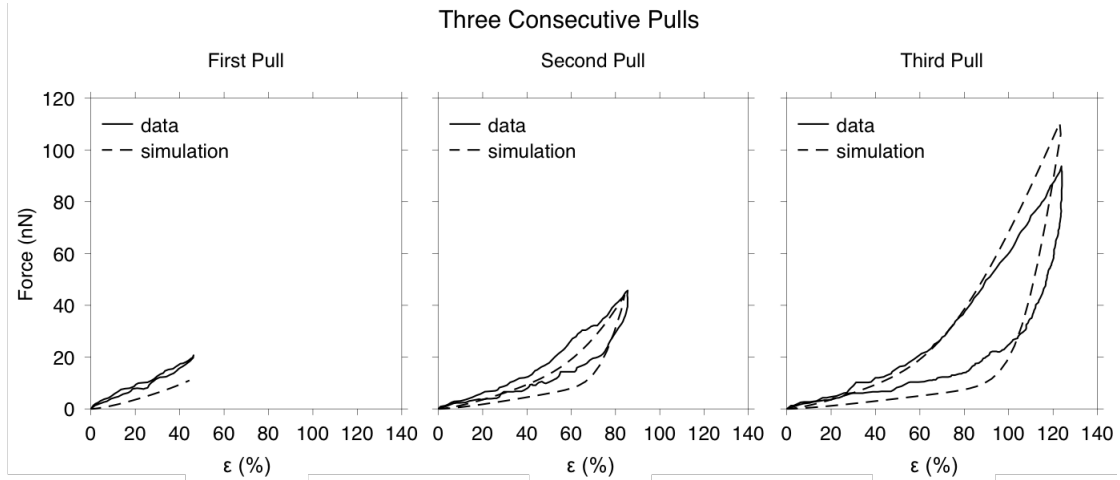
Figure 11: The experimental and simulated force required for a single fibrin strand to extend to a maximum 45% strain on the first pull (left), 85% strain on the second pull (center), and 125% strain on the third pull (right) for the modular spring coefficients corresponding to Figure 12. Experimental data was digitized from [63].
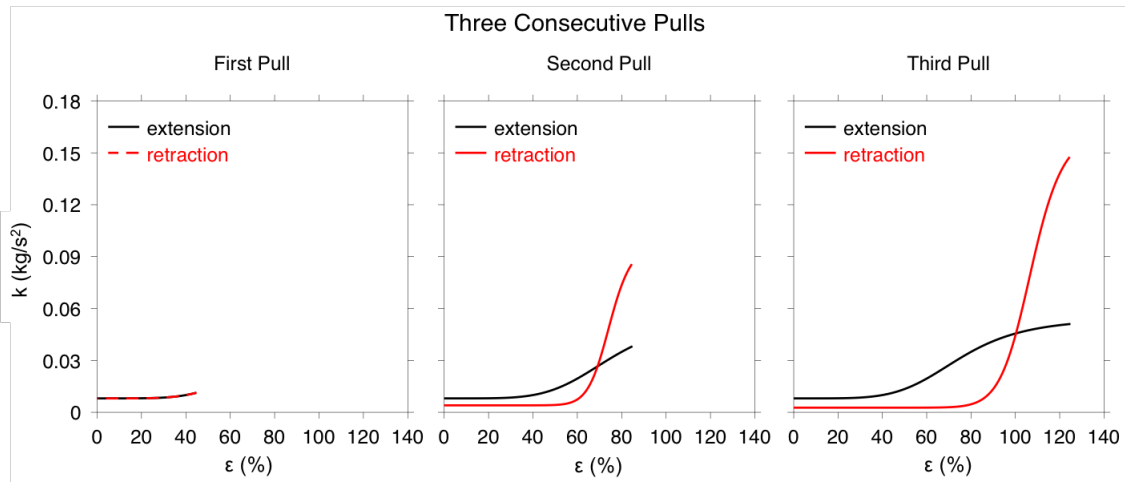
Figure 12: Extension and retraction spring coefficient trajectories used in the attractive force calculation between neighboring particles in a simulated fibrin bundle of three particles extended to a maximum 45% strain on the first pull (left), 85% strain on the second pull (center), and 125% strain on the third pull (right).

Table 4: Spring coefficient Hill function parameters corresponding to Figure 10 for the consecutive extensions-retractions scenario of a fibrin strand.

Parameters (Units)	k_0 (kg/s^2)	k_{max} (kg/s^2)	ε_M (% strain)	n (unitless)
Extend/1st Retract	0.01	0.24	75	5
2nd Retract	0.005	0.45	75	15
3rd Retract	0.0033	0.75	110	15

observation of the current fitted parameter values included in Table 4, k_0 will be a decreasing function of the maximum strain, while both k_{max} and ε_M will be increasing functions of the maximum strain.

3.4 Summary

In Chapter 3, the unique mechanical properties of fibrin can be captured *in silico* by modeling fibrin strands as chains of small particles linked together with implicit springs. The springs behave according to Hooke's Law with a variable spring coefficient that is mapped to experimental data. The isolated fibrin strand *in silico* model is capable of capture the high extensibility, strain-hardening, and viscoelastic behavior of *in vitro* fibrin.

The modular elastic modulus of fibrin at increased strains is evident by a nonlinear slope on the extension portion of its stress-strain curve [63, 44]. Specifically, the slope of the stress-strain curve increases in magnitude or steepness with increased strain. At low strains, the slope, or elastic modulus is constant because stress is directly proportional to strain. At large strains, the slope increases dramatically, exhibiting a phenomena known as strain-hardening. Strain-hardening behavior is believed to result from the increased availability of contact sites on fibrin at large strains and consequently enables clots and thrombi to stiffen in scenarios with increased deformation that could otherwise induce clot breakdown [123].

43

We calibrated the implicit spring force between neighboring particles of the same strand to extension-retraction data from *in vitro* fibrin. The mechanical properties can be measured from stress-strain curves obtained by applying a stress, or a force per unit area, to the polymer and recording the resulting strain, or the stretch of the polymer normalized to its initial length [123]. From *in vitro* extension-retraction studies of single fibrin bundles, the distinct mechanical properties can be quantified. Specifically, the degree of strain-hardening is observed by a comparison of the steeper slope at larger strains to the initial slope steepness of stress-strain curves [63]. The viscoelastic behavior is evident by the departure between the extension and retraction curves, where the area between the curves is proportional to the energy dissipated [62].

The calibrated single *in silico* fibrin strand mechanics from Chapter 3 results in an *in silico* DEM-based model that captures the extremely extensible, strain-hardening, and viscoelastic behavior of individual fibrin bundles. The model from this chapter functions not only as a stand-alone entity, but also as a building block for a multiscale model that includes fibrin networks composed of hundreds to thousands of strands. The fibrin network simulations are explored in Chapters 4 and 5.

4.0 *Ex Vivo* Platelet Aggregate Formation

4.1 Background

The focus of Chapter 4 is the development of a model that incorporates fibrin networks into the cell-scale adhesive mechanics model from Chapter2. The trans-scale gap is traversed to study the emergent behavior of assemblies of platelets and fibrin. Specifically, we investigated how variations in blood composition of key blood components lead to different qualitative and quantitative descriptors and pathologies. We can define relationships between the concentrations of blood coagulation contributors and corresponding aggregate morphologies, void size distributions, and permeabilities.

Several other models have been developed in recent years that are also motivated by the essential role of platelet adhesive interactions during coagulation. These studies have focused on the aggregatory behavior of activated platelets under various hemodynamic conditions. Pivkin et al. have developed a 3D model using Dissipative Particle Dynamics (DPD) that captures the reduced accumulation of platelets in the presence of red blood cells [84]. Other studies developed continuum platelet aggregation models, based on PDEs, by considering only the fluid phase and tracking platelets concentrations [29, 120]. While the contributions of these platelet aggregation models are noteworthy in this space, the rules governing the platelet attachment and activation stage are not validated by experimental work. Xu et al. developed a 2D discrete model that combined the discrete Cellular Potts Model (CPM) of platelet and blood cell aggregation with continuous partial differential equations (PDEs) describing the hydrodynamics of blood flow and the kinetics of coagulation reactions [127]. Despite the biological detail that was incorporated into the CPM hybrid model, the morphologies of the resulting simulated clots were not aligned with their experimental counterparts. Mody and King constructed a 3D platelet aggregation model, named Platelet Adhesive Dynamics (PAD), which captures a growing thrombus by considering individual receptor-ligand bonds under simple shear flow. Although the PAD model does not incorporate the effect of platelet activation, the model accounts for the non-sphericity of platelets,

45

which is typically ignored in most coarse-grained models [69]. Mori et al. applied Voigt's model, a spring and dashpot pair, to capture the adhesive behavior between platelets and two plasma proteins, vonWillebrand Factor (vWF) and Fibrinogen [74]. Though a simple model, it provides mechanistic insight on thrombus formation and rupture. These researchers have used different computational approaches to model platelet adhesion and aggregation, but few have investigated the effect that component concentrations have on aggregate properties [58, 105, 116].

Using a discrete element method (DEM)-based approach, the three-dimensional model developed herein investigates the morphological and mechanistic differences of aggregates formed from varied compositions of platelets and fibrin. We considered platelets to be solid spheres and describe the adhesive platelet-platelet and platelet-fibrin bonds using implicit springs. The adhesive interactions were first calibrated to experimental data from isolated platelet experiments [56, 77] before the simulations were expanded to include hundreds to thousands of platelets, aligned with the conditions at the core of a clot or thrombus.

We considered two general scenarios of fibrin incorporation in our model that we believe provide a simple yet effective manner to identify the critical role that fibrin plays during coagulation and the diverse effect it can have on resulting clot morphology. In both fibrin scenarios, we varied the platelet concentration from roughly 0.8-32 percent solid by volume. The simulation results allow us to observe and compare the aggregates as a function of fibrin structure and platelet concentration. The spatial variation was quantified by calculating the void size distribution within the aggregates and their corresponding permeabilities. This model as a whole can provide insight on the mechanism of platelet aggregation and the potential effect of pathologic fibrin on aggregate formation.

4.2 Model Development

4.2.1 Platelet and Fibrin Aggregate Generation

To investigate the aggregatory behavior of activated platelet assemblies, we expanded our simulations from isolated platelet-platelet and platelet-fibrin interactions at the cell-scale to include hundreds to thousands of platelets within a $4.2e5$ μm^3 three-dimensional periodic framework. The number of *in silico* platelets included in each simulation was determined by the desired solid volume fraction of platelets, which ranged from 0.008-0.32 and assumed 2 μm-diameter spherical platelet particles. The set platelet range corresponds to a platelet count that would be representative of the concentration present at a clot core or platelet plug. To initiate the simulations, the platelets were randomly placed within the 3D simulation box by assigning their x, y, and z coordinates from a uniform distribution and ensuring that no two particles overlapped. At runtime, the platelets were given a slow random velocity to facilitate the particle collisions. Particle interactions resulted when any pair of particle centers had three radii of separation. The additional halo of adhesive contact allowed particles to spontaneously interact before their surfaces made physical contact, which is aligned with a platelet's ability to grab nearby platelets [15]. Each simulation was run to a pseudo-steady state, defined by a 25 μs or longer plateau of the median interaction force across all of the simulation contacts.

To execute the implicit handling of fibrin within the simulations, platelet-platelet interactions simply behaved as platelet-fibrin interactions, aligned with the platelet-fibrin parameter values listed in Table 1 from Chapter 2 to define the magnitude of the piecewise spring force from Equation 2.3. The initial conditions for the implicit fibrin scenario for four different simulations with platelet concentrations ranging from 0.008-0.32 solid by volume are included in Figure 13a. Each of the four concentrations was simulated in triplicate with uniquely randomized initial particle positions and velocities.

To handle fibrin explicitly, fibrin was included as rigid and immobile cylinders of finite length. The diameter assigned to the fibrin cylinders was an order of magnitude smaller than the platelet particles, or 0.02 μm. The network of fibrin cylinders was generated prior
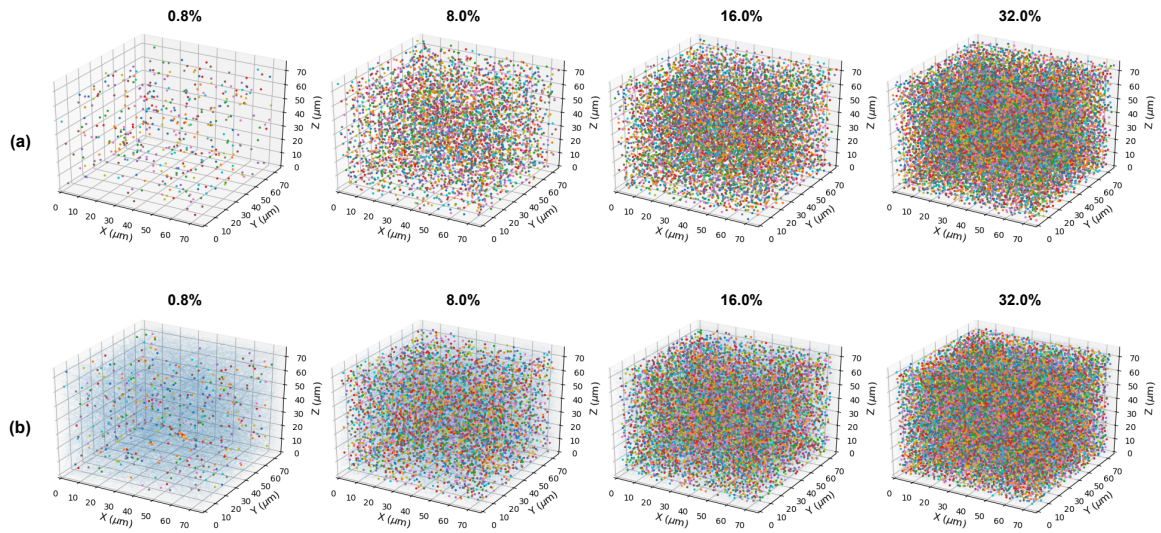
Figure 13: Initial conditions of aggregates within a 75 μm x 75 μm x 75 μm simulation framework for both the implicit (a) and explicit (b) inclusion of fibrin and 0.8%, 8.0%, 16.0%, and 32.0% platelets by volume. Platelets are represented as colored dots and explicit fibrin as blue lines.

to placing the *in silico* platelet particles into the system. Each fibrin cylinder was defined by its two endpoints whose positions were assigned at random to one of the six faces of the simulation box. Fibrin cylinders were added to the system until the solid fibrin volume fraction reached 0.03. The random assignment of the fibrin endpoints created variability in the overall organization of the aggregates between each simulation, which can be qualitatively explained by differences in the quantity, orientation, and length of the fibrin cylinders. An example of the background fibrin mesh is included in Figure 14 for the $4.2e5$ μm^3 system.

In the simulations with explicit fibrin, platelet-platelet and platelet-fibrin adhesive interactions followed their respective spring force parameter values that are listed in Table 1 of Chapter 2. The initial conditions for the explicit fibrin scenario with 0.03 solid fibrin by volume and 0.008-0.32 solid platelets by volume are included in Figure 13b. Each of the four platelet concentration conditions was simulated in triplicate with uniquely randomized initial platelet positions, platelet velocities, and fibrin cylinder positions.

4.2.2   Platelet Nearest Fibrin Neighbors Search

Because the simulations were executed with periodic boundary conditions and fibrin was modeled as cylinders of finite length, an additional step in the traditional nearest neighbor search was required to identify the potential fibrin cylinders that were interacting with platelets located near the simulation boundaries. We developed an automated search method that is summarized schematically in Figure 15 for the instance that a platelet is located in the corner of the simulation framework.
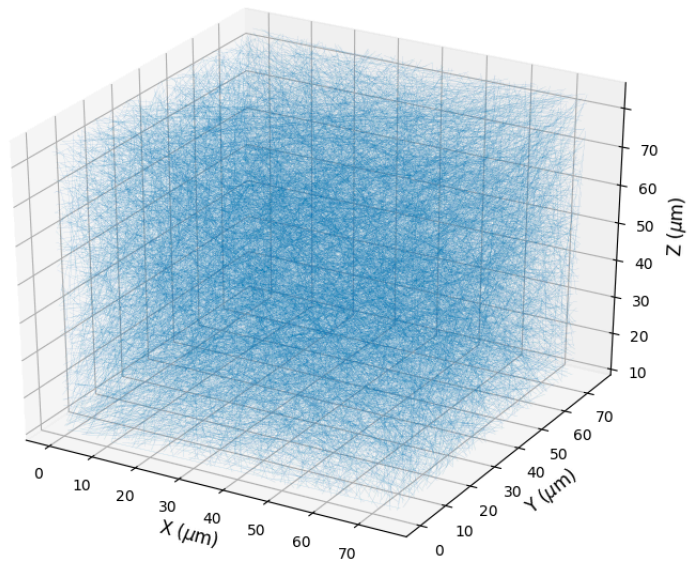
Figure 14: Example of the fibrin network made up of system-spanning cylinders with end-points located at the system walls of a 75 μm x 75 μm x 75 μm framework. The fibrin cylinders are represented as blue lines.
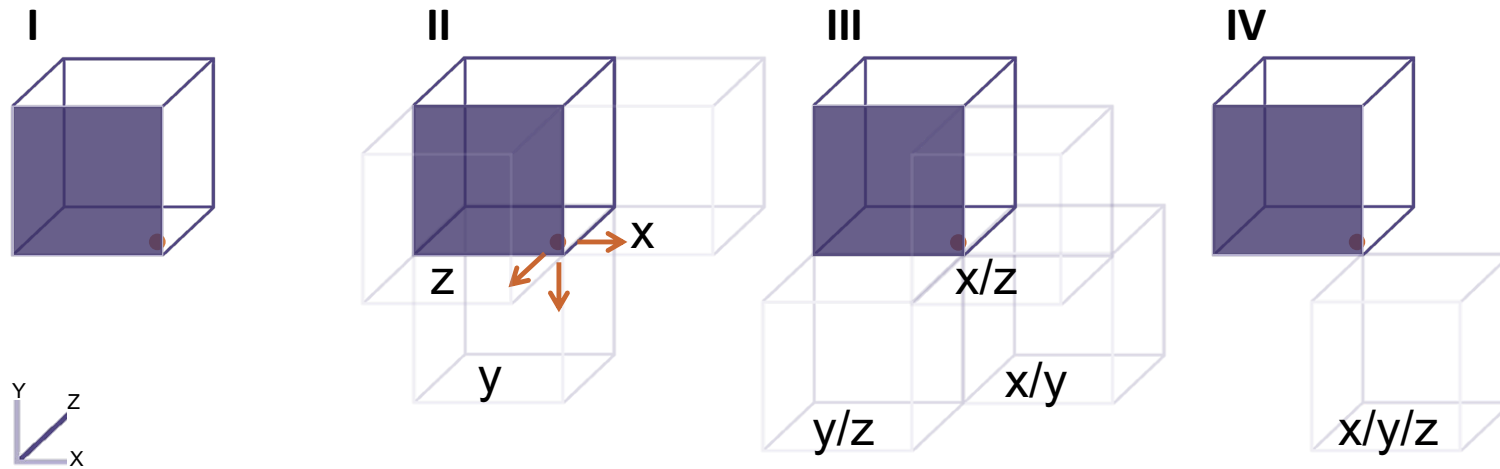
Figure 15: Schematic of the search method used to detect the nearest fibrin neighbors to platelets (orange particle) located near a vertex of a simulation unit cell with periodic boundaries. Nearest fibrin neighbors are first identified in the original unit cell (I) before they are identified in the adjacent unidirectional unit cells (II), bidirectional cells (III), and lastly the diagonal unit cell (IV).

Table 5: The seven adjacent and "self" unit cells that correspond to the example scenario from Figure 15 and are searched within for interacting fibrin cylinders. Each adjacent search cell is named by the coordinate direction it is positioned with respect to the "self" or the original unit cell. The search cells are assigned a one or zero if interactions are possible or not with the platelet of interest.

Search Box	*self*	X	Y	Z	$X+Y$	$X+Z$	$Y+Z$	$X+Y+Z$
Yes/No	1	1	1	1	1	1	1	1

In general, when a platelet is located near a vertex, the method searches in the seven neighboring simulation frames. Due to the periodicity of the simulations, the neighboring frames are repetitions of the unit cell. If a platelet lies near an edge, the method searches in three neighboring cells (two unidirectional and one bidirectional), and if a platelet is near a face, just one (unidirectional) neighboring cell is searched. The adjacent unit cells to be searched are assigned as true as shown in Table 5. To execute the actual search in a given adjacent cell, the *in silico* platelet is effectively repositioned by adjusting its position according to Table 6. The inclusion of this additional step to the nearest neighbors search algorithm enables the aggregates to form system-spanning networks in the presence of high platelet concentrations.

4.3 Results of Platelet Aggregate Simulations

4.3.1 Morphology and Porosity

The steady-state DEM results for the platelet aggregates formed from both the implicit and explicit inclusion of fibrin are included as Figure 16. Qualitative morphological differences can be observed across fibrin inclusion scenarios and platelet concentrations. These differences can be quantified and provide pathological implications. Particularly apparent

Table 6: The adjustments to the *in silico* platelet position that are necessary for the corresponding "self" or imaginary nearby search boxes to be searched, where Nx, Ny, and Nz are the simulation sizes in the X, Y, and Z directions, respectively, if the values in Table 5 indicate *true*.

	X	Y	Z
self	0	0	0
X	$\pm Nx$	0	0
Y	0	$\pm Ny$	0
Z	0	0	$\pm Nz$
$X + Y$	$\pm Nx$	$\pm Ny$	0
$X + Z$	$\pm Nx$	0	$\pm Nz$
$Y + Z$	0	$\pm Ny$	$\pm Nz$
$X + Y + Z$	$\pm Nx$	$\pm Ny$	$\pm Nz$

in the 8.0% and 16.0% solid platelets by volume cases shown in Figure 16a, the absence of explicit fibrin enables the formation of large voids as platelets aggregate into separate isolated clusters or network-like structures. The spatial arrangement of the aggregates formed in the lowest (0.8%) and highest (32.0%) concentrations for both fibrin scenarios are very similar from a qualitative perspective. In the low concentration regime, the initial platelet positions are far apart, so little particle-particle adhesion occurs. In the high concentration regime, independent of fibrin inclusion method, the higher packing fraction and resulting close proximity of the platelets facilitates a higher frequency of adhesive interactions.

To quantify the spatial arrangement of the aggregates, the pore size distributions (PSDs) were estimated by calculating the three-dimensional Delaunay Triangulations from the final platelet positions using the *delaunayTriangulation* function in MATLAB as validated by Zhang et al. [131]. The probability density functions (PDFs) of the PSDs and cumulative PDFs of the PSDs that correspond to the aggregate results shown in Figure 16 are included
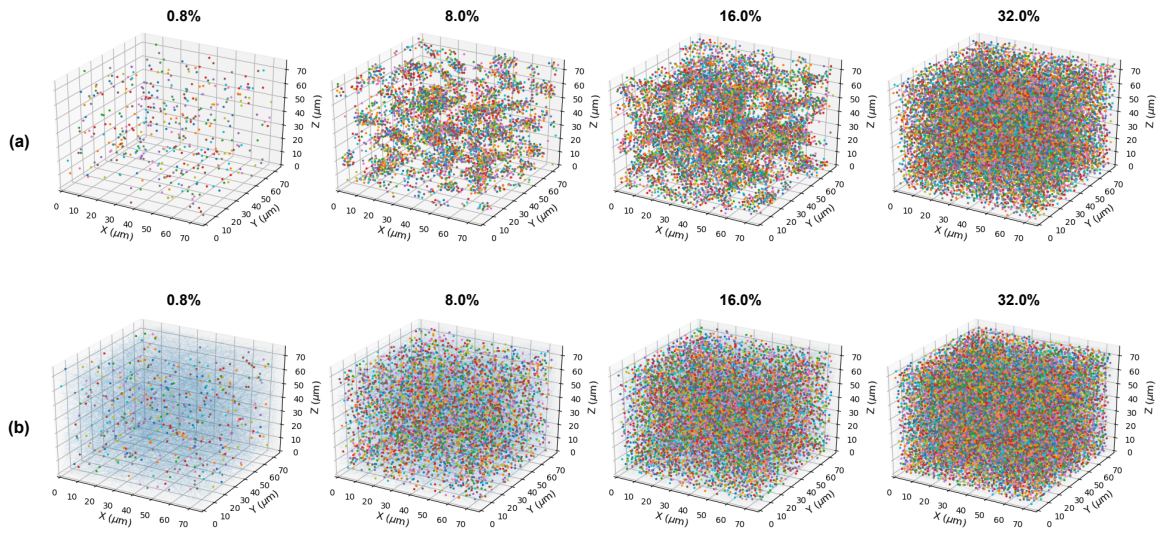
Figure 16: Resulting aggregates within a 75 *µm* x 75 *µm* x 75 *µm* simulation framework formed from implicit (a) and explicit (b) inclusion of fibrin and 0.8%, 8.0%, 16.0%, and 32.0% platelets by volume. Platelets are represented as colored dots and explicit fibrin as blue lines.
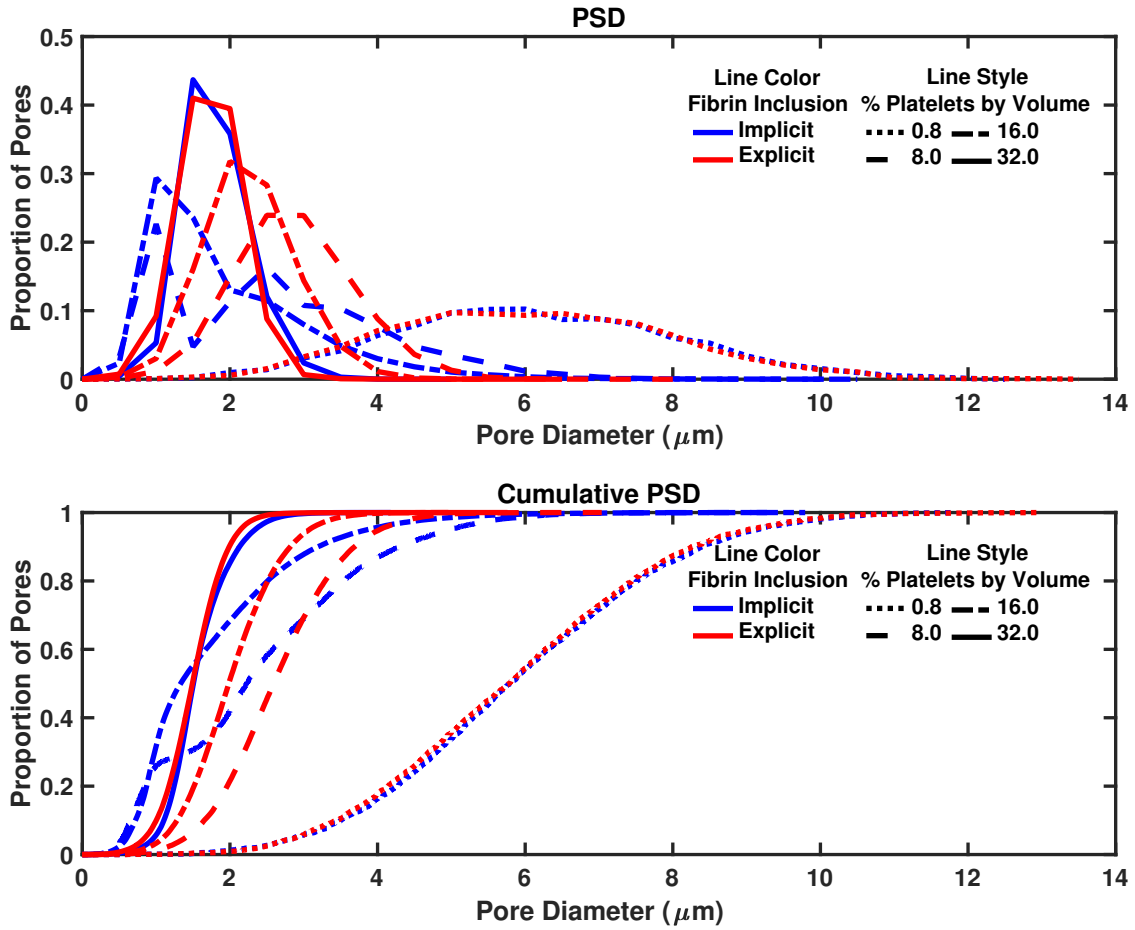
Figure 17: Probability density functions of pore size distributions (top) and cumulative probability densities of pore size distributions (bottom) of *platelets only* within aggregates formed from implicit and explicit consideration of fibrin *in silico* at 0.8%, 8.0%, 16.0%, and 32.0% platelets by volume.

as Figure 17. The line color distinguishes the fibrin scenario (implicit versus explicit) and the line style distinguishes the platelet concentrations. In Figure 17, the fibrin particles are excluded from the PSD calculation for the explicit fibrin scenario, leaving only platelets to be considered in the PSDs for both fibrin scenarios. Figure 17 summarizes the effect that fibrin structure has on platelet organization during aggregation. The PSD results recapitulate the qualitative spatial arrangement observations. In general, as the platelet concentrations increase and void volumes decrease, the distributions become increasingly right-skewed as the platelet concentration increases, corresponding to a decrease in the dominant pore diameter. The variance across the distributions decreases with increasing platelet concentration, indicating that the maximum pore size decreases with increasing platelet concentration. In the highest and lowest platelet concentrations considered, the PSDs for both fibrin scenarios nearly overlap, indicating no spatial dependency of aggregate formation on fibrin length, stiffness, or mobility when the platelet concentration is above 32.0% or below 0.8% by volume.

On the contrary, the PSDs for the 8.0% and 16.0% platelet concentration cases do show a sensitivity to the fibrin scenario. As seen in Figure 17, the tails of the PSDs for these concentrations in the implicit fibrin scenario extend further to the right than the respective tails belonging to the explicit fibrin scenario. By modeling the fibrin implicitly, physical fibrin in this scenario could be either extremely short or long and flexible, thereby providing an environment that would facilitate the formation of large pores or void volumes during platelet aggregation. The multimodal distributions associated with the implicit inclusion of fibrin stem from the existence of the isolated aggregates. The smaller intra-aggregate pores form the left-most peaks and the inter-aggregate pores form the broader secondary peaks.

Figure 18 is included to show the effect of stiff and immobile fibrin (green curves) on the PSD within the aggregates. The red curves are the same across Figures 17 and 18. When the fibrin particles are considered in the calculation of the aggregate PSDs, the largest pores shrink to 2 μm in diameter, the size of a single platelet, which is 5x smaller than the pores within the aggregates formed from the implicit fibrin scenario. The overlap of the four green PSD curves indicates that the pores are largely governed by the fibrin structure and have little sensitivity to platelet concentration. The aggregates formed from the explicit
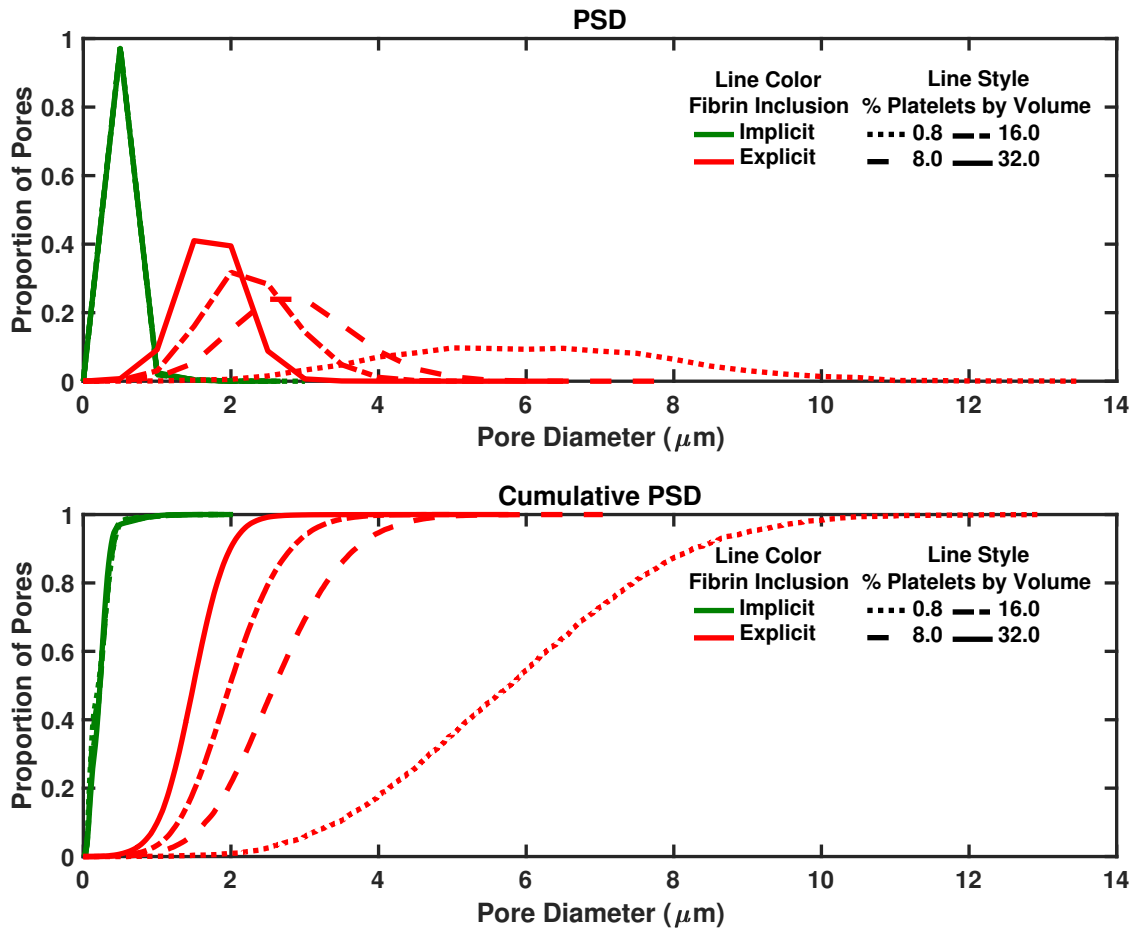
Figure 18: Probability density functions of pore size distributions (top) and cumulative probability densities of pore size distributions (bottom) calculated from *platelets only* (red) and *platelets and fibrin* (green) within aggregates formed from the explicit inclusion of fibrin at 0.8%, 8.0%, 16.0%, and 32.0% platelets by volume.

inclusion of fibrin lack the large voids that are observable in the implicit fibrin scenario because the rigid and immobile fibrin cylinders provide a stiff scaffold that sterically hinders the aggregating platelets. The distinguishable PSDs that evolve from the simulated platelet aggregates identify the platelet gap sizes that regulate the transport of signaling factors and control downstream clot integrity [105].

4.3.2 Permeability of Aggregates

Aggregate permeabilities were calculated by employing D3Q19 LBM simulations with the Bhatnagar-Gross-Krook single relaxation time collision operator approximation, which was explained in Chapter 1.4.2.

Cylindrical solid boundaries were defined around the aggregates generated from the DEM simulations and a periodic boundary was defined in the direction of the cylinder length. The interface of a fluid-solid boundary was handled as a no-slip boundary by implementing bounce-back (reflected) velocities. To minimize error in the permeability measurements, the radius of the cylinder boundary was ten nodes less than the length of the DEM samples. This ensured that the aggregates spanned the radius of the cylindrical opening and that no gaps existed between the aggregates and the walls, aside from the expected voids within the aggregates. Poiseuille flow, parallel to the length of the cylinder, was induced via a constant pressure gradient boundary condition. In the direction of flow, additional fluid nodes were added at both ends of the cylinder.

The platelet aggregates were coupled with LBM by assigning at least ten lattice nodes to each platelet diameter. In the case of explicit fibrin inclusion, it was necessary to increase the node to platelet resolution from ten to thirty lattice nodes in order to accommodate the order of magnitude diameter differential that exists between platelets and fibrin. As a means to increase the lattice resolution while maintaining a computationally feasible system, a smaller sample with comparable solid volume fraction of platelets and fibrin was first extracted from the larger platelet-fibrin aggregates. The samples extracted from the larger platelet-fibrin aggregates were ten platelet diameters in length in order to eliminate the effect of media length on permeability [121]. The fibrin cylinders from the DEM simulations were replaced
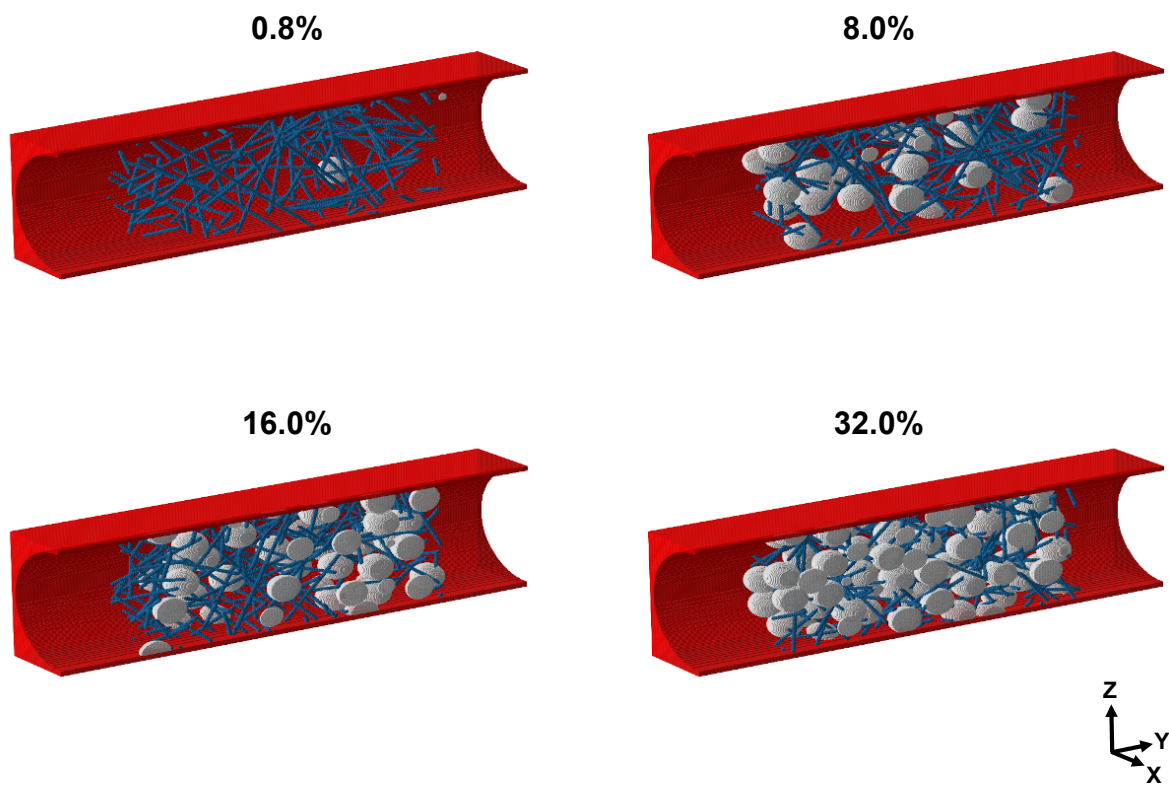
Figure 19: Cross-sections ($X > \frac{1}{2}X_{max}$) of LBM solid nodes represented as filled voxels of platelet-fibrin aggregate samples extracted from larger DEM-generated aggregates composed of 0.8%, 8.0%, 16.0%, and 32.0% platelets (white) and 3.0% fibrin (blue) by volume within a cylindrical solid boundary (red).

with chains of adjacent spheres that were ten times smaller in diameter than the platelet spheres. The corresponding aggregate samples can be visualized by filling the solid voxels from the LBM simulations, as shown in Figure 19. The cylinder wall is red, platelets are white, and fibrin is blue. Voxels with $X > \frac{1}{2}X_{max}$ are not shown in order for the interior of the cylinder to be visible.

The permeability of porous media can be calculated with Darcy's law, which is defined as,

$$q = -\frac{k}{\mu}\nabla p \tag{4.1}$$

where q is the interstitial flux, k is the permeability, μ is the dynamic viscosity of the percolating fluid, and p is the pressure. In the constant pressure gradient boundary condition scenario that we implement, any changes in permeability that results from changes in both aggregate organization and void fraction are observed as changes in the measured fluid flux at steady state. A pressure drop of $3e{-}10\ Pa/m$ was chosen to ensure laminar flow and a Mach number less than 0.1 so that compressibility of the fluid could be ignored.

The LBM simulation results are included in Figure 20 for the implicit (a) and explicit (b) fibrin inclusion scenarios. The permeabilities of the DEM-generated platelet and fibrin aggregates that were calculated from LBM simulations are plotted in Figure 21, along with experimental permeabilities of *in vitro* platelet and fibrin aggregates from literature [125]. Consistent with the literature, the permeability of the simulated aggregates decreases exponentially with increasing platelet concentration. The implicit and explicit inclusion of fibrin in our model influenced the structural morphology and pore size distributions within the emergent aggregates, which directly affected the aggregate permeabilities. The reduced overall permeability that is observed in the case of explicit inclusion of fibrin when compared to the implicit fibrin case is a result of both the lowered void volume and the small pore sizes that are introduced by the presence of the fibrin particles.

For the LBM-derived permeabilities, the different rates of change of permeability with respect to platelet concentration within the two classes of fibrin inclusion are correlated to the sensitivity of the pore size distribution to changes in the platelet concentration. Exemplified in Figure 17 by the distinguishable blue curves, the PSD of aggregates formed from implicit fibrin are highly sensitive to the platelet concentration. Dissimilarly, the overlapping green
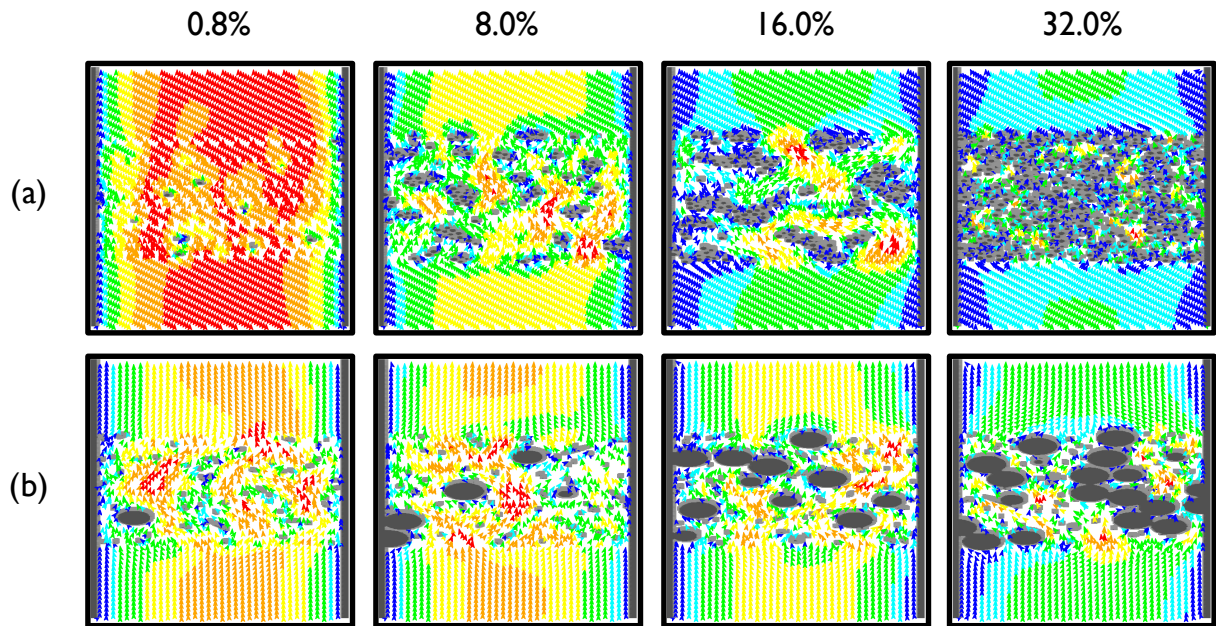
Figure 20: X-Y cross sectional visualization of steady-state simulation results from LBM simulations of flow through aggregates formed via implicit (a) and explicit (b) fibrin scenarios at 0.8%, 8.0%, 16.0%, and 32.0% solid platelets by volume. Solid nodes are represented as gray squares and fluid nodes as arrows in the direction of the flow with colors showing the normalized magnitude of the flow velocity. The velocity field within each frame of this figure was normalized independently.
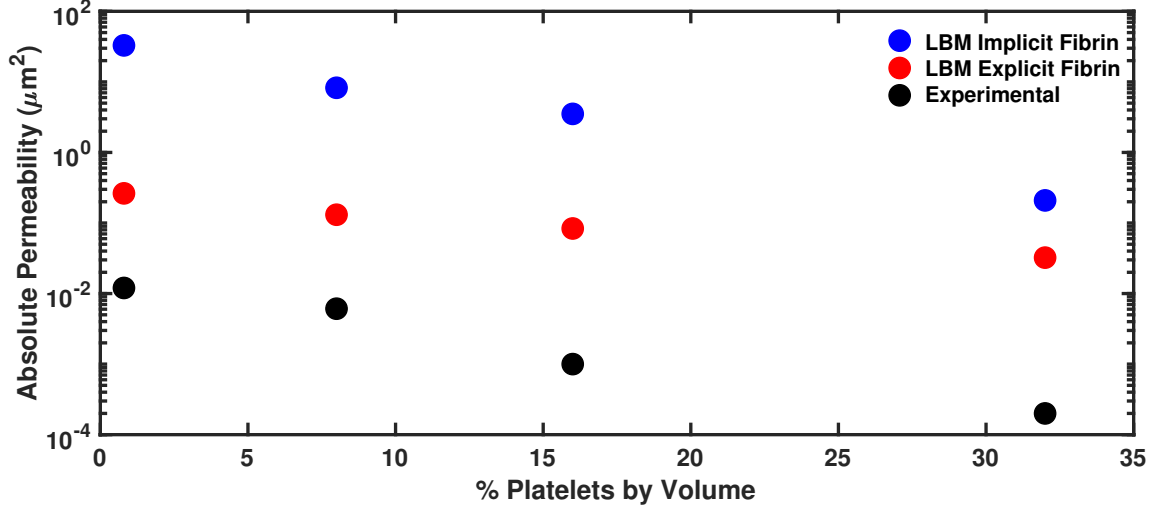
Figure 21: Absolute permeabilities of aggregates calculated from LBM simulations of flow through aggregates formed via implicit and explicit fibrin scenarios and experimental permeabilities obtained from [125].

curves in Figure 18 indicate a lower sensitivity of PSD to platelet concentration. From Figure 21, it is apparent that for the same increase in platelet concentration or decrease in void fraction, the decrease in permeability of aggregates formed from the implicit fibrin scenario is greater than the decrease in permeability for the explicit fibrin inclusion. The reason for this is that in the implicit fibrin scenario, the mean pore size and the variance of the distribution decreases with increasing platelet concentration, but for the explicit fibrin scenario, the PSDs remain the same.

The departure of the experimental permeabilities from the simulated permeabilities is a result of the assumed sphericity of platelets. In reality, platelets are soft and flexible. Upon activation and during aggregation, the deformation of platelets enables their small volumes to cover larger surface areas to impede blood loss and effectively reduce the aggregate permeabilities [77]. However, if platelet activation is compromised or a certain pathology induces platelet hardening, the simulated results from our model propose that these pathologies would result in leaky clots with weak or compromised coagulation capacity.

4.4 Summary

Through the development of a DEM-based model of platelet aggregation, we have investigated the influence of platelet concentration and fibrin inclusion on the emergent clot morphologies. Grounding the platelet adhesive mechanics in isolated single platelet experimental results from the literature, we first calibrated individual interactions before scaling-up our simulations to capture aggregatory behavior. We manipulated the method of fibrin incorporation in our model to simulate two pathological scenarios. We handled fibrin implicitly to identify the influence of extremely flexible and/or short fibrin bundles and explicitly to investigate the effect of inflexible and immobile fibrin.

After simulating the formation of aggregates across the fibrin inclusion scenarios and the desired platelet concentrations of 0.8-32.0% by volume, the morphological differences of the emergent platelet plugs were quantified. We calculated the aggregate permeabilities by executing LBM simulations of fluid flow through the resulting aggregates. Despite the departure from experimental counterparts due to the assumed platelet sphericity, we identified a greater sensitivity of the aggregate permeabilities to platelet concentration in the implicit fibrin scenario. The increased sensitivity of the aggregate permeabilities in the case of implicit fibrin can be explained from the underlying variability of the PSDs. Without stiff and immobile fibrin, increasing in the platelet concentration decreases the mean and variance of the corresponding PSDs. However, in the presence of stiff and immobile fibrin, the number of pores decreases, but the PSDs are insensitive to an increase in platelet concentration.

The simulated fibrin scenarios herein create the bounds of expected platelet behavior during aggregation. The results allow us to observe and compare aggregate formation as a function of fibrin structure and platelet concentration. These findings have important implications for mass transport during clot formation. This model as a whole provides insight into the mechanism of platelet aggregation and the potential effect of pathological fibrin on aggregate formation. Furthermore, it can be used to support the design of drug delivery strategies to control the formation and lysis of blood clots.

5.0 Platelet and Fibrin Aggregate Dynamics

5.1 Background

The focus of Chapter 5 is the development of a model that translates the combined platelet and fibrin adhesive mechanics from the previous chapter (Chapter 4) into a dynamic framework, as a means to study the sensitivity of platelet concentration and adhesive capacity on overall aggregate strength. The first step toward a more dynamic framework includes the implementation of the flexible and mobile fibrin model, calibrated in Chapter 3, into network-like fashion. Modeling the fibrin network as a rigid scaffold of immobile rods, as implemented in Chapter 4, provided the foundation for the conversion to a flexible and mobile network explained in this chapter. Using a discrete element method (DEM)-based approach, the three-dimensional model developed herein investigates the mechanical differences of aggregates formed from varied platelet concentrations and adhesive capacities. Consistent throughout this thesis, we considered platelets and fibrin to be solid spheres and describe the adhesive platelet-platelet and platelet-fibrin bonds using implicit springs. The adhesive interactions were first calibrated to experimental data from isolated platelet experiments [38, 53] before the simulations were expanded to include hundreds to thousands of platelets and fibrin strands, aligned with the conditions at the core of a clot or thrombus.

To investigate the *in silico* platelet and fibrin aggregate dynamics, we used the model from Chapter 4 to generate a pseudo-steady state arrangement of the aggregates at various specified conditions. After replacing the stiff and rigid fibrin cylinders with flexible chains of fibrin particles, we simulated a uni-axial stretching experiment by forcing the velocity of the top wall of the simulation box in an upward direction. We tracked the force on the wall that resisted the wall displacement as a metric for the aggregate strength. By executing a fibrin-control scenario in the absence of platelets, we can compare the relative increase in the magnitude of the resistance stress upon the addition of platelets to calculate the platelet contribution to the aggregate strength.

In vitro, the platelet component of clot strength can be inhibited with the application of glycoprotein IIb/IIIa receptor antagonist [90]. The platelet component of clot strength is measured in the clinic by comparing TEG tracings with and without the platelet adhesion antagonist. The difference in the TEG tracings before and after the application of the platelet adhesion antagonist is equated to the platelet component of clot strength, which is then used to guide the transfusion of platelets in the treatment of coagulopathies [98]. We can use platelet component metrics from *in vitro* samples, reported in Ranucci et al., to calibrate the comparable *in silico* outcomes from the dynamic platelet and fibrin aggregate simulations explored in this chapter [90].

5.2   Model Development

5.2.1   Initial Condition Generation

To investigate the dynamical and mechanical properties of the *in silico*-formed aggregates of platelets and fibrin from Chapter 4, we monitored the response of a simulated continuous uni-axial stretch on the system and tracked the force that resisted the aggregate expansion. To generate the initial conditions for the aggregate extension studies, we executed the same aggregate formation simulations with three-dimensional periodic boundary conditions according to Chapter 4.2.1. The volume of the simulation framework was 5.6e3 μm^3 with a length to width to height ratio of 3:3:5. The fibrin concentration was 3% and the platelet concentrations ranged from 0.8 to 32% solid by volume. The network of fibrin was held constant across the extension studies so as to eliminate the effect of fibrin organization and arrangement on the resistance stress measurements. The constant fibrin network arrangement enabled the isolated effect of platelet concentration and activation level.

To capture the unique dynamics that fibrin exhibits upon stretching, the immobile fibrin strands, modeled as rigid cylinders in Chapter 4, were replaced with chains of small particles linked together with implicit springs as established in Chapter 3. The fibrin particles that composed each fibrin strand were positioned equidistantly along the lines defined by two end

points. The endpoints of the lines were assigned at random to the faces of the simulation framework. Given the two endpoints, $p_a = (x_a, y_a, z_a)$ and $p_b = (x_b, y_b, z_b)$, and the fibrin equilibrium spring length, s_0, the fibrin particles were added in the direction of p_a to p_b according to Equations 5.1 and 5.2.

$$p_{n+1} = (1 - u) \times p_n + u \times p_b, \tag{5.1}$$

$$\text{where } u = \frac{s_0}{\sqrt{(x_b - x_n)^2 + (y_b - y_n)^2 + (z_b - z_n)^2}} \tag{5.2}$$

Fibrin particles were added in sequence until the euclidean distance between the current fibrin particle, p_{n+1}, and the final, p_b, was less than or equal to the equilibrium spring length. The number of fibrin particles that filled each strand varied across the set of strands depending on the length of the original fibrin line/cylinder. The adjacent fibrin particles within the same strand were connected by implicit springs that behaved according to Equation 3.2, where the modular spring coefficient was defined as Equation 3.3. The parameter values of Equation 3.3 are listed in Table 3. A schematic of the resulting fibrin network with fibrin strands composed of adjacent particles is shown in Figure 22A.

To capture the cross-linked nature of the *in silico* fibrin networks, we modified the initial condition of the fibrin network by fusing fibrin strands that intersected. In practice, one of the two most-overlapped particles from intersecting strands is removed and the remaining particle becomes tethered to the two nearest neighbors of the particle that was removed. Following Figure 23IA, this means the two most-overlapped particles from intersecting Strands 1 and 2 are fibrin particle 4 from Strand 1 and fibrin particle 9 from Strand 2. In this case, fibrin particle 9 from Strand 1 is removed and the particle indices from Strand 2 are adjusted accordingly. Fibrin particle 4 (blue) from Strand 1 gains two spring neighbors, particles 8 and 9 (gold) from Strand 2, aligned with Figure 23IB. Multiple strands can be involved in a single cross-linking site, similar to the schematic representation shown in Figure 23II. In this case, the three most-overlapped particles from the three intersecting strands are determined and the fibrin particles with the greater indices (9 and 15) are removed and the remaining fibrin particle (4) is assigned four new spring neighbors (8, 9, 13, and 14). There is no limit

66
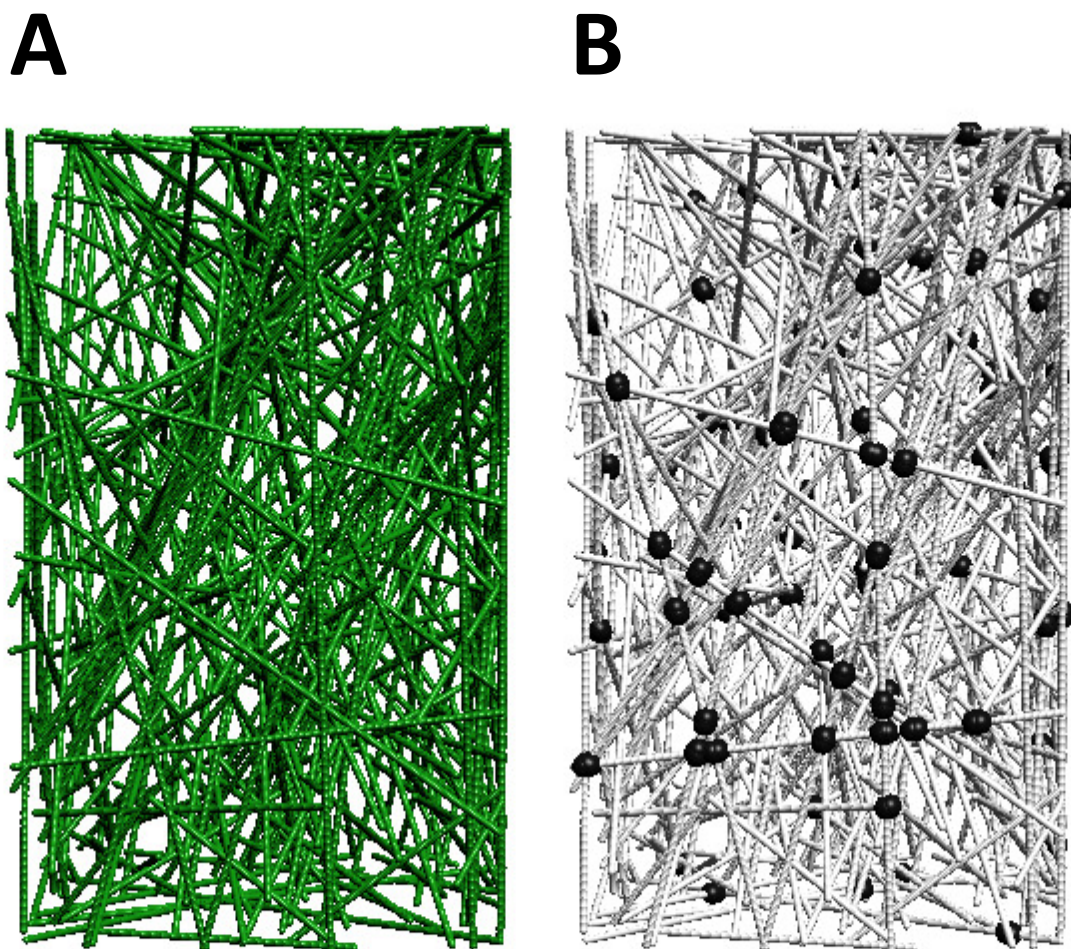
Figure 22: Schematic of the fibrin network used for simulations within Chapter 5 with fibrin strands composed of adjacent green spheres in A and crosslinked particles highlighted as larger black spheres and non-crosslinked particles as white spheres in B for the same fibrin network. There are a total of 45,387 particles within this system.
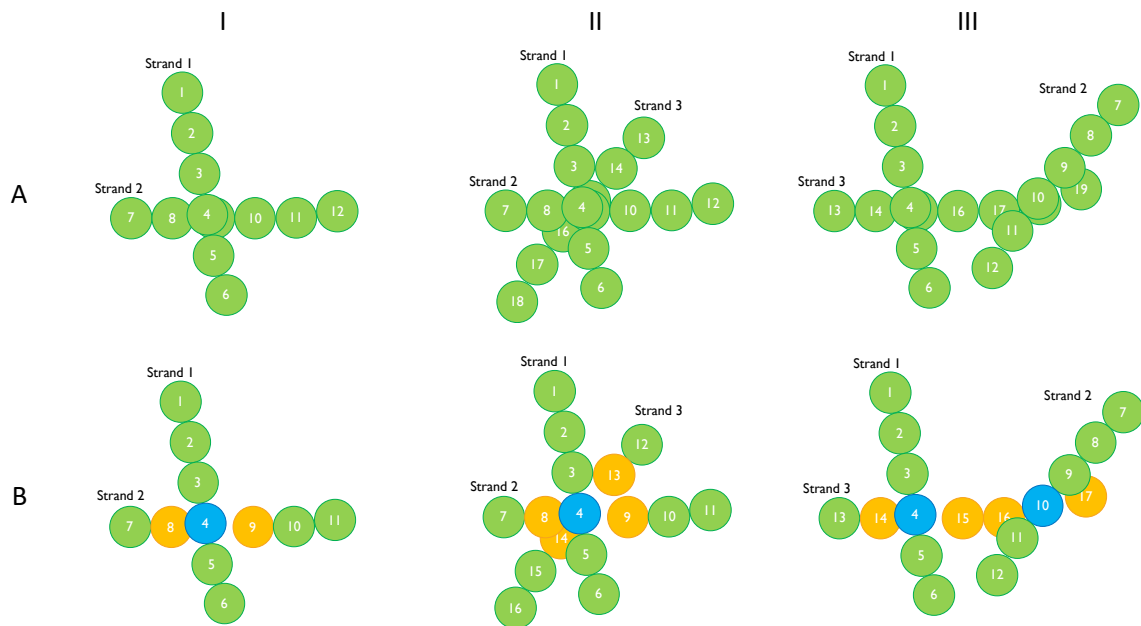
Figure 23: Three cases (I, II, and III) of fibrin strand overlap that were considered for cross-linking within the larger fibrin network. Row A shows the original fibrin strands with all fibrin particles included and row B shows cross-linked strands, where the particle highlighted in blue gains the two gold neighbors that belonged to the particle that the blue replaced.

to the number of spring neighbors a given fibrin particle can have. A particular fibrin strand can also intersect nearby strands at separate sites as shown schematically in Figure 23III. In this case, the particle replacement and new spring neighbor assignments are determined as they were in case I from Figure 23. The fibrin network used for the simulations within this chapter is shown in Figure 22, where the cross-linked fibrin particles are highlighted in part B by representing them as enlarged black spheres and the remaining fibrin particles as smaller white spheres.

$$\text{interacting pairs} = \frac{N \times (N - 1)}{2} \tag{5.3}$$

$$\text{interacting pairs} = \frac{P \times (2 \times N - P - 1)}{2} \tag{5.4}$$

For simplification and computational feasibility purposes, we ignored the inter-strand fibrin particle interactions, which reduces the possible fibrin interactions to the nearest-neighbor interactions within a strand or intersecting strands and platelet-fibrin adhesive interactions. As a result, the number of potential interactions that can occur is substantially reduced, which increases the speed of the simulations. When the fibrin-fibrin interactions are not considered, the number of possible interacting pairs reduces from Equation 5.4 to Equation 5.3, where N is the number of total particles (platelets + fibrin) and P is the number of platelets.

$$\text{pair index} = j - i + \frac{i \times (i + 1)}{2} \tag{5.5}$$

$$\text{pair index} = i \times N + j - \frac{i \times (i + 1)}{2} - 1 \tag{5.6}$$

Schematically, the reduced number of interactions can be visualized by eliminating the fibrin-fibrin interactions from the lower right section of the grid of interaction indices shown in Figure 24. The indices of the interaction pairs must then be adjusted to eliminate the fibrin-fibrin interactions by filling the grid in a row-wise manner instead of column-wise. To accommodate the change in the grid filling direction from vertical to horizontal, Equation
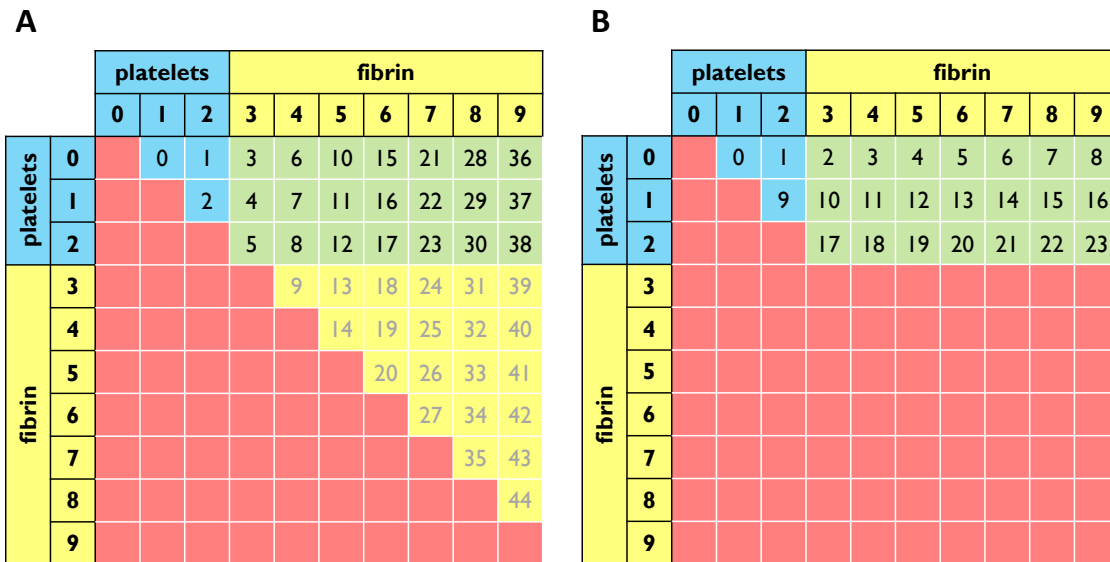
Figure 24: Schematic of the interaction index grid for a test system composed of 10 particles, including 3 platelets and 7 fibrin. The indices identifying the unique interaction pairs of A are calculated with Equation 5.5 and the pair indices of B are calculated with Equation 5.6, where in both cases i corresponds to the index of the particle along the row, j to the index of the particle along the column, and N to the total number of particles.

5.6 is used in place of Equation 5.5, where i and j correspond to the indices of the interacting particles, $i > j$, and N is again the total number of particles (platelets + fibrin).

Fusing the sites where fibrin strands intersect fosters the network connectivity, even in the absence of fibrin-fibrin interactions. The effective cross-linking allows any and all perturbations to the system to be felt throughout the network in a computationally feasible manner.

5.2.2   Aggregate Extension Simulation Setup

To implement a continuous uni-axial stretch of the platelet and fibrin aggregates, a layer of particles parallel to the x-z plane and located at the bottom of the fibrin network was colored red and frozen in place to ground the platelet and fibrin aggregate. A separate layer of particles that was also parallel to the x-z plane, but located at the top of the fibrin network, was colored yellow and given a positive velocity in the y-direction of approximately 0.74 m/s. A visualization of the fibrin network with colored layers to identify the wall particles is included as Figure 25A. As the yellow band of particles moved in the positive y-direction and effectively stretched the system, the resistance to the stretch was measured by adding the force of the particle interactions at the wall interface. The simulations were run until the displacement of the system was stretched a total distance of 4 μm.

Prior to implementing the bands of frozen particles, an alternative simulation setup for the continuous system stretching was considered in which two additional layers of particles designated as wall particles were positioned around the aggregate. One layer was placed above the aggregate to simulate the top wall with a forced velocity in the positive y-direction and the second layer was placed beneath the aggregate to simulate the bottom wall that was frozen in place to keep the aggregate grounded during the extension studies. A visualization of the fibrin network with additional layers of particles to function the aggregate walls is included as Figure 25B. The addition of non-biological particles to function as the system walls introduced complexities that were eliminated by deeming portions of the aggregates that were already present as wall layers. The unnecessary complexities included the properties of the particles themselves, which could have artificially altered the results away from

physiology. The biggest concern was how to handle the wall-aggregate interface because it was somewhat artificial and would be challenging to calibrate. In the end, the principle is the same with respect to including walls on the aggregate ends that are parallel to the direction of the stretching motion, but the interactions with the wall are grounded in physiology and either platelet-fibrin, platelet-platelet, or fibrin-fibrin interactions.

The thickness of the wall of the fibrin aggregate was varied to determine the minimum wall thickness that maintained a reasonable degree of connectivity throughout the aggregate. The range of explored thicknesses corresponded to the sizes of the particles included in the simulations. The smallest wall thickness of 0.2 μm aligns with the *in silico* fibrin particle diameter and 2.0 μm is the diameter of the *in silico* platelet particles. Two additional wall thicknesses of 0.4 and 0.8 μm were also investigated. Schematics of the initial conditions of the four cases of varied wall thickness are included as Figure 26.

As a metric of the aggregate connectivity, the number of contacts with the wall and the force on the wall resisting aggregate extension were measured as a function of the wall thickness for the four aforementioned wall thickness scenarios. The measurements were taken at the endpoint of the simulations, defined as a displacement of the top wall equal to 4 μm. The number of contacts with the wall and the corresponding force on the wall increases with respect to the wall thickness, but at different rates. The secondary y-axis for both plots included in Figure 27 shows the normalized ratio of remaining contacts and remaining force on the wall relative to the thickest wall scenario of 2 μm for 27a and 27b, respectively. When the wall thickness decreases from 2 μm to 0.8 μm, 14 contacts with the wall are lost, or $\sim$90% of the contact points remain. However, the force resisting the aggregate extension reduces by $\sim$40%, meaning that the interactions responsible for the 10% increase in wall contacts when the wall thickness increases from 0.8 μm to 2.0 μm hold a significant weight with respect to the aggregate connectivity that they facilitate. The shift from a linear relationship with respect to contact and force reduction in the 0.2 μm to 0.8 μm range to a nonlinear relationship in the 0.8 μm to 2.0 μm range justified using 2.0 μm-thick walls for the simulations executed herein.

The initial positions of the platelets within the fibrin networks were taken from the pseudo-steady state positions of the aggregate formation simulations explained in Chapter
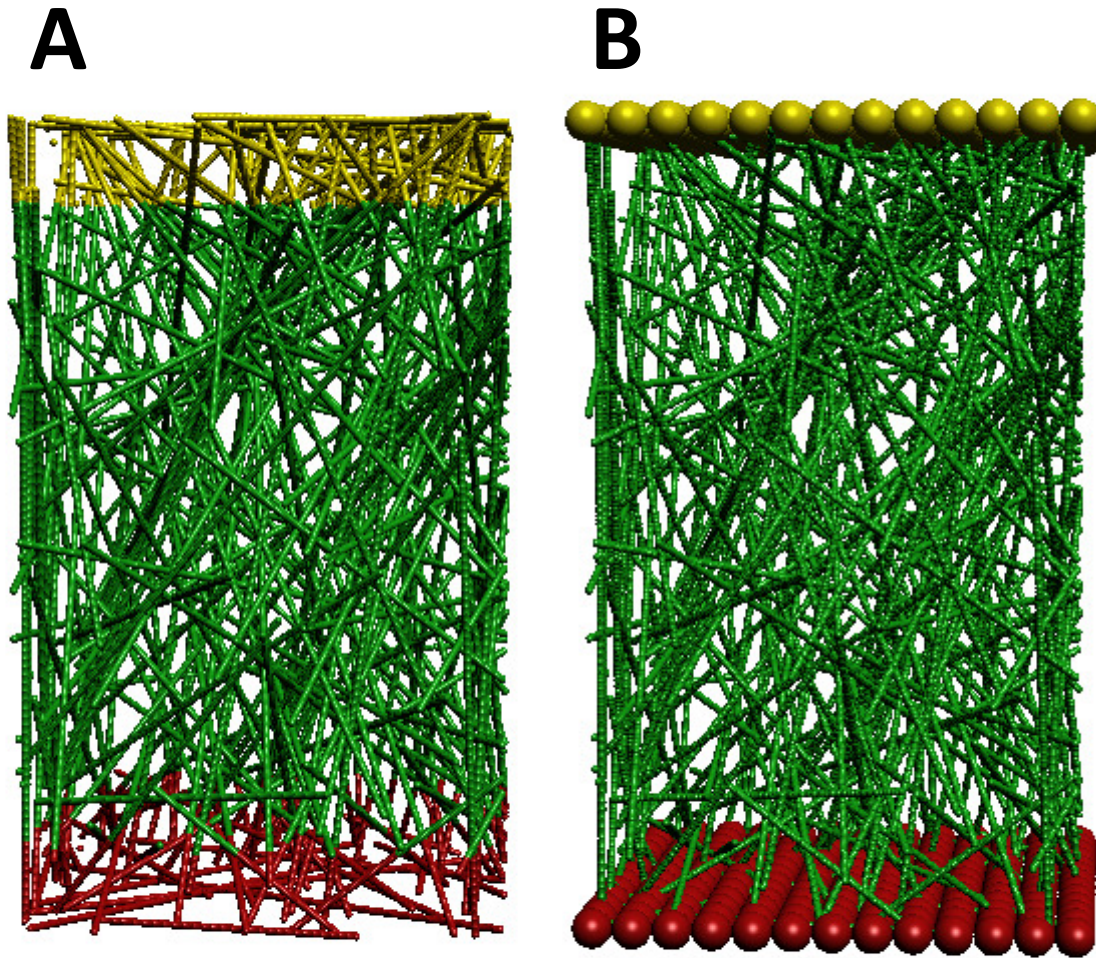
Figure 25: Schematic of the fibrin network with two variations of wall particle inclusion. In A, two layers of intra-network fibrin particles are designated as the walls. In B, two layers of additional non-fibrin particles are incorporated to act as the walls. In both wall inclusion scenarios, the top wall particles are colored yellow, the bottom wall particles are colored red, and the non-wall fibrin particles are green. Yellow particles are assigned a velocity in the positive y-direction (up) and red particles remain stationary to ground the aggregate during the stretching simulations. For the simulations executed within this work, the wall inclusion scenario from A was implemented.

0.2 µm **0.4 µm** **0.8 µm** **2.0 µm**
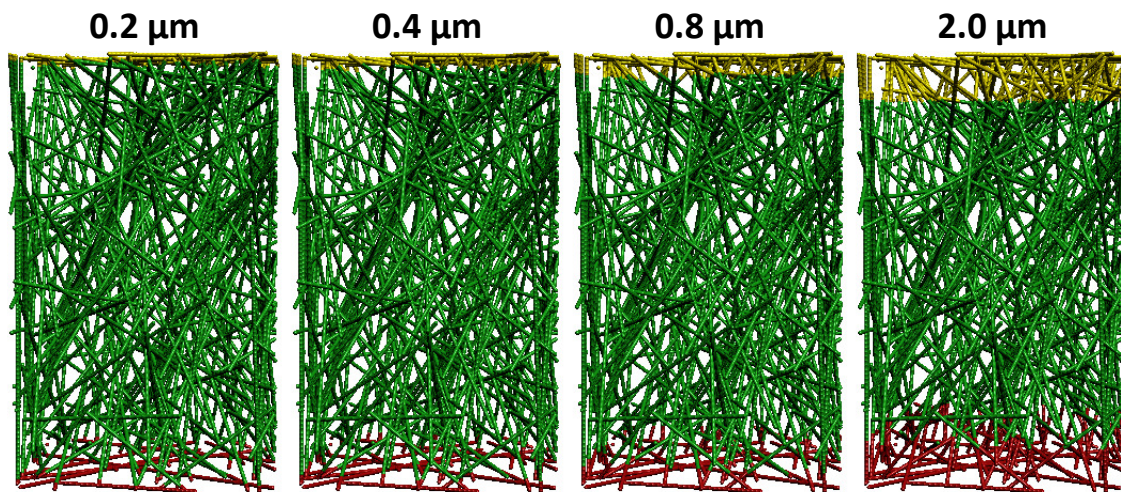
Figure 26: Schematic of the initial condition of the fibrin network with four different wall thicknesses increasing (from left to right) from 0.2 μm to 2.0 μm, where particles composing the bottom wall are colored red, particles composing the top wall are colored yellow, and non-wall fibrin particles are colored green. Moving from left to right, the thickness of the walls correspond to 1x, 2x, 4x, and 10x the diameter of the *in silico* fibrin strands.
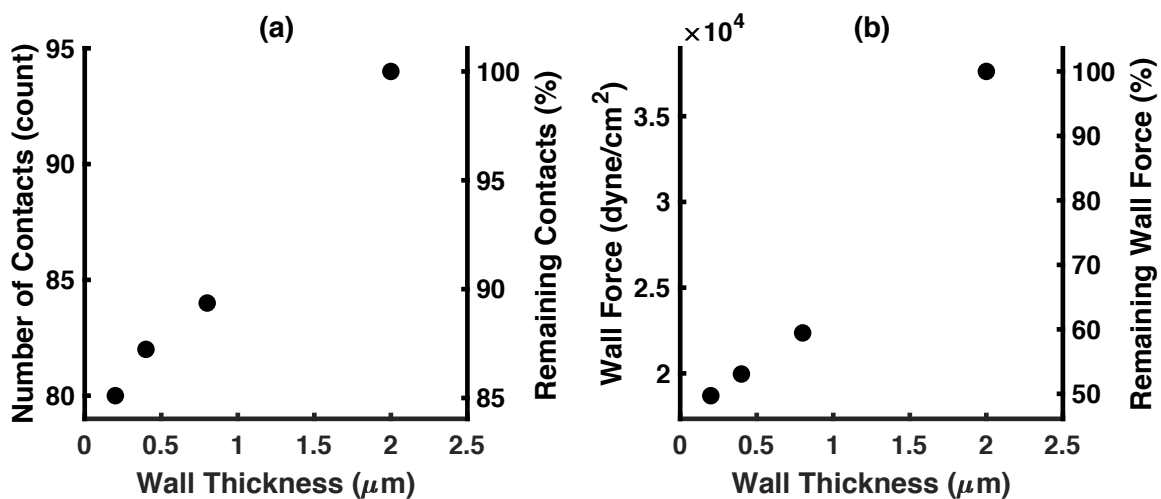
Figure 27: Number of contacts vs wall thickness (left) and wall force vs wall thickness (right) for four fibrin aggregate wall thickness scenarios, including 0.2, 0.4, 0.8, and 2.0 μm that correspond to the schematics of the fibrin aggregates depicted in Figure 26. Measurements were recorded when the top wall displacement reached 4 μm, corresponding to the maximum point of extension. The secondary y-axis for both of the plots shows the normalized ratio with respect to the value at 2.0 μm.

Table 7: Number of platelet particles included in the *in silico* aggregates shown in Figure 28 for various platelet concentrations within a 5.6e3 μm^3 simulation framework. Platelet particles were assumed to be spherical with a diameter of 2 μm.

Volume %	0.8	8	16	32
Platelets (count)	6	55	110	220

4. The platelet activation level was tuned to simulate the effect of varied activation and adhesive capacity on aggregate strength or resistance to stretching. The activation level was incorporated as a discrete parameter to discriminate between non-/weakly-, partially-, and fully-activated states. The three levels correspond to those observed experimentally in [77] that were used to calibrate the platelet-platelet adhesive interactions in Chapter 2. The platelet activation level was uniform across all platelets within a given run and held constant throughout the duration of each simulation. The number of platelet particles included for each of the four simulated concentration scenarios are listed in Table 7. The platelet counts were calculated to satisfy the appropriate volume fraction by assuming platelets to be spherical with a 2 μm diameter and the simulation framework to have a volume of 5.6e3 μm^3. Schematics of the initial platelet and fibrin particle positions for the five platelet concentration scenarios are included as Figure 28. Simulations were performed in triplicate for each combination of activation level and platelet concentration condition and a single execution of the fibrin only control, amounting to a total of 37 unique runs.

5.3 Results and Discussion of Aggregate Stretching Simulations

5.3.1 Effect of Varied Platelet Concentration

The force resisting the vertical displacement of the top wall (yellow particles) of the platelet and fibrin aggregates shown in Figure 28 was tracked as a function of the distance
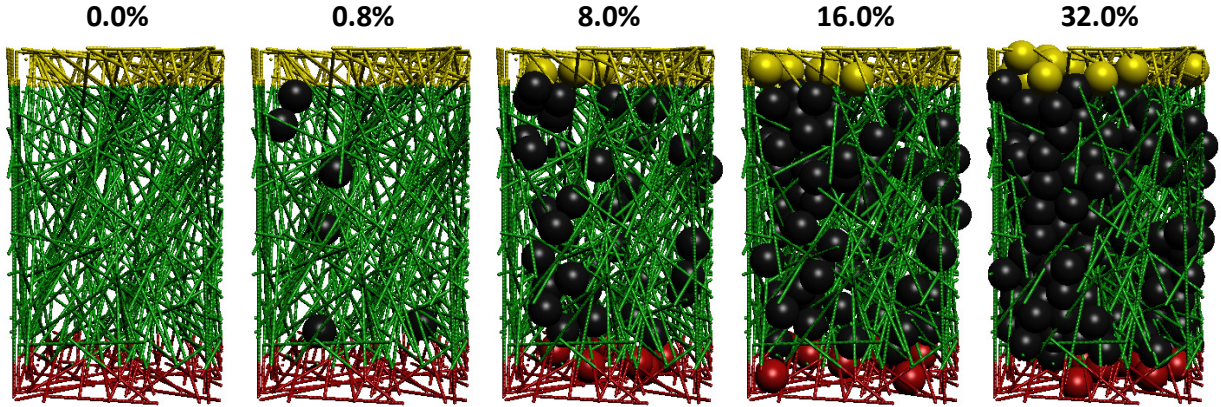
Figure 28: The initial conditions of the aggregates with 0-32% solid platelets (black particles) by volume and 3% solid fibrin (green particles) by volume. The wall layers are colored in yellow (top) and red (bottom) and the fibrin network structure is consistent across the platelet concentration scenarios.

the aggregate was stretched. Schematics of the final condition of the aggregates after a displacement of 4 μm are included in Figure 29. The green portions of the fibrin strands, visible in Figure 29, exhibit bends and curves, demonstrating the successful implementation of flexible and mobile fibrin strands. The emergent fibrin network rearrangement upon stretching is variable and depends on the platelet concentration and platelet positions within the aggregates. In the absence of platelets, the fibrin networks tend to rearrange first at the cross-linked sites, shown in Figure 22B, and the subsequent particle rearranging occurs in worm-like fashion as the perturbations travel along isolated fibrin strands and eventually throughout the fibrin network. Without any platelets present and in the low platelet concentration regime (0.8% platelets), the connectivity within the aggregates is not expected to be complete, meaning that some fibrin strands, especially ones oriented parallel to the simulation faces, are not connected to the rest of the aggregate and do not rearrange during the simulation.

When platelets are present within the aggregates, the platelets attract nearby fibrin strands and the network effectively collapses around the platelets to form tighter networks.
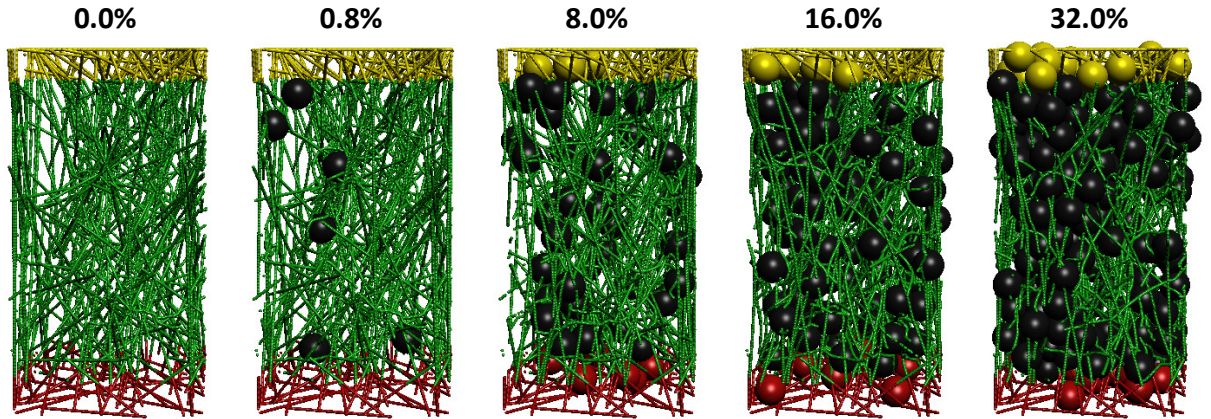
Figure 29: The final conditions of the aggregates from Figure 28 with 0-32% solid platelets (black particles) by volume and 3% solid fibrin (green particles) by volume after a 4 μm vertical displacement of the top wall. The wall layers are colored in yellow (top) and red (bottom) and the fibrin network structure is consistent across the platelet concentration scenarios.

This effect can be observed qualitatively in the three highest platelet concentration regimes, specifically 8-32% platelets, where the aggregates display a slight hour glass shape after a 4-μm stretch as seen in the three right-most schematics of Figure 29. The qualitative simulation results are supported by the physiological role of platelets in coagulation; platelets contribute to overall clot strength by binding and tightening nearby fibrin fibers via their strong contraction and adhesive forces [56].

The dynamics of the resistance stress on the ascending aggregate wall are reported in Figure 30 as a function of displacement in μm for the mean of three trials with the corresponding 95% confidence interval about the mean for platelet concentrations ranging from 0-32%. A new random initial condition of platelet positions was generated for each trial while maintaining the same fibrin network and the platelet activation level was controlled as fully-activated. The plot shows that the magnitude of the force that resists the stretching of the aggregates generally increases as function of the top wall displacement or the extent of stretching. The magnitude of the resistance stress also increases as a function of the platelet concentration.

As the platelet concentration increases, the inclusion of more platelets increases the number of possible platelet-platelet and platelet-fibrin adhesive interactions, thereby increasing the aggregate strength or the force required to stretch the aggregate. The complete separation of the 95% confidence interval bands from 0.8 to 32% indicates that the resistance stress mechanics are highly sensitive to platelet concentration. The exception to this is the 0% platelets or the fibrin-only scenario and the 0.8% platelets, whose curves overlap slightly along the 4-μm trajectory. Those overlapped wall-force curves result because the 0.8% platelet scenario is not dense enough with respect to the platelets to result in any platelet-platelet interactions, hence not enhancing the connectivity throughout the aggregate to distinguish the dynamics from the fibrin-only scenario.

The large initial decrease in the resistance stress is likely due to high local strain that is imposed on the wall-aggregate interface when the wall first begins to move, which is then relaxed as the force creeps through the rest of the aggregate network. The tracked force in Figure 30 is the sum of all platelet-fibrin and intra-strand fibrin-fibrin interaction forces in the positive y-direction (up). Aligned with Figure 29, these interactions include yellow fibrin particles with black platelet particles (platelet-fibrin) and yellow fibrin particles with green fibrin particles (intra-strand fibrin-fibrin). Yellow fibrin particles with either black platelets or green fibrin were excluded from the wall force calculation because their misaligned position from the yellow-green interface and forced velocity imposed an aphysiological condition on the yellow platelets and caused an erroneous contribution to the wall-force metric.
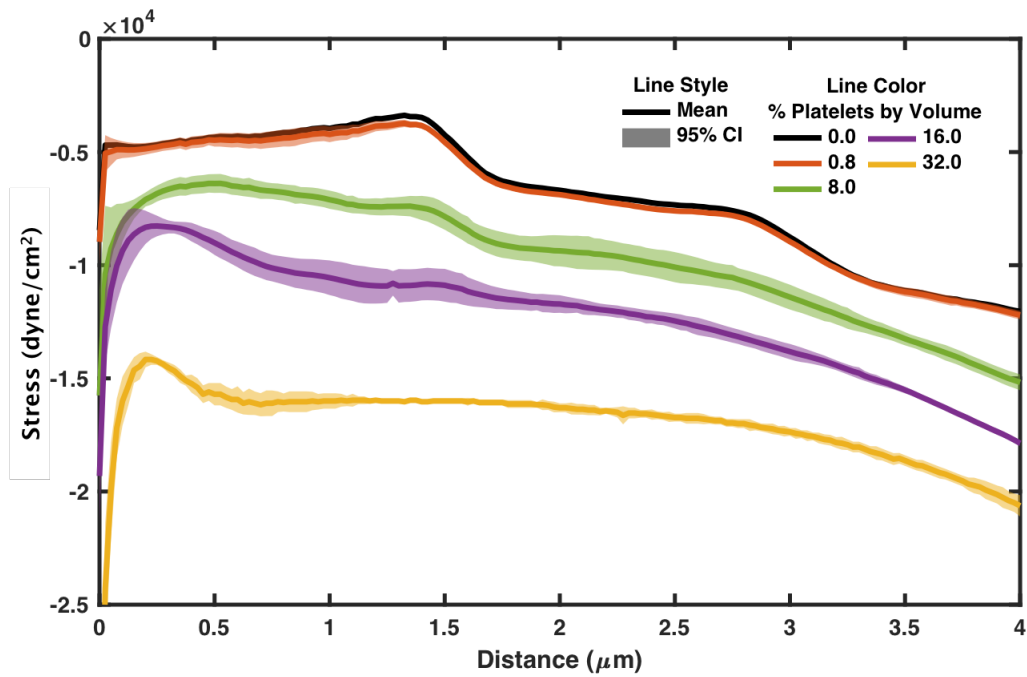
Figure 30: Mechanics of resistance stress in $dyne/cm^2$ on top wall of simulated platelet and fibrin aggregates as a function of displacement in μm. The mean of three trials with a shaded 95% confidence interval band are plotted for the fully-activated platelet condition of platelet concentrations ranging from 0-32% solid by volume and 3% solid fibrin. Schematics in Figures 28 and 29 correspond to displacements of 0 and 4 μm, respectively.

5.3.2 Effect of Platelet Activation Level

As a means to investigate the effect of platelet activation level on aggregate strength, we varied the platelet activation level from non-weakly-activated, partially-activated, and fully-activated as explained in Chapter 2 for the platelet-platelet adhesive interactions. For each subplot of Figure 31, the dynamics of the resistance stress on the ascending aggregate wall are reported as a function of displacement in μm for the mean of three trials with the corresponding 95% confidence interval about the mean for each of the three activation levels. The title of each subplot from Figure 31 corresponds to the platelet concentration of the aggregates.

Within each subplot, the curves corresponding to the three levels of activation are nearly indistinguishable, indicating that the resistance stress mechanics within the *in silico* aggregates are insensitive to platelet activation or platelet function. Mechanistically, this can be explained by the magnitude of the adhesive forces between the platelet-fibrin interactions and the platelet-platelet interactions. Platelet-fibrin adhesive interactions are nearly thirty times stronger than the strongest platelet-platelet interactions [56, 77]. The magnitude of the platelet-fibrin interactions was not adjusted with the platelet activation level as it likely would be in vivo or *in vitro*. However, regardless of changes in the strength of the platelet-platelet adhesive interactions as the activation level varies from fully-activated to partially-activated to non-weakly-activated, the platelet-fibrin interactions remain dominant and govern the overall resistance stress magnitude and dynamics.

Platelet function or activation level affects the degree of platelet aggregation and fibrin accumulation [77]. Both physiological changes alter the formation phase of the platelet and fibrin aggregates, which are steps in the coagulation cascade that occur prior to the stage of coagulation where this model is relevant. The simulation results demonstrate that after platelets form aggregates within a fibrin network, the degree of platelet activation or the platelet functionality has no effect on the overall strength of the aggregate.
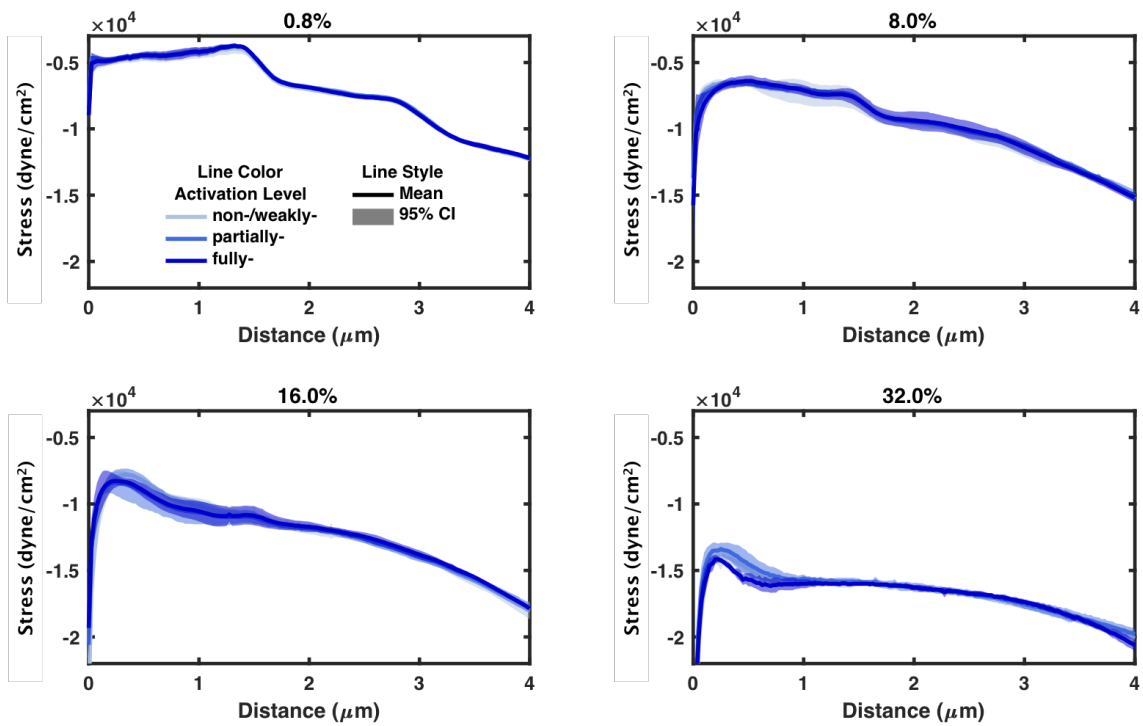
Figure 31: Mechanics of resistance stress in $dyne/cm^2$ on top wall of simulated platelet and fibrin aggregates as a function of displacement in μm. The mean of three trials with a shaded 95% confidence interval band are plotted for three platelet activation scenarios including non-/weakly-activated, partially-activated, and fully-activated within each subplot that is titled with the platelet concentration in solid volume percent, ranging from 0.8-32%.

5.3.3   Quantifying Platelet Contribution

The curves from the aggregate extension simulations with nonzero platelet concentrations from Chapter 5.3.1 and 5.3.2 can be normalized with respect to the fibrin-only case to generate a metric that is comparable to the clinical measurement known as the platelet contribution or the platelet component of clot strength. By subtracting the output of the *in silico* aggregate extension studies from the fibrin-only scenario from the output with platelets, the effect of platelets can be isolated.

In the clinic, the platelet component of clot strength is calculated by comparing TEG tracings before and after the application of glycoprotein IIb/IIIa receptor antagonist, which inhibits platelet adhesion [90]. In the presence of the platelet inhibitor, the magnitude of the pin amplitude from a TEG run is smaller, so the envelope of the pin tracing, or the TEG output, lies beneath the envelope of the pin tracing from the uninhibited platelet scenario. The area between the curves, or the difference in the TEG tracings before and after the application of the platelet inhibitor is equated to the platelet component of clot strength, which is then used to guide the transfusion of platelets in the treatment of coagulopathies [98].

Similarly, the area between the output curves from simulated aggregate extension studies with and without platelets can be calculated using Equation 5.7. The area between curves is the difference in the area under the curves.

$$\text{platelet contribution} = \frac{\text{AUC}_{\text{platelets + fibrin}} - \text{AUC}_{\text{fibrin}}}{\text{AUC}_{\text{platelets + fibrin}}} \times 100\% \qquad (5.7)$$

The *in silico* platelet contribution can be depicted schematically as the highlighted region of Figure 32, which corresponds to the difference in the AUC from the *platelet + fibrin* aggregate extension curve and the AUC from the *fibrin-only* aggregate extension curve. Equation 5.7 was used to generate the platelet contribution of all of the simulated aggregates from Chapter 5.3.1 and 5.3.2, where the *fibrin-only* curve was constant, but the *platelets + fibrin* curve varied based upon the simulation conditions.

In Figure 33, the results of the platelet contribution calculation are plotted as a function of the platelet concentration for 36 *in silico* aggregate extension simulations. Each of
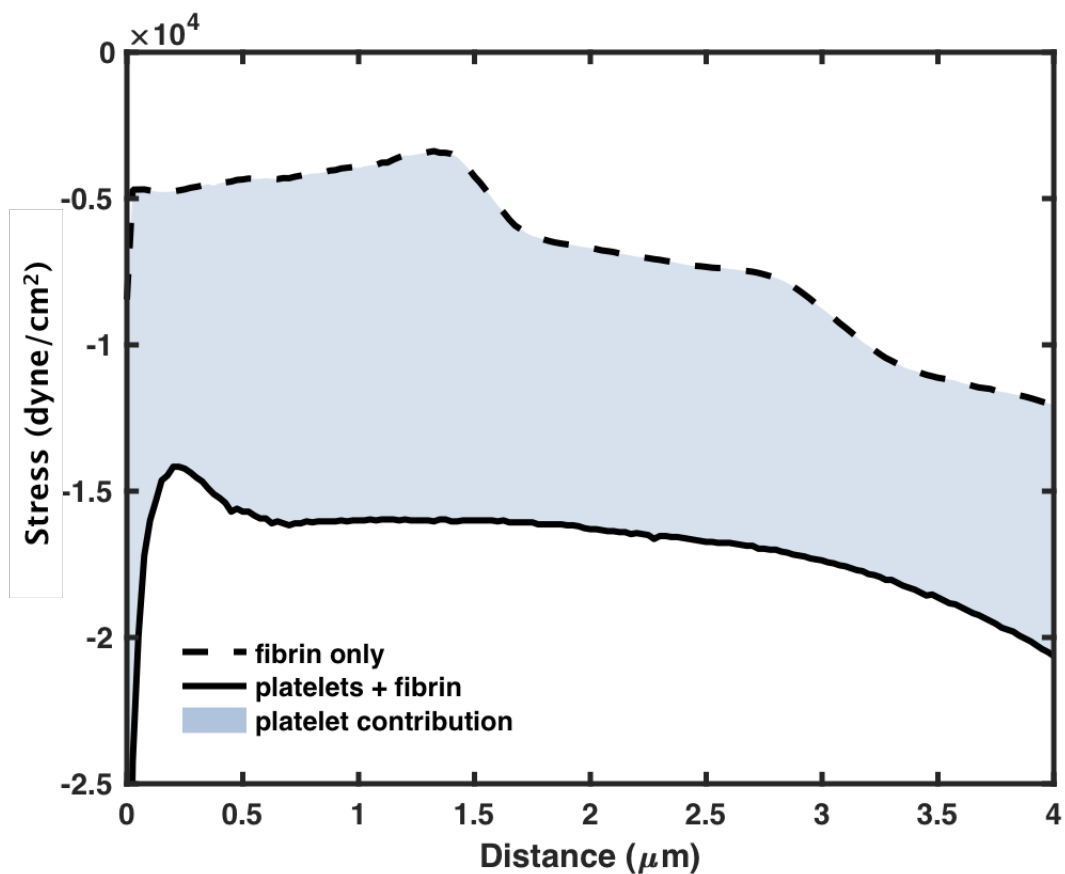
Figure 32: Visualization of the platelet contribution to aggregate strength highlighted as the area between fibrin-only and fibrin + platelets curves, corresponding to Equation 5.7. This particular fibrin + platelet scenario corresponds to a 32% solid platelets by volume, but the area between curves can be calculated across all simulated platelet concentrations and platelet activation scenarios.

the explored platelet concentration and platelet activation level scenarios was performed in triplicate. The AUCs from each simulation were calculated using the *trapz* function in MAT-LAB. The mean platelet contribution (%) are reported with corresponding 95% confidence intervals. As expected from the results reported in Chapters 5.3.1 and 5.3.2, the platelet contribution is highly sensitive to the platelet concentration, but insensitive to the platelet activation status.

According to Harr et al., the component contributions of platelets and fibrin to the clot strength are estimated to be 80% and 20%, respectively, for normal hemostasis [39]. The ratio of the component contributions can be calculated from the clot elasticity or the clot amplitude TEG output metric. Dependent upon the contribution method, the ratio varies nonlinearly with respect to the platelet count because clot elasticity and strength do not have a linear relationship [90]. Although the methodology for measuring platelet contribution to clot strength is somewhat debated, the general 80%/20% rule tends to apply, however, careful attention must be paid when using the platelet component for transfusion guidance [98].

The results from the *in silico* platelet and fibrin aggregate extension scenarios, reported in Figure 33, produced platelet contributions beneath the 80% threshold for normal platelet component, meaning that all of the explored *in silico* scenarios align with a thrombocytopenia diagnosis, or low platelet count pathology. Even though the quiescent platelet volume is less than one percent of blood, the local platelet concentration after platelet activation and aggregation is much higher [102]. The 32% solid platelets by volume was the upper bound of feasible *in silico* platelet concentrations due to the assumed rigid spherical structure and the manner in which the initial condition was generated; By establishing the fibrin network prior to placing the platelets within the simulation framework, the number of possible platelet particle positions are restricted due to the steric hindrance that the fibrin network imposes. However, despite not fully capturing the breadth of physiological platelet concentrations, the model developed herein successfully captures the sensitivity of platelet contribution to aggregate strength with respect to the platelet concentration.

The insensitivity of platelet contribution with respect to the platelet activation level or platelet function observed from the *in silico* aggregate extension studies corroborates with *in vitro* studies [90]. Platelet function and platelet count are known to be highly coupled, so it
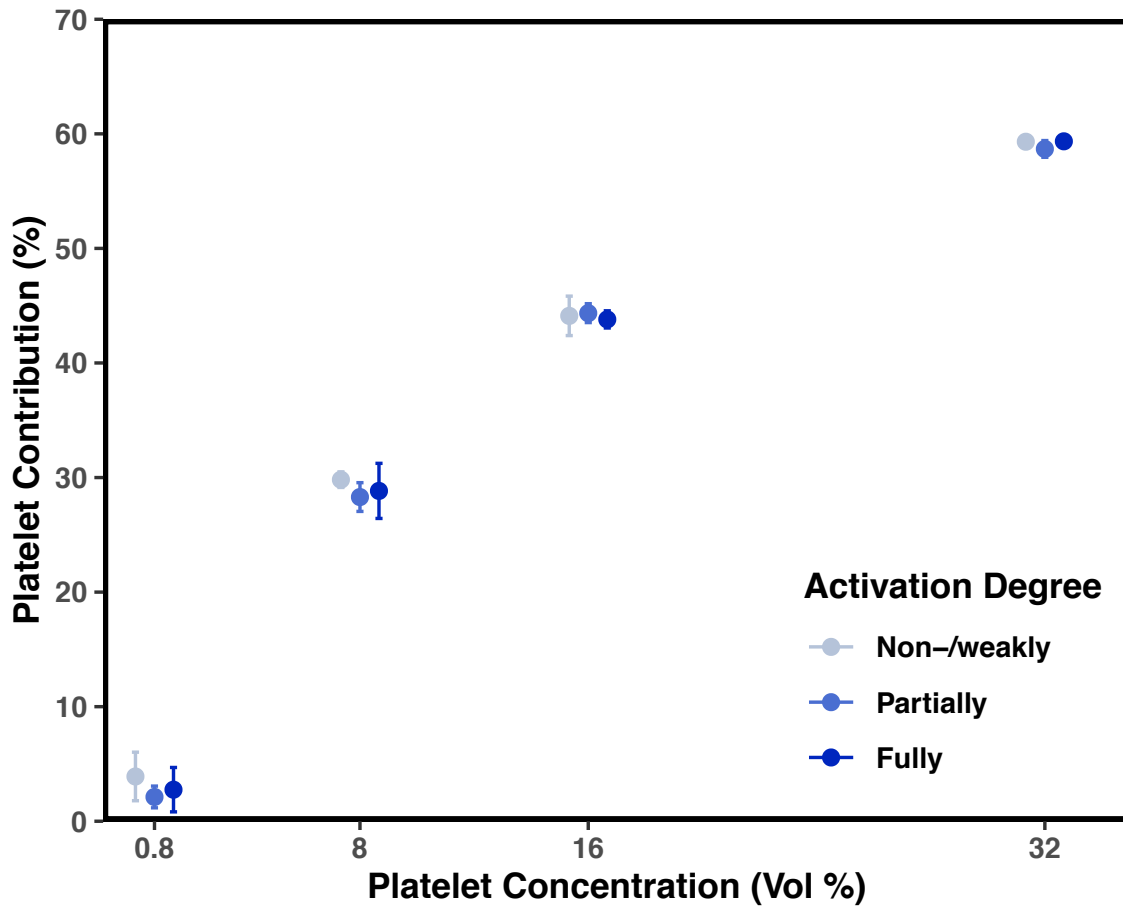
Figure 33: The mean platelet contribution to aggregate strength of three trials and corresponding 95% confidence intervals about the mean plotted as a function of platelet concentration ranging from 0.8-32% solid by volume for three platelet activation scenarios, including non-weakly-activated, partially-activated, and fully-activated.

is challenging both experimentally and computationally to isolate the two. *In vivo*, platelet function influences all stages of the coagulation cascade, including the degree of platelet aggregation and fibrin accumulation, which occurs upstream from the scope of the scenarios modeled herein [77]. By focusing on the stage of coagulation after fibrin accumulation and platelet aggregation, alterations in the platelet functionality may not manifest *in silico* to the extent that they might *in vivo*.

5.4   Summary

Through the development of a DEM-based model of platelet and fibrin aggregate dynamics, we have investigated the influence of platelet concentration and platelet activation level on the contribution of platelets to the strength of *in silico* aggregates. By first expanding the *in silico* platelet aggregation model from Chapter 4 to include flexible and mobile fibrin strands, the model developed herein can be used to simulate platelet and fibrin aggregate extension scenarios. By grounding the platelet and fibrin adhesive mechanics and fibrin strand extension mechanics in isolated experimental results from the literature, we have a calibrated model appropriate for scaling-up our simulations to capture the dynamics of platelet and fibrin aggregates.

The scale-up method for translating fibrin strands from rigid lines to chains of adjacent particles connected by implicit springs in series was developed in a general manner that can accommodate changes in fibrin strand length and individual fibrin particle sizes. The crosslinking capacity of fibrin networks was also incorporated into the model development through the design of an algorithm that considers the points of intersecting strands and effectively fuses overlapping particles through a remove-replace-reconnect sequence explained in Chapter 5.2.1. Fusing the intersecting fibrin particles captures the fibrin network connectivity, which enables the network extension simulations to exhibit the emergent behavior of fibrin assemblies.

The influence of platelet concentration, in the range of 0.8-32% solid platelets by volume, on the overall aggregate strength can be studied by modifying the number of platelet particles

included in the simulation framework. The *in silico* aggregate extension studies show that increasing the platelet concentration also increases the strength of the aggregates, which was measured by tracking the force that resisted a uni-axial stretching motion. The platelet activation level was also modified with the *in silico* aggregates, but no significant effect was observed on the resulting aggregate strength with respect to the activation level changes. We calculated the platelet contribution to the strength of the aggregates by comparing the force versus distance curves for each platelet concentration and activation level scenario combination to the force versus distance curve of the lone fibrin network. The resulting range of platelet contribution values falls beneath hemostatic thresholds, identifying that the simulated range of platelet concentrations correspond to a thrombocytopenia pathology. Despite the small breadth of simulated platelet concentrations due to the assumed platelet sphericity, the model can still capture the effect of platelet concentration on the platelet contribution to aggregate strength that is observed clinically.

The model developed herein combined an independent platelet and fibrin adhesive mechanics model with another independent model of extensible fibrin to yield a model with the capacity to model platelet and fibrin aggregate dynamics. The resulting model is grounded in experimental isolated platelet adhesion studies and fibrin extension studies that serve to calibrate the independent contributions. Together, this model as a whole provides insight into the mechanism of platelet and fibrin aggregate dynamics. Furthermore, the resulting model bridges the gap to the macroscale by approximating comparable metrics, like the platelet contribution to clot strength, to those obtained from whole-blood assays.

6.0 Summary and Outlook

6.1 Model Utility

6.1.1 Platelet Adhesive Mechanics

In Chapter 2, a DEM-based platelet adhesive mechanics model was developed that captures the phenomenological behavior of platelet-platelet and platelet-fibrin adhesion. The cell-scale model serves as the foundation for the development of a multiscale model of coagulation by including the micro-mechanical contributions that influence downstream clot formation. The platelet adhesion model is suitable to simulate the collective and emergent behavior of platelet and fibrin interactions.

Within the platelet adhesive mechanics model, the platelet activation level is modifiable to accommodate four levels that govern platelet-platelet interactions. The levels range from inactive (no adhesion) to fully-active (strongest adhesion). Both platelet-platelet and platelet-fibrin adhesion is incorporated via implicit springs that are mathematically defined as piecewise linear functions. The piecewise linear functions that describe the adhesive interactions were calibrated to experimental data from the literature [77, 56]. With the aim of utilizing the developed cell-scale model as the foundation of a larger, multiscale model, the phenomenological nature of the model provides the computational feasibility required for scale-up.

6.1.2 Fibrin Extensibility Mechanics

In Chapter 3, the unique mechanical properties of fibrin were modeled *in silico* by simulating fibrin strands as chains of small particles linked together with implicit springs. The springs behave according to Hooke's Law with a variable spring coefficient that is mapped to experimental data. The isolated fibrin strand *in silico* model captures the high extensibility, strain-hardening, and viscoelastic behavior of *in vitro* fibrin.

We calibrated the implicit spring force between neighboring particles of the same strand to extension-retraction data from *in vitro* fibrin studies [63]. The mechanical properties can be measured from stress-strain curves obtained by applying a stress, or a force per unit area, and recording the resulting strain, or the stretch normalized to its initial length [123]. The model from this chapter functions not only as a stand-alone entity, but also as a building block for a multiscale model that includes fibrin networks composed of hundreds to thousands of strands.

6.1.3   Platelet and Fibrin Aggregate Mechanics

In Chapter 4, a DEM-based model of platelet aggregation was developed by scaling-up the platelet adhesive mechanics model from Chapter 2 to include hundreds of activated platelets. It was used to investigate the influence of platelet concentration and fibrin inclusion on the emergent collective behavior and subsequent clot morphologies. We manipulated the method of fibrin incorporation in our model to simulate two pathological scenarios. We handled fibrin implicitly to identify the influence of extremely flexible and/or short fibrin bundles and explicitly to investigate the effect of inflexible and immobile fibrin.

We characterized the morphological differences of the emergent *in silico* platelet and fibrin plugs. We calculated the aggregate permeabilities by executing LBM simulations of fluid flow through the resulting aggregates. Despite the departure from experimental counterparts due to the assumed platelet sphericity, we identified the role that fibrin plays in the flow through the aggregates. The stiff and immobile implementation of *in silico* fibrin restricted the mobility of the platelets and also the pore size, thus limited the aggregate permeabilities. The results from the simulated fibrin scenarios created the bounds of expected platelet behavior during aggregation and enabled a comparison of aggregate formation as a function of fibrin structure and platelet concentration. This model as a whole provides insight into the mechanism of platelet aggregation and the potential effect of pathological fibrin on aggregate formation.

6.1.4 Platelet and Fibrin Aggregate Dynamics

In Chapter 5, the platelet and fibrin mechanical model was translated into a dynamic framework to investigate the influence of platelet concentration and platelet activation level on the contribution of platelets to the strength of *in silico* aggregates. By first expanding the *in silico* platelet aggregation model from Chapter 4 to include flexible and mobile fibrin strands, the resulting model can be used to simulate platelet and fibrin aggregate extension scenarios. By grounding the platelet and fibrin adhesive mechanics and fibrin strand extension mechanics in isolated experimental results from the literature, we calibrated the model components separately, prior to combining them to capture the dynamics of platelet and fibrin aggregates.

We used the static fibrin network model as the scaffold for converting the rigid fibrin cylinders to chains of adjacent particles connected by implicit springs in series. The known geometry of the scaffold framework facilitated the crosslinking algorithm development within the fibrin networks. The resulting crosslinked/fused particle locations provided the fibrin network connectivity, allowing the network extension simulations to exhibit the emergent behavior of fibrin assemblies.

The influence of platelet concentration on the overall aggregate strength was studied by modifying the number of platelet particles included in the simulation framework. We developed a method to calculate the platelet contribution to the strength of the aggregates by comparing the force versus distance curves for each platelet concentration and activation level scenario combination to the force versus distance curve of the lone fibrin network. The resulting model provides insight into the mechanism of platelet and fibrin aggregate dynamics and bridges the gap to the macroscale by approximating comparable metrics, like the platelet contribution to clot strength, to those obtained from whole-blood assays. By taking a bottom-up approach to the problem, the trans-scale relationships among the model components were elucidated through the emergent behavior of the combined models. The model functions as a general tool that can be expanded and used to predict the effects that changes in blood composition have on hemostasis.

The *in silico* aggregate extension studies performed herein were executed on a local server and each run required several weeks to generate the included results. Because the acceleration of the particles within these systems is possibly small, a quasi-static assumption could be considered, which is appropriate for modeling slow deformations of granular materials [110]. In the case of very dense materials, the quasi-static assumption means that the normal force calculations can be replaced with constants to drastically reduce the computational cost of the simulations. However, if the assembly is loose and the particle impacts cannot be ignored, the force terms must evolve according to classical DEM.

6.2   Future Work

The model that stands as the culmination of the work from this dissertation provides the foundation for a general model that can be tailored toward a specific application or expanded to include more functional detail. Including the influence of fluid blood plasma is a logical consideration that can be explored through coupled LBM-DEM simulations of platelet aggregation under flow. Results from studies of platelet aggregation under flow can be used to inform the initial conditions of the platelet and fibrin aggregate studies from Chapter 5, in place of the existing assumptions regarding initial platelet concentrations. It is known that platelet activation levels influence the rate and capacity of platelet aggregation and the ultimate packing density of platelet plugs *in vitro* [66]. The varied platelet activation model developed in Chapter 2 can be coupled with a model of platelet aggregation under flow as an avenue to explore this effect.

We can simulate platelet aggregation under a couette flow scenario to approach the inclusion of an additional plasma component and to study the effect of platelet activation level on aggregation. The model can be calibrated with a comparable experimental study that measured the contractile forces in platelet aggregates within a microfluidic device [104]. *In vitro*, the activation capacity of platelets was controlled by modifying the shear rate and the concentration of inhibitory agents. Ting et al. designed a microfluidic system that contained an array of fibrin-coated flow barriers that acted as the substrate for platelet aggregation. We

can simulate the microfluidic array by including a single flow barrier set and implementing periodic boundaries to execute repeated unit cells of the simulation framework. A schematic of the unit cell of the described microfluidic array is included in Figure 34.

We can vary the platelet concentration as well as the platelet activation level at the beginning of the LBM-DEM simulations and define a pressure drop across the x dimension to initiate a constant flow rate in the direction of the flow. A schematic of the initial condition with 40 platelets within the cross-sectional view is included as Figure 35. During the simulations, the frequency of platelet adhesion and the force due to platelet contraction can be tracked to investigate the sensitivity of those metrics to changes in the platelet count and platelet function. A schematic of the steady-state flow scheme is included as Figure 36 where the fluid flows from left to right. The capture radius of the activated *in silico* platelets can be tuned in order to fit the aggregation rate of the platelets to the data available in the literature [104].

A fibrin polymerization model could also be developed that generates the strands and networks that align with the model from Chapter 5. By incorporating fibrin polymerization, the expanded model will be equipped to simulate platelet and fibrin aggregate formation under flow. Such a model could be used to generate TEG tracings *in silico*. In modeling the TEG *in silico*, specific relationships between the blood coagulation participants and the measurable parameters of the TEG could be defined. A combined LBM-DEM *in silico* model of an entire TEG would be unrealistic to simulate due to the computational expense of calculating the interactions of the billions of blood cell particles across a time frame on the order of minutes. Instead, we could model a volume fraction of a to-scale TEG as a unit cell with periodic boundary conditions.

Through a dynamic *in silico* model of a TEG, the clot assembly and organization of the blood particles could be visualized in real-time, which is not possible with existing TEGs in the clinic. The organization of simulated clots could be paired with the TEG outputs to establish certain patterns that result in specific TEG shapes. By recreating TEG tracings and simulating various coagulopathic states, the model could also be used to explore and design more precise treatments. It is possible and not unlikely that by incorporating the mechanistic details into the cell-scale models, the computational framework could be used to identify
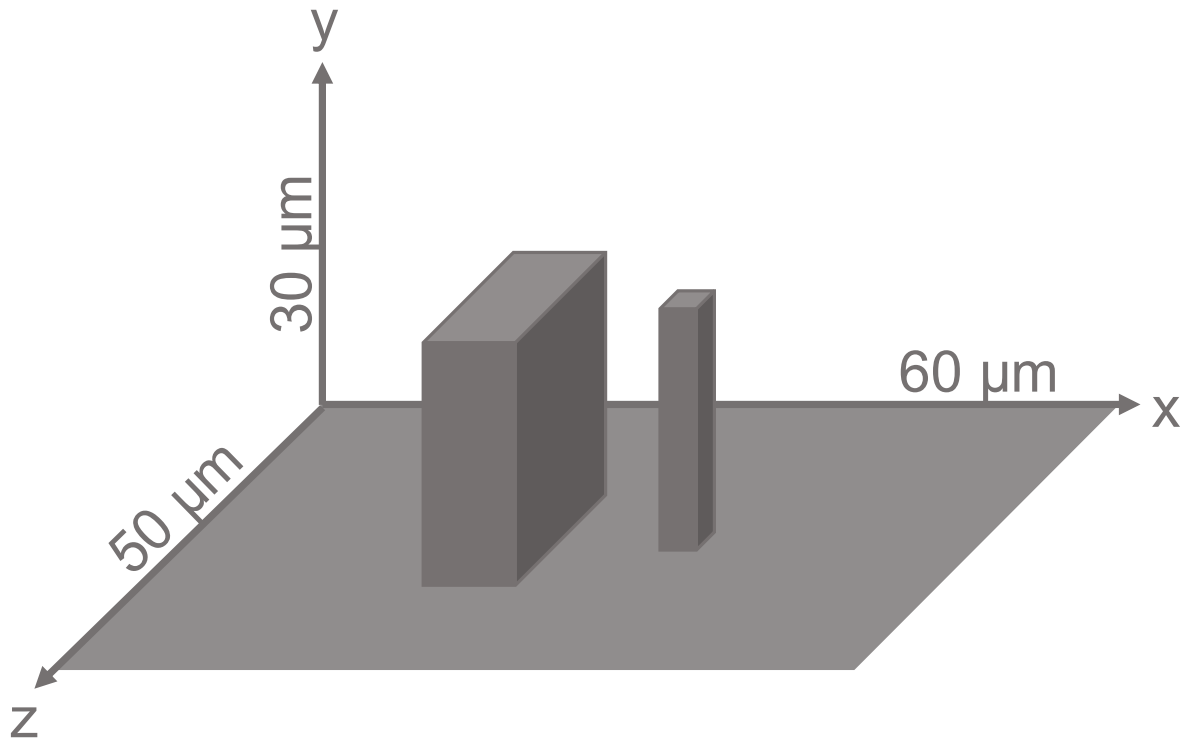
Figure 34: Schematic of a three-dimensional 60 μm x 30 μm x 50 μm unit cell of the LBM-DEM simulation framework with two solid, fibrin-coated flow barriers. Simulation boundary conditions are periodic in x and z and fluid flows in the x-direction.
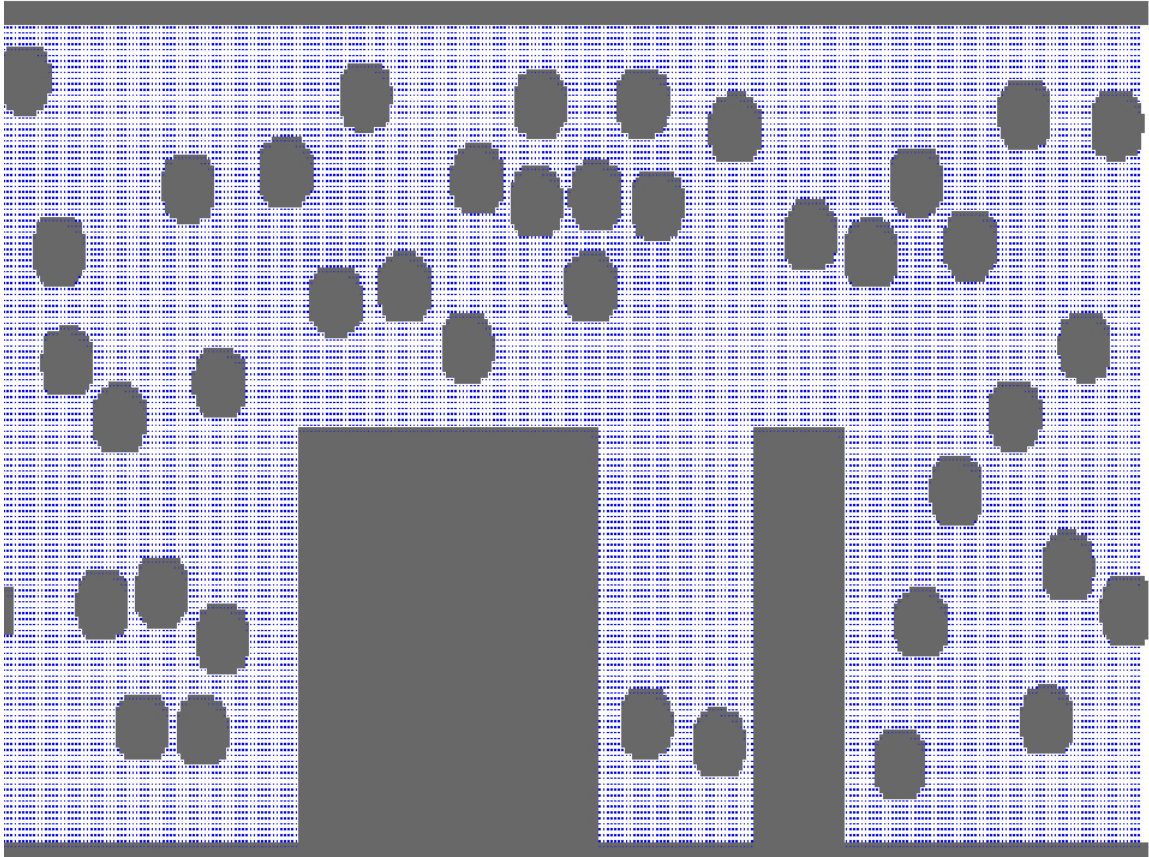
Figure 35: Cross-section of initial condition of a three-dimensional LBM-DEM simulation of the activation, aggregation, and adhesion of 40 platelets (in view) under flow with two solid, fibrin-coated boundary walls impeding the flow. Simulation boundary conditions are periodic in the x and z direction, and finite in y.
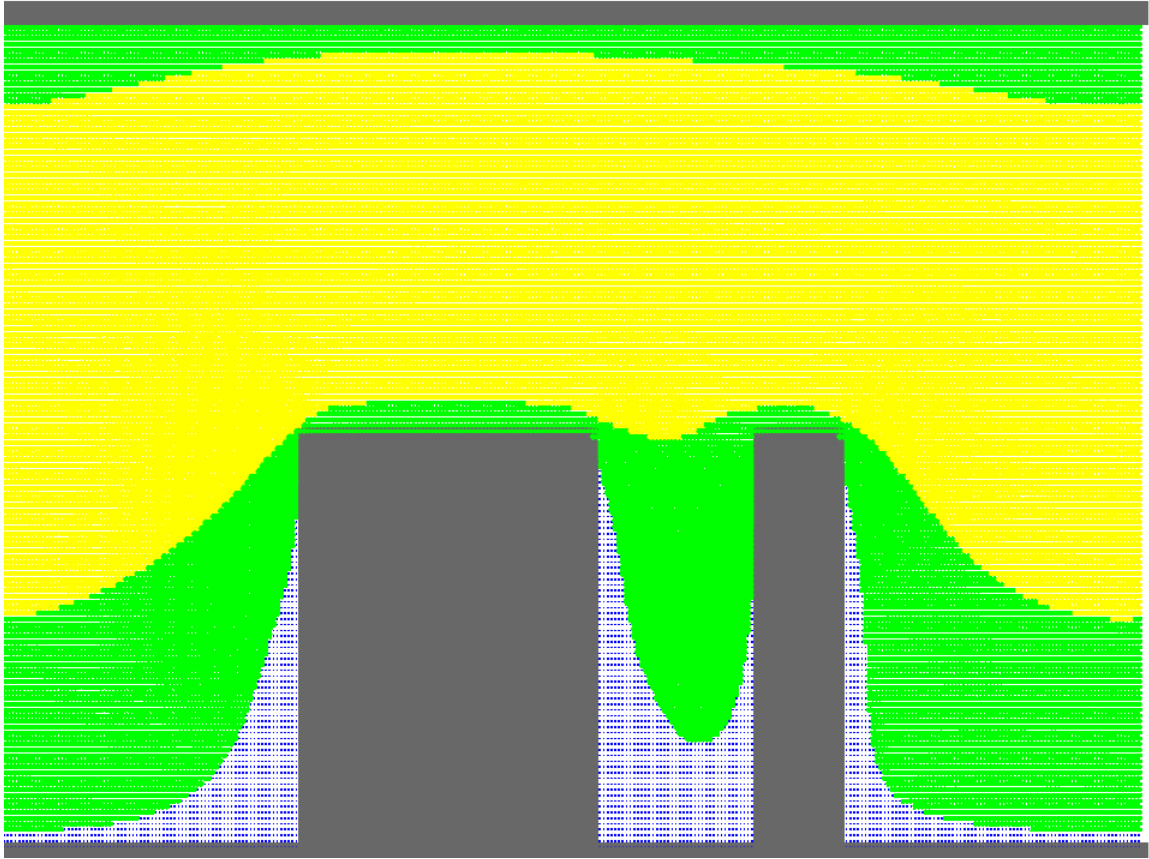
Figure 36: Cross-section of fluid steady-state of a three-dimensional LBM-DEM simulation of flow with two solid boundary walls impeding the flow. Simulation boundary conditions are periodic in the x and z direction, and finite in y.

several possible treatment designs. The model could then be used to determine patient responses to treatments *in silico*, prior to administration in the clinic, so the traditional heuristic cocktail of blood-product therapies given to patients with abnormal TEGs becomes extinct.

The mechanistic cell-scale models of fibrin and platelets can be easily modified so as to simulate coagulopathies. For instance, thrombocytopenia can be simulated by lowering the platelet concentration; hemophilia would result in non-/weakly activated platelets; and disfibrinogenemia, which is clinically defined as low fibrin functionality, can be simulated by a decreased fibrin concentration. If hundreds of TEG shapes could be reproduced by varying the initial blood composition as in Chapters 4 and 5, multiplicities in the readouts could be sought to develop blood composition probability distributions for each TEG shape. More precise treatments could be designed by observing the sensitivity of the blood composition on the TEG shapes in response to changes in particular concentrations. From the hundreds of simulated TEGs, subtle differences in TEG shapes could also be able to identified that would indicate a strong benefit from a specific therapy. The model could be used to simulate enough TEGs with corresponding treatment trajectories to establish a database-type reference for clinicians to use to inform treatment times and dosage regimens for patients with coagulopathies as a means to improve their outcomes by moving the patient into an acceptable clotting performance range.

Bibliography

[1] George L Adams, Roberto J Manson, Immanuel Turner, David Sindram, and Jeffrey H Lawson. The balance of thrombosis and hemorrhage in surgery. *Hematol Oncol Clin North Am*, 21(1):13–24, feb 2007.

[2] Cyrus K Aidun and Jonathan R Clausen. Lattice-Boltzmann Method for Complex Flows. *Annual Review of Fluid Mechanics*, 42(1):439–472, 2010.

[3] Cyrus K. Aidun and Jonathan R. Clausen. Lattice-Boltzmann Method for Complex Flows. *Annual Review of Fluid Mechanics*, 42(1):439–472, 2010.

[4] T. AlMomani, H. S. Udaykumar, J. S. Marshall, and K. B. Chandran. Micro-scale dynamic simulation of erythrocyte-platelet interaction in blood flow. *Annals of Biomedical Engineering*, 36(6):905–920, 2008.

[5] Y Bazilevs, M Hsu, J Kiendl, R Wüchner, and K Bletzinger. 3D Simulation of Wind Turbine Rotors at Full Scale. Part II: Fluid Structure Interaction Modeling with Composite Blades. *International Journal for Numerical Methods in Fluids*, 65(October 2010):236–253, 2011.

[6] A.V. Belyaev and V. Volpert. Modeling thrombosis in silico: Frontiers, challenges, unresolved problems and milestones. *Physics of Life Reviews*, pages 42–44, 2018.

[7] PL Bhatnagar, EP Gross, and M Krook. A model for collision processes in gases. I. Small amplitude processes in charged and neutral one-component systems. *Physical review*, 94(3):511–525, 1954.

[8] T. Bodnár and a. Sequeira. Numerical Simulation of the Coagulation Dynamics of Blood. *Computational and Mathematical Methods in Medicine*, 9(2):83–104, 2008.

[9] Daniel Bolliger, Manfred D. Seeberger, and Kenichi A. Tanaka. Principles and Practice of Thromboelastography in Clinical Coagulation Management and Transfusion Practice. *Transfusion Medicine Reviews*, 26(1):1–13, 2012.

[10] F Cairnduff, M Stringer, E Hudson, D Ash, and S Brown. Superficial photodynamic therapy with topical 5-aminolaevulinic acid for superficial primary and secondary skin cancer. *Br. J. Cancer*, 69:605–608, 1994.

[11] B. S. Camas. Lattice Boltzmann Modeling for Mass Transport Equations in Porous Media. 2002(December), 2008.

[12] K C Chang, D F Tees, and D a Hammer. The state diagram for cell adhesion under flow: leukocyte rolling and firm adhesion. *Proceedings of the National Academy of Sciences of the United States of America*, 97(21):11262–11267, 2000.

[13] Jennifer K W Chesnutt and Hai-Chao Han. Platelet size and density affect shear-induced thrombus formation in tortuous arterioles. *Physical biology*, 10(5):056003, 2013.

[14] Bastien Chopard, Jean L. Falcone, and Jonas Latt. The lattice Boltzmann advection-diffusion model revisited. *European Physical Journal: Special Topics*, 171(1):245–249, 2009.

[15] Jordan C. Ciciliano, Reginald Tran, Yumiko Sakurai, and Wilbur A. Lam. The platelet and the biophysical microenvironment: Lessons from cellular mechanics. *Thrombosis Research*, 133(4):532–537, 2014.

[16] Douglas B. Cines, Tatiana Lebedeva, Chandrasekaran Nagaswami, Vincent Hayes, Walter Massefski, Rustem I. Litvinov, Lubica Rauova, Thomas J. Lowery, and John W. Weisel. Clot contraction: Compression of erythrocytes into tightly packed polyhedra and redistribution of platelets and fibrin. *Blood*, 123(10):1596–1603, 2014.

[17] J P Collet, D Park, C Lesty, J Soria, C Soria, G Montalescot, and J W Weisel. Influence of fibrin network conformation and fibrin fiber diameter on fibrinolysis speed: dynamic and structural approaches by confocal microscopy. *Arteriosclerosis, thrombosis, and vascular biology*, 20(5):1354–1361, 2000.

[18] Jean-Philippe Collet, Henry Shuman, Robert E Ledger, Seungtaek Lee, and John W Weisel. The elasticity of an individual fibrin fiber in a clot. *Proceedings of the National Academy of Sciences of the United States of America*, 102(26):9133–7, 2005.

[19] B K Cook, D R Noble, and J R Williams. A direct simulation method for particle-fluid systems. *Engineering Computations*, 21(2-4):151–168, 2004.

[20] C.Thornton. Coefficient of Restitution for Collinear Collisions of Elastic-Perfectly Plastic Spheres. *Journal of applied mechanics.*, 64(2):383–386, 1997.

[21] P. A. Cundall. Cundall_Strack_1979. *Geeotechnique*, 29(29):47–65, 1979.

[22] Peter A Cundall. Construction of a LBM-DEM Coupling System and its Applications in Modeling Fluid Particle Interaction in Porous Media Flow. (May), 2012.

[23] Machado D., Costa R.S., Rocha M., Ferreira E.C., Tidor B., and Rocha I. Modeling formalisms in systems biology. *AMB Express*, 1(1):1–14, 2011.

[24] E W Davie, K Fujikawa, and W Kisiel. The coagulation cascade: initiation, maintenance, and regulation. *Biochemistry*, 30(43):10363–10370, 1991.

[25] N H Duong, E Shen, T Shinbrot, and F Muzzio. Segregation in granular materials and the direct measurement of surface forces using atomic force microscopy. *Powder Technology*, 145(1):69–72, jul 2004.

[26] Pep Español, Mariano Revenga, and Pep Espan. Smoothed dissipative particle dynamics. *Phys. Rev. E*, 67(2):26705, feb 2003.

[27] Brunhilde Felding-Habermann. Integrin adhesion receptors in tumor metastasis. *Clinical and Experimental Metastasis*, 20(3):203–213, 2003.

[28] Y Feng, K Han, and D Owen. Coupled lattice Boltzmann and discrete element modelling of particle transport in turbulent fluid flows: COmputational issues. *Proceedings of the 2011 American Control Conference*, (March):1885–1891, 2011.

[29] Aaron L Fogelson. Continuum Models of Platelet Aggregation : Formulation and Mechanical Properties. *Society for Industrial and Applied Mathematics*, 52(4):1089–1110, 1992.

[30] Aaron L. Fogelson and Keith B. Neeves. Fluid Mechanics of Blood Clot Formation. *Annual Review of Fluid Mechanics*, 47(1):377–403, 2015.

[31] Bryan R Fonslow, Benjamin D Stein, Kristofor J Webb, Tao Xu, Jeong Choi, Sung Kyu, and John R Yates Iii. NIH Public Access. 10(1):54–56, 2013.

[32] W. E. Fowler, R. R. Hantgan, J. Hermans, and H. P. Erickson. Structure of the fibrin protofibril. *Proceedings of the National Academy of Sciences of the United States of America*, 78(8 I):4872–4876, 1981.

[33] Jonathan B. Freund. Numerical Simulation of Flowing Blood Cells. *Annual Review of Fluid Mechanics*, 46(1):67–95, 2014.

[34] Bruce S. Gardiner, Kelvin K.L. Wong, Grand R. Joldes, Addison J. Rich, Chin Wee Tan, Antony W. Burgess, and David W. Smith. Discrete Element Framework for Modelling Extracellular Matrix, Deformable Cells and Subcellular Components. *PLoS Computational Biology*, 11(10):1–23, 2015.

[35] Tobias Geback and Alexei Heintz. A Lattice Boltzmann Method for the Advection-Diffusion Equation with Neumann Boundary Conditions. *Communications in Computational Physics*, 15(2):487–505, 2013.

[36] D. R. Golbert, P. J. Blanco, a. Clausse, and R. a. Feijóo. Tuning a lattice-Boltzmann model for applications in computational hemodynamics. *Medical Engineering and Physics*, 34(3):339–349, 2012.

[37] R Gray and F Baldwin. Targeting blood tests in the ICU may lead to a significant cost reduction. *Intensive Care Med*, 28, 2002.

[38] R D Groot and K L Rabone. Mesoscopic simulation of cell membrane damage, morphology change and rupture by nonionic surfactants. *Biophysical journal*, 81(2):725–36, aug 2001.

[39] Jeffrey N. Harr, Ernest E. Moore, Theresa L. Chin, Arsen Ghasabyan, Eduardo Gonzalez, Max V. Wohlauer, Anirban Banerjee, Christopher C. Silliman, and Angela Sauaia. Platelets are dominant contributors to hypercoagulability after injury. *Journal of Trauma and Acute Care Surgery*, 74(3):756–765, 2013.

[40] Xing He, Gary Duckwiler, and Daniel J. Valentino. Lattice Boltzmann simulation of cerebral artery hemodynamics. *Computers & Fluids*, 38(4):789–796, 2009.

[41] Maureane Hoffman. Remodeling the blood coagulation cascade. *Journal of Thrombosis and Thrombolysis*, 16(1-2):17–20, 2003.

[42] P Y Huang and J D Hellums. Aggregation and disaggregation kinetics of human blood platelets: Part I. Development and validation of a population balance method. *Biophysical journal*, 65(1):334–43, 1993.

[43] P Y Huang and J D Hellums. Aggregation and disaggregation kinetics of human blood platelets: Part III. The disaggregation under shear stress of platelet aggregates. *Biophysical journal*, 65(1):354–61, 1993.

[44] Nathan E. Hudson, John R. Houser, E. Timothy O'Brien, Russell M. Taylor, Richard Superfine, Susan T. Lord, and Michael R. Falvo. Stiffening of individual fibrin fibers equitably distributes strain and strengthens networks. *Biophysical Journal*, 98(8):1632–1640, 2010.

[45] Paul a Janmey and Christopher a McCulloch. Cell mechanics: integrating cell responses to mechanical stimuli. *Annual review of biomedical engineering*, 9:1–34, 2007.

[46] Chauying J. Jen and Larry V. McIntire. The structural properties and contractile force of a clot. *Cell Motility*, 2(5):445–455, 1982.

[47] K.L. Johnson. *Contact Mechanics*. Cambridge University Press, 1985.

[48] Oliver Jonas, Claudia T. Mierke, and Josef a. Käs. Invasive cancer cell lines exhibit biomechanical properties that are distinct from their noninvasive counterparts. *Soft Matter*, 7(24):11488, 2011.

[49] Seung Jae Joo. Mechanisms of platelet activation and integrin $\alpha II\beta 3$. *Korean Circulation Journal*, 42(5):295–301, 2012.

[50] Rimantas Kačianauskas, Robertas Balevičius, Darius Markauskas, and Algirdas Maknickas. Discrete Element Method in Simulation of Granular Materials. In *IUTAM Symposium on Multiscale Problems in Multibody System Contacts*, pages 65–74. 2007.

[51] Khaled Khairy, JiJinn Foo, and Jonathon Howard. Shapes of Red Blood Cells: Comparison of 3D Confocal Images with the Bilayer-Couple Model. *Cellular and Molecular Bioengineering*, 1(2-3):173–181, 2008.

[52] Oleg V. Kim, Rustem I. Litvinov, Mark S. Alber, and John W. Weisel. Quantitative structural mechanobiology of platelet-driven blood clot contraction. *Nature Communications*, 8(1):1–10, 2017.

[53] Oleg V. Kim, Rustem I. Litvinov, John W. Weisel, and Mark S. Alber. Structural basis for the nonlinear mechanics of fibrin networks under compression. *Biomaterials*, 35(25):6739–6749, 2014.

[54] Mika M. Kohonen, Dimitrios Geromichalos, Mario Scheel, Christof Schier, and Stephan Herminghaus. On capillary bridges in wet granular materials. *Physica A: Statistical Mechanics and its Applications*, 339(1-2):7–15, 2004.

[55] R Anand Kumar, Jing-fei Dong, Jenny a Thaggard, Miguel a Cruz, José a López, and Larry V McIntire. Kinetics of GPIbalpha-vWF-A1 tether bond under flow: effect of GPIbalpha mutations on the association and dissociation rates. *Biophysical journal*, 85(6):4099–4109, 2003.

[56] Wilbur A Lam, Ovijit Chaudhuri, Ailey Crow, Kevin D Webster, Tai-De Li, Ashley Kita, James Huang, and Daniel A Fletcher. Mechanics and contraction dynamics of single platelets and implications for clot stiffening. *Nature materials*, 10(1):61–6, 2011.

[57] Ra Latour. Biomaterials: protein-surface interactions. *... of Biomaterials and Biomedical Engineering*, pages 1–15, 2005.

[58] Karin Leiderman and Aaron L. Fogelson. The Influence of Hindered Transport on the Development of Platelet Thrombi Under Flow. *Physiology & behavior*, 176(1):139–148, 2017.

[59] Alessandro Leonardi, Falk K. Wittel, Miller Mendoza, and Hans J. Herrmann. Coupled DEM-LBM method for the free-surface simulation of heterogeneous suspensions. *Computational Particle Mechanics*, 1(1):3–13, 2014.

[60] Ju Li, George Lykotrafitis, Ming Dao, and Subra Suresh. Cytoskeletal dynamics of human erythrocyte. *Proc. Natl. Acad. Sci. U. S. A.*, 2007:700257104, 2007.

[61] Ton Lisman, Nicolas Raynal, Dafna Groeneveld, Ben Maddox, Anthony R. Peachey, Eric G. Huizinga, Philip G. De Groot, and Richard W. Farndale. A single high-affinity binding site for von Willebrand factor in collagen III, identified using synthetic triple-helical peptides. *Blood*, 108(12):3753–3756, 2006.

[62] Rustem I. Litvinov and John W. Weisel. Fibrin mechanical properties and their structural origins. *Matrix Biology*, 2016.

[63] W. Liu, C. R. Carlisle, E. A. Sparks, and M. Guthold. The mechanical properties of single fibrin fibers. *Journal of Thrombosis and Haemostasis*, 8(5):1030–1036, 2010.

[64] Robert M. MacMECCAN, J. R. Clausen, G. P. Neitzel, and C. K. Aidun. Simulating deformable particle suspensions using a coupled lattice-Boltzmann and finite-element method. *Journal of Fluid Mechanics*, 618:13, 2009.

[65] Guy R. McNamara and Gianluigi Zanetti. Use of the boltzmann equation to simulate lattice-gas automata. *Physical Review Letters*, 61(20):2332–2335, 1988.

[66] M. Mirramezani, B. A. Herbig, T. J. Stalker, L. Nettey, M. Cooper, J. W. Weisel, S. L. Diamond, T. Sinno, L. F. Brass, S. C. Shadden, and M. Tomaiuolo. Platelet packing density is an independent regulator of the hemostatic response to injury. *Journal of Thrombosis and Haemostasis*, 16(5):973–983, 2018.

[67] Michael J Mitchell and Michael R King. Computational and experimental models of cancer cell response to fluid shear stress. *Frontiers in oncology*, 3(March):44, 2013.

[68] S. M??nster, L. M. Jawerth, B. Fabry, and D. A. Weitz. Structure and mechanics of fibrin clots formed under mechanical perturbation. *Journal of Thrombosis and Haemostasis*, 11(3):557–560, 2013.

[69] N A Mody and M R King. Platelet Adhesive Dynamics. {Part I}: Characterization of Platelet Hydrodynamic Collisions and Wall Effects. *Biophys. J.*, 95:2539–2555, 2008.

[70] Nipa A. Mody and Michael R. King. Three-dimensional simulations of a platelet-shaped spheroid near a wall in shear flow. *Physics of Fluids*, 17(11):1–12, 2005.

[71] Nipa a. Mody and Michael R. King. Platelet adhesive dynamics. Part II: high shear-induced transient aggregation via GPIα-vWF-GPα bridging. *Biophysical Journal*, 95(5):2556–2574, 2008.

[72] Nipa A. Mody, Oleg Lomakin, Teresa A. Doggett, Thomas G. Diacovo, and Michael R. King. Mechanics of transient platelet adhesion to von Willebrand factor under flow. *Biophysical Journal*, 88(2):1432–1443, 2005.

[73] Dougald M. Monroe, Maureane Hoffman, and Harold R. Roberts. Platelets and thrombin generation. *Arteriosclerosis, Thrombosis, and Vascular Biology*, 22(9):1381–1389, 2002.

[74] Daisuke Mori, Koichiro Yano, Ken-ici Tsubota, Takuji Ishikawa, Shigeo Wada, and Takami Yamaguchi. Simulation of platelet adhesion and aggregation regulated by fibrinogen and von Willebrand factor. *Thrombosis and Haemostasis*, pages 108–115, 2008.

[75] Andrea Nans, Narla Mohandas, and David L. Stokes. Native ultrastructure of the red cell cytoskeleton by cryo-electron tomography. *Biophysical Journal*, 101(10):2341–2350, 2011.

[76] Warwick S Nesbitt, Erik Westein, Francisco Javier Tovar-Lopez, Elham Tolouei, Arnan Mitchell, Jia Fu, Josie Carberry, Andreas Fouras, and Shaun P Jackson. A shear gradient-dependent platelet aggregation mechanism drives thrombus formation. *Nature Medicine*, 15(6):665–673, 2009.

[77] Thi-Huong Nguyen, Raghavendra Palankar, Van-Chien Bui, Nikolay Medvedev, Andreas Greinacher, and Mihaela Delcea. Rupture Forces among Human Blood Platelets at different Degrees of Activation. *Scientific Reports*, 6(April):25402, 2016.

[78] Satoru Ogawa, Fania Szlam, Daniel Bolliger, Takashi Nishimura, Edward P Chen, and Kenichi A Tanaka. The impact of hematocrit on fibrin clot formation assessed by rotational thromboelastometry. *Anesthesia and analgesia*, 115(1):16–21, 2012.

[79] R. Ouared, B. Chopard, B. Stahl, D.a. Rüfenacht, H. Yilmaz, and G. Courbebaisse. Thrombosis modeling in intracranial aneurysms: a lattice Boltzmann numerical algorithm. *Computer Physics Communications*, 179(1-3):128–131, 2008.

[80] Sanjeev Palta, Richa Saroa, and Anshu Palta. Overview of the coagulation system. *Indian Journal of Anaesthesia*, 58(5):515–523, 2014.

[81] Matthew J. Paszek, Nastaran Zahir, Kandice R. Johnson, Johnathon N. Lakins, Gabriela I. Rozenberg, Amit Gefen, Cynthia a. Reinhart-King, Susan S. Margulies, Micah Dembo, David Boettiger, Daniel a. Hammer, and Valerie M. Weaver. Tensional homeostasis and the malignant phenotype. *Cancer Cell*, 8(3):241–254, 2005.

[82] Henry T. Peng. Thromboelastographic study of biomaterials. *Journal of Biomedical Materials Research - Part B Applied Biomaterials*, 94(2):469–485, 2010.

[83] Izabela K Piechocka, Karin A Jansen, Chase P Broedersz, Nicholas A Kurniawan, Fred C MacKintosh, and Gijsje H Koenderink. Multi-scale strain-stiffening of semi-flexible bundle networks. *Soft Matter*, 12(7):2145–2156, 2016.

[84] Igor Pivkin, Peter Richardson, and George Karniadakis. Effect of red blood cells on platelet aggregation. *IEEE engineering in medicine and biology magazine : the quarterly magazine of the Engineering in Medicine & Biology Society*, 28(April):32–7, 2009.

[85] C. Pozrikidis. Numerical Simulation of the Flow-Induced Deformation of Red Blood Cells. *Annals of Biomedical Engineering*, 31(10):1194–1205, 2003.

[86] Meenakshi Prabhune, Gazanfer Belge, Andreas Dotzauer, Jörn Bullerdiek, and Manfred Radmacher. Comparison of mechanical properties of normal and malignant thyroid cells. *Micron*, 43(12):1267–1272, 2012.

[87] Y. H. Qian, D. D'Humières, and P. Lallemand. Lattice bgk models for navier-stokes equation. *Epl*, 17(6):479–484, 1992.

[88] Yongzhi Qiu, Ashley C Brown, David R Myers, Yumiko Sakurai, Robert G Mannino, Reginald Tran, Byungwook Ahn, Elaissa T Hardy, Matthew F Kee, Sanjay Kumar, Gang Bao, Thomas H Barker, and Wilbur a Lam. Platelet mechanosensing of substrate stiffness during clot formation mediates adhesion, spreading, and activation. *Proceedings of the National Academy of Sciences of the United States of America*, 111(40):14430–5, 2014.

[89] M Radmacher, M Fritz, C M Kacher, J P Cleveland, and P K Hansma. Measuring the viscoelastic properties of human platelets with the atomic force microscope. *Biophysical journal*, 70(1):556–67, 1996.

[90] Marco Ranucci, Umberto Di Dedda, and Ekaterina Baryshnikova. Platelet Contribution to Clot Strength in Thromboelastometry: Count, Function, or Both? *Platelets*, 31(1):88–93, 2020.

[91] Daniel a. Reasor, Marmar Mehrabadi, David N. Ku, and Cyrus K. Aidun. Determination of critical parameters in platelet margination. *Annals of Biomedical Engineering*, 41(2):238–249, 2013.

[92] José Rivera, María Luisa Lozano, Leyre Navarro-Núñez, and Vicente Vicente García. Platelet receptors and signaling in the dynamics of thrombus formation. *Haematologica*, 94(5):700–711, 2009.

[93] Am. Robertson, a Sequeira, and Rg. Owens. Rheological models for blood. *Cardiovascular Mathematics. Modeling and simulation of the circulatory system*, pages 211–241, 2009.

[94] Zaverio M. Ruggeri and G. Loredana Mendolicchio. Adhesion mechanisms in platelet function. *Circulation Research*, 100(12):1673–1685, 2007.

[95] E A Ryan, L F Mockros, J W Weisel, and L Lorand. Structural origins of fibrin clot rheology. *Biophysical journal*, 77(5):2813–2826, 1999.

[96] Venkat Shankarraman, Grace Davis-Gorman, Jack G. Copeland, Michael R. Caplan, and Paul F. McDonagh. Standardized methods to quantify thrombogenicity of blood-contacting materials via thromboelastography. *Journal of Biomedical Materials Research - Part B Applied Biomaterials*, 100 B(1):230–238, 2012.

[97] Alexey M. Shibeko and Mikhail A. Panteleev. Untangling the complexity of blood coagulation network: Use of computational modelling in pharmacology and diagnostics. *Briefings in Bioinformatics*, 17(3):429–439, 2016.

[98] Cristina Solomon, Marco Ranucci, Gerald Hochleitner, Herbert Schochl, and Christoph J. Schlimp. Assessing the methodology for calculating platelet contribution to clot strength (platelet component) in thromboelastometry and thrombelastography. *Anesthesia and Analgesia*, 121(4):868–878, 2015.

[99] V Spicka. Generalized Kadanoff-Baym. *Phys. Rev. B*, 34(10), 1986.

[100] Cornelis Storm, Jennifer J Pastore, FC MacKintosh, TC Lubensky, and Paul A Jamney. Nonlinear elasticity in biological gels. *Nature*, 435(May):191–194, 2005.

[101] Sauro Succi, Mauro Sbragaglia, and Stefano Ubertini. Lattice Boltzmann Method. *Scholarpedia*, 5(5):9507, 2010.

[102] Louis Thibault, Annie Beauséjour, Marie Joëlle De Grandmont, Réal Lemieux, and Jean François Leblanc. Characterization of blood components prepared from whole-blood donations after a 24-hour hold with the platelet-rich plasma method. *Transfusion*, 46(8):1292–1299, 2006.

[103] Colin Thornton and Zemin Ning. A theoretical model for the stick/bounce behaviour of adhesive, elastic- plastic spheres. *Powder Technology*, 99(2):154–162, 1998.

[104] Lucas H. Ting, Shirin Feghhi, Nikita Taparia, Annie O. Smith, Ari Karchin, Esther Lim, Alex St John, Xu Wang, Tessa Rue, Nathan J. White, and Nathan J. Sniadecki. Contractile forces in platelet aggregates under microfluidic shear gradients reflect platelet inhibition and bleeding risk. *Nature Communications*, 10(1):1–10, 2019.

[105] Maurizio Tomaiulo, Timothy Stalker, John Welsh, Scott Diamond, Talid Sinno, and Lawrence Brass. A systems approach to hemostasis: 2. Computational analysis of molecular transport in the thrombus microenvironment. 124(11):1816–1824, 2014.

[106] A. Tosenberger, F. Ataullakhanov, N. Bessonov, M. Panteleev, A. Tokarev, and V. Volpert. Modelling of thrombus growth in flow with a DPD-PDE method. *Journal of Theoretical Biology*, 337:30–41, 2013.

[107] Reginald Tran, David R. Myers, Jordan Ciciliano, Elaissa L. Trybus Hardy, Yumiko Sakurai, Byungwook Ahn, Yongzhi Qiu, Robert G. Mannino, Meredith E. Fay, and Wilbur A. Lam. Biomechanics of haemostasis and thrombosis in health and disease: from the macro- to molecular scale. *Journal of Cellular and Molecular Medicine*, 17(5):579–596, 2013.

[108] Valerie Tutwiler, Rustem I Litvinov, Andrey P Lozhkin, Alina D Peshkova, Tatiana Lebedeva, Fazoil I Ataullakhanov, Kara L Spiller, Douglas B Cines, and John W Weisel. Kinetics and mechanics of clot contraction are governed by the molecular and cellular composition of the blood Running Title: Kinetics and mechanics of blood clot contraction. 127(1):149–160, 2015.

[109] Valerie Tutwiler, Hailong Wang, Rustem I. Litvinov, John W. Weisel, and Vivek B. Shenoy. Interplay of Platelet Contractility and Elasticity of Fibrin/Erythrocytes in Blood Clot Retraction. *Biophysical Journal*, 112(4):714–723, 2017.

[110] M. Ap Tzaferopoulos. On a Quasi-static Discrete Element Model of Granular Materials. *Computers and Geotechnics*, 18(2):145–165, 1996.

[111] Luis Ulloa, Mahendar Ochani, Huan Yang, Mahira Tanovic, Daniel Halperin, Runkuan Yang, Christopher J Czura, Mitchell P Fink, and Kevin J Tracey. Ethyl pyruvate prevents lethality in mice with established lethal sepsis and systemic inflammation. *Proceedings of the National Academy of Sciences*, 99(19):12351–12356, 2002.

[112] Anetta Undas. Fibrin clot properties and their modulation in thrombotic disorders. *Thrombosis and Haemostasis*, 112(1):32–42, 2014.

[113] Paola E.J. van der Meijden and Johan W.M. Heemskerk. Platelet biology and functions: new concepts and clinical perspectives. *Nature Reviews Cardiology*, 16(3):166–179, 2019.

[114] Thomas H S van Kempen, Gerrit W M Peters, and Frans N. van de Vosse. A constitutive model for the time-dependent, nonlinear stress response of fibrin networks. *Biomechanics and Modeling in Mechanobiology*, 14(5):995–1006, 2015.

[115] K. J. Van Vliet, G. Bao, and S. Suresh. The biomechanics toolbox: Experimental approaches for living cells and biomolecules. *Acta Materialia*, 51(19):5881–5905, 2003.

[116] Roman S. Voronov, Timothy J. Stalker, Lawrence F. Brass, and Scott L. Diamond. Simulation of intrathrombus fluid and solute transport using in vivo clot structures with single platelet resolution. *Annals of Biomedical Engineering*, 41(6):1297–1307, 2013.

[117] D. C. Walker, J. Southgate, G. Hill, M. Holcombe, D. R. Hose, S. M. Wood, S. Mac Neil, and R. H. Smallwood. The epitheliome: Agent-based modelling of the social behaviour of cells. *BioSystems*, 76(1-3):89–100, 2004.

[118] OR Walton. Numerical Simulation of Inclined Chute Flows of monodisperse, inelastic, fricitonal spheres. *Mechanics of Materials*, 16:239–247, 1993.

[119] Otis R. Walton and Robert L. Braun. Viscosity, granulartemperature, and stress calculations for shearing assemblies of inelastic, frictional disks. *Journal of Rheology*, 30(5):949–980, 1986.

[120] Nien-Tzu Wang and Aaron L Fogelson. Computational Methods for Continuum Models of Platelet Aggregation. *Journal of Computational Physics*, 151(2):649–675, 1999.

[121] Ping Wang. Lattice Boltzmann simulation of permeability and tortuosity for flow through dense porous media. *Mathematical Problems in Engineering*, 2014, 2014.

[122] Weiwei Wang and Michael R. King. Multiscale modeling of platelet adhesion and thrombus growth. *Annals of Biomedical Engineering*, 40(11):2345–2354, 2012.

[123] John W. Weisel. The mechanical properties of fibrin for basic scientists and clinicians. *Biophysical Chemistry*, 112(2-3 SPEC. ISS.):267–276, 2004.

[124] N Wohner. Europe PMC Funders Group Role of Cellular Elements in Thrombus Formation and Dissolution. pages 1–9, 2008.

[125] A. R. Wufsus, N. E. MacEra, and K. B. Neeves. The hydraulic permeability of blood clots as a function of fibrin and platelet density. *Biophysical Journal*, 104(8):1812–1823, 2013.

[126] Adam R. Wufsus, Kuldeepsinh Rana, Andrea Brown, John R. Dorgan, Matthew W. Liberatore, and Keith B. Neeves. Elastic behavior and platelet retraction in low- and high-density fibrin gels. *Biophysical Journal*, 108(1):173–183, 2015.

[127] Zhiliang Xu, Nan Chen, Malgorzata M Kamocka, Elliot D Rosen, and Mark Alber. A multiscale model of thrombus development. *Journal of the Royal Society, Interface / the Royal Society*, 5(24):705–22, 2008.

[128] Zhiliang Xu, Malgorzata Kamocka, Mark Alber, and Elliot D. Rosen. Computational approaches to studying thrombus development. *Arteriosclerosis, Thrombosis, and Vascular Biology*, 31(3):500–505, 2011.

[129] Takami Yamaguchi, Takuji Ishikawa, Y. Imai, N. Matsuki, Mikhail Xenos, Yuefan Deng, and Danny Bluestein. Particle-based methods for multiscale modeling of blood flow in the circulation and in devices: Challenges and future directions: Sixth international bio-fluid mechanics symposium and workshop March 28-30, 2008 Pasadena, California. *Annals of Biomedical Engineering*, 38(3):1225–1235, 2010.

[130] Z. Yan, S. K. Wilkinson, E. H. Stitt, and M. Marigo. Discrete element modelling (DEM) input parameters: understanding their impact on model predictions using statistical analysis. *Computational Particle Mechanics*, 2(3):283–299, 2015.

[131] Siying Zhang and Joseph J. McCarthy. Modeling of the pressure drop across polydisperse packed beds in cake filtration. *AIChE Journal*, 65(5):1–11, 2019.

[132] Simon Zimny, Bastien Chopard, Orestis Malaspinas, Eric Lorenz, Kartik Jain, Sabine Roller, and Jörg Bernsdorf. A multiscale approach for the coupled simulation of blood flow and thrombus formation in intracranial aneurysms. *Procedia Computer Science*, 18(0):1006–1015, 2013.